

**University of Alberta**

**Cross-Equatorial Flow of Grounded Abyssal Ocean Currents**

by

**Alexander Kim**

A thesis submitted to the Faculty of Graduate Studies and Research  
in partial fulfillment of the requirements for the degree of

**Master of Science**

**Department of Physics**

©Alexander Kim  
Fall 2013  
Edmonton, Alberta

Permission is hereby granted to the University of Alberta Libraries to reproduce single copies of this thesis and to lend or sell such copies for private, scholarly or scientific research purposes only. Where the thesis is converted to, or otherwise made available in digital form, the University of Alberta will advise potential users of the thesis of these terms.

The author reserves all other publication and other rights in association with the copyright in the thesis and, except as herein before provided, neither the thesis nor any substantial portion thereof may be printed or otherwise reproduced in any material form whatsoever without the author's prior written permission.

## Dedication

This thesis is dedicated to my late brother and best friend Vladimir Park who was brutally murdered in July 2011, a few weeks after he earned his degree in Computer Science and five days before his 22nd birthday. He was always supportive and encouraging to me throughout my education and life, yet I did not have a chance to say a last goodbye. His inspiration will always push me to greater heights.

# Abstract

An idealized process study is presented describing the cross-equatorial flow of grounded abyssal ocean currents in a differentially-rotating meridional channel with parabolic bottom topography. In particular we fully examine the dependence of the cross-equatorial volume flux on the underlying flow parameters including slope of the channel's walls ( $s$ ), half-width of the channel ( $l$ ), width and height of the abyssal current ( $a$  and  $H$ ), magnitude of the rotation vector ( $\Omega$ ), Earth's radius ( $R$ ) and reduced gravity ( $g'$ ).

We determined that the ratio between the width of the channel and the zonal wavelength of a narrow wave structure that is formed by the current in the equatorial region plays a crucial role in determining into which hemisphere the current flows after its interaction with the equator. It is found that some parameters ( $a$  and  $H$ ) do not have any significant effect on the zonal wavelength, while variations in other parameters ( $s$ ,  $\Omega$ ,  $R$  and  $g'$ ) change the zonal wavelength and, consequently, the behaviour of the abyssal current. After examining an auxiliary model of a particle in a rotating channel, we derived a combination of these parameters  $L_{Rh} = \frac{1}{2} \left( \frac{g's}{y_0} \right)^{1/2} \frac{R}{\Omega}$  called the Rhines scale and the zonal wavelength is found to be linearly proportional to this scale.

# Acknowledgements

My first debt of gratitude must go to my supervisors, Dr. Bruce R. Sutherland and Dr. Gordon E. Swaters, for their help, guidance, and many hours worth of thesis corrections, but mainly for introducing me to the world of scientific research. Their support has served me well and I owe them my heartfelt appreciation. I also would like to thank my committee members for their time, interest, and valuable insight.

My thanks and appreciation goes to the members of my research group with whom I have interacted during the course of my graduate studies and who provided me with many valuable comments and insights on the research.

I would like to thank graduate program assistant, Sarah Derr, who calmed me down when I expressed a complete lack of knowledge about paperwork, protocols, and procedures.

I owe a lot to my family - especially my mother and father for always believing in me and for their tremendous support and encouragement from thousand miles away. I extend acknowledgement and love to my sister. She has always provided me with motivation and cheer.

Finally, I owe a very important debt to my girlfriend Olga. We both know I could not have done this without you. Thank you for keeping me sane - a feat that easily exceeds that of conducting a scientific research.

# Table of Contents

## List of Tables

## List of Figures

<b>1</b>	<b>Introduction</b>	<b>1</b>
1.1	Introduction . . . . .	1
<b>2</b>	<b>Derivation of our Model Equations</b>	<b>6</b>
2.1	Navier-Stokes Equations . . . . .	6
2.2	Shallow Water Equations . . . . .	10
<b>3</b>	<b>Numerical Scheme</b>	<b>13</b>
3.1	Spatial Discretization . . . . .	13
3.2	Implementation of the Flux-Corrected Transport Algorithm . . . . .	14
3.3	Initialization and Boundary Conditions . . . . .	19
3.4	Default set of parameter values . . . . .	21
<b>4</b>	<b>Comparison of Numerical Solution with Two Exact Solutions</b>	<b>23</b>
4.1	Steady solution of governing SWE on an f-plane . . . . .	24
4.2	Planetary Geostrophic Model . . . . .	30
<b>5</b>	<b>Results and Discussion</b>	<b>37</b>
5.1	Numerical Simulations of a Grounded Abyssal Current Approaching the Equator . . . . .	37
5.2	Auxiliary Model of a Particle in a Rotating Channel . . . . .	61
5.3	Comparison of Two Models . . . . .	67
<b>6</b>	<b>Conclusions</b>	<b>71</b>
6.1	Summary . . . . .	71
6.2	Future Directions . . . . .	74
	<b>Bibliography</b>	<b>76</b>

# List of Tables

3.1	Default values of parameters . . . . .	22
5.1	Numerical simulations for various values of $g'$ . . . . .	47
5.2	Numerical simulations for various values of $s$ . . . . .	49
5.3	Numerical simulations for various values of $\Omega$ . . . . .	51
5.4	Numerical simulations for various values of $l$ . . . . .	53
5.5	Numerical simulations for various values of $R$ . . . . .	55
5.6	Numerical simulations for various values of $a$ . . . . .	57
5.7	Numerical simulations for various values of $H$ . . . . .	59

# List of Figures

2.1	Geometry of the model. The west-to-east cross section view at $y = y_0$ . $h_b(x)$ is the bottom topography, $h(x)$ is the height of the abyssal current (lower layer), $\rho_1$ and $\rho_2$ are the densities in the upper and lower layers, respectively. The center of the current is located at $x = 0$ . The point of maximum depth is located at $x = l$ . . . . .	7
2.2	The local Cartesian coordinate system ( $x$ -axis is directed into the page), the Earth's radius is $R$ , the magnitude of the rotation vector is $\Omega$ and the reference latitude is $\phi$ . . . . .	8
3.1	The staggered Arakawa C-grid. The heights $h$ are located in the center of each grid cell, velocity components $u$ are located on the vertical edges of each grid cell, and velocity components $v$ are located on the horizontal edges of each grid cell. Grid cell sizes $\Delta y$ , $\Delta x$ are constant throughout the domain. . . . .	15
3.2	Domain used in the numerical simulations. The boundaries of the domain are located at $y = y_0, -y_0$ and $x = x_1, x_2$ , respectively. The initial current's height $h_0(x)$ is located at $y = y_0$ between $x = -a$ and $x = a$ . The center of the current is located at $x = 0$ . $x = l$ is the distance between the center of the current and point of the maximum depth. . . . .	20
4.1	Cross-sections of the exact analytic solutions $h_f$ ((4.4)) and $v_f$ ((4.5)) to the model equations assuming an $f$ -plane approximation. (a) Cross-section view of the height $h_f$ . (b) Cross-section view of the meridional velocity $v_f$ . . . . .	25
4.2	Contour plots of the analytical solution to the $f$ -plane equations with $l = 1000$ km. (a) Current height, $h_f$ . and (b) Current meridional velocity, $v_f$ . . . . .	26
4.3	As in 4.2 but showing the contour plots of the numerical solution of the fully nonlinear equations on the $f$ -plane. . . . .	26

4.4	The errors between the exact analytical $h_f, u_f, v_f$ and numerical $h, u, v$ solutions along constant longitudes (constant $x$ ). (a) $\tilde{h}$ along $x = -79$ km, (b) $\tilde{h}$ along $x = 0$ km, (c) $\tilde{u}$ along $x = -79$ km, (d) $\tilde{u}$ along $x = 0$ km, (e) $\tilde{v}$ along $x = -79$ km and (f) $\tilde{v}$ along $x = 0$ km. . . . .	28
4.5	The errors between the exact analytical $h_f, u_f, v_f$ and numerical $h, u, v$ solutions along constant latitudes (constant $y$ ). Figures indicate that the errors near the downslope grounding ( $x = 80$ km) are of the same order as the ones near the upslope grounding ( $x = -80$ km). (a) $\tilde{h}$ along $y = -3000$ km, (b) $\tilde{h}$ along $y = 0$ km, (c) $\tilde{u}$ along $y = -3000$ km, (d) $\tilde{u}$ along $y = 0$ km, (e) $\tilde{v}$ along $y = -3000$ km and (f) $\tilde{v}$ along $y = 0$ km. . . . .	29
4.6	Contour plot of the current's height determined from the geostrophic model equations $h_p$ (Swaters, 2006, 2013). . . . .	32
4.7	Contour plot of the current's height $h$ obtained from the numerical simulations. . . . .	33
4.8	Heights $h_p$ and $h$ at $x = 0$ km vs. $y$ , the meridional distance from the equator. . . . .	34
4.9	Difference between the numerical solution $h$ and geostrophic model solution $h_p$ normalized by $H$ . . . . .	35
5.1	Experiment with the default initialization parameters: $H_0 = 200$ m, $a_0 = 80$ km, $s_0 = 6 \times 10^{-3}$ , $l_0 = 1000$ km, $g'_0 = 8 \times 10^{-4}$ m/s <sup>2</sup> , $\Omega_0 = 7.29 \times 10^{-5}$ rad/s and $R_0 = 6371$ km. The horizontal line represents the equator. The vertical line represents the location of the channel's axis at greatest depth. Figures (a) to (d) show the contour of the height $h$ at different times: (a) $h$ at $t=231$ days, (b) $h$ at $t=255$ days, (c) $h$ at $t=347$ days, and (d) $h$ at $t=428$ days. . . . .	39
5.2	Experiment with the physical parameters set to their default values. (a) Total mass of fluid in the current vs. time. (b) Total energy vs. time. . . . .	40
5.3	Contour plot of the current's height $h$ after the current has reached the state of constant energy. The physical parameters are set to their default values as given in Figure 5.1 . . . . .	41
5.4	Contour plot of the current's eastward velocity $u$ after the current has reached the state of constant energy. The physical parameters are set to their default values as given in Figure 5.1 . . . . .	42
5.5	Contour plot of the current's northward velocity $v$ after the current has reached the state of constant energy. The physical parameters are set to their default values as given in Figure 5.1 . . . . .	43
5.6	Contour plots of $h$ for various values of $g'$ (Table 5.1). . . . .	47
5.7	Southward transmission coefficients $T_s$ vs. $g'$ . . . . .	48
5.8	Contour plots of $h$ for various values of $s$ (Table 5.2). . . . .	49
5.9	Southward transmission coefficients $T_s$ vs. $s$ . . . . .	50

5.10	Contour plots of $h$ for various values of $\Omega$ (Table 5.3). . . . .	51
5.11	Southward transmission coefficients $T_s$ vs. $\Omega$ . . . . .	52
5.12	Contour plots of $h$ for various values of $l$ (Table 5.4). . . . .	53
5.13	Southward transmission coefficients $T_s$ vs. $l$ . . . . .	54
5.14	Contour plots of $h$ for various values of $R$ (Table 5.5). . . . .	55
5.15	Southward transmission coefficients $T_s$ vs. $R$ . . . . .	56
5.16	Contour plots of $h$ for various values of $a$ (Table 5.6). . . . .	57
5.17	Southward transmission coefficients $T_s$ vs. $a$ . . . . .	58
5.18	Contour plots of $h$ for various values of $H$ (Table 5.7). . . . .	59
5.19	Southward transmission coefficients $T_s$ vs. $H$ . . . . .	60
5.20	Trajectories of a particle in a rotating cross-equatorial channel for various value of $g'$ . . . . .	65
5.21	Particle model. Wavelength $\lambda$ of the zonal wave in the equatorial area vs. the Rhines scale $L_{Rh}$ given by (5.13). . . . .	66
5.22	Numerical simulations. Wavelength $\lambda$ of the zonal wave in the equatorial area vs. the Rhines scale $L_{Rh}$ given by (5.13). . . . .	69
5.23	Southward transmission coefficients $T_s$ vs. $\frac{\lambda}{2l}$ (top axis) and $\frac{L_{Rh}}{2l}$ (bottom axis). . . . .	70

# Chapter 1

## Introduction

### 1.1 Introduction

Thorough knowledge of ocean circulation is a key component in understanding the processes of global climate. One of the most important phenomena that take place in the world ocean are ocean currents. These currents are generated by many different forces such as wind, gravitational effect exerted by the Moon and Sun, thermohaline and buoyancy processes.

Thermohaline circulation is a circulation driven by density differences caused by non-uniform distribution of temperature (thermo) and salinity (haline) in the ocean waters. Circulation in the abyss of the world ocean is mainly induced by thermohaline processes. Abyssal waters form in subpolar regions when atmospheric cooling increases the local density. If the density is sufficiently increased, the water can sink to the bottom where it can form abyssal currents that flow equatorward and beyond.

Stommel and Arons (1958; 1959) developed the first theory of abyssal ocean circulation. According to this theory, away from the continental shelf abyssal circulation consists of waters that principally originate in two sources located at high latitudes - North Atlantic and Antarctic regions. In these source regions abyssal waters are formed during the respective cold seasons and, due to cooling and salinization associated with formation of sea ice, they start to sink and continue to do so until possibly they reach the ocean bottom.

In the North Atlantic, away from the sources, abyssal currents propagate towards

the equator in the form of the Deep Western Boundary Currents (DWBC). During their equatorward propagation some water in the abyssal current gradually increases its temperature, mixes with the overlying fluid and rises to the surface supplying the flows that carry it back to subpolar regions. This process compensates the excessive amount of heat acquired by the surface waters at low latitudes (Siedler *et al.*, 2001; Samelson, 2011).

At high latitudes in the northern hemisphere the cooled salty water sinks to the deep ocean forming the North Atlantic Deep Water (NADW). Labrador and Norwegian/Greenland seas are the main sources that supply the NADW. From here it spreads southward in the form of the DWBC (Cunningham *et al.*, 2007; McCarthy *et al.*, 2012).

A portion of abyssal waters formed in the Antarctic region, mainly in the Weddell sea, propagate eastward in the form of the Antarctic Circumpolar Current (ACC) (Siedler *et al.*, 2001). Other parts of these waters constitute the deepest water in the Atlantic ocean - the Antarctic Bottom Water (AABW). Some of this flow remains in the southern hemisphere, while the rest of it has been observed to cross the equator and end up in the northern hemisphere (De Madron & Weatherly, 1994). As it propagates in the northward direction, the AABW mixes with the overlying Lower North Atlantic Deep Water (LNADW) decreasing its transport with latitude (Paldor *et al.*, 2003; Kamenkovich & Goodman, 2001). Despite qualitatively good agreement between the observational data and schematic circulation given by Stommel and Arons, their theory does not explain the mechanisms at work when the bottom water enters the vicinity of the equator.

Due to the conservation of potential vorticity, idealized models of inviscid fluid are not able to describe the abyssal currents that cross the equator and propagate long distances away from it. Killworth's (1991) model has shown that inviscid cross-equatorial geostrophic adjustment allows the fluid to penetrate into the opposite hemisphere, but the penetration distance is limited to a few deformation radii from the equator.

Edwards & Pedlosky (1998) studied potential vorticity modification in the frame-

work of nonlinear deep western boundary currents. They pointed out that the relative vorticity in the abyssal currents is negligible and, since the Coriolis parameter changes sign at the equator, penetration into the opposite hemisphere by the abyssal currents can only occur if the potential vorticity is modified by dissipative or non-conservative processes.

Kawase *et al.* (1992) numerically integrated the three-dimensional equations of motion under the Boussinesq approximation assuming flat topography. During the initial stages of its motion the simulated current was observed to flow in the equatorward direction. According to this study, when the current enters the equatorial region it turns eastward and oscillates perpendicular to the equator. However, in the steady-state limit the oscillations disappear and the crossing of the equator is observed along the western boundary.

Borisov & Nof (1998) compared a relatively simple model of the inertial motion of a cloud of solid particles to numerical simulations of eddies propagating in a parabolic meridional channel on an equatorial  $\beta$ -plane. Although models of balls and eddies are obviously not identical, they found that the dependence of the cross-equatorial volume flux on the steepness of the channel walls was very similar in both models. They also concluded that the splitting of the eddies into northward and southward trajectories occurs because of the presence of the bathymetry and not due to the conservation of potential vorticity. The penetration into the opposite hemisphere was argued to be independent of the initial potential vorticity distribution. Thus, the modification of potential vorticity merely takes place to allow the current to follow paths prescribed to it by the shape of the bottom topography.

Nof & Borisov (1998) numerically simulated the cross-equatorial motion of continuous double front currents (flows with an upslope and downslope incropping) in a meridional channel with parabolic bottom topography on an equatorial  $\beta$ -plane. Their study showed that the percentage of volume flux that crossed the equator and ended up in the opposite hemisphere depends on the steepness of the bottom topography. In general, many similarities were found between the model of continuous currents and models of eddies and solid balls studied by Borisov & Nof (1998). Solid

balls, however, occasionally exhibited chaotic behaviour not observed in the cases of currents and eddies.

Choboter & Swaters (2000) examined both the frictional-geostrophic and full shallow water equations in the context of abyssal cross-equatorial currents over idealized topography. The major disadvantage of their frictional-geostrophic model lies in neglecting the fluid inertia. However, after comparing this model to a more sophisticated shallow-water model they concluded, that both models quantitatively agree in capturing certain aspects of motion such as along-shelf propagation, downhill acceleration and northward-southward splitting.

Swaters (2013) derived a nonlinear planetary geostrophic model for the flow of abyssal currents far from the equator on a rotating sphere and found its analytic solution. Further analysis of this solution revealed that it has several properties. The groundings of the current, i.e., the curves where the current height intersects the bottom, were found to be set by the boundary conditions and do not change as the current propagates equatorward. The averaged height of the current showed a nearly linear decrease with decreasing latitude, while the meridional volume transport was shown to be independent of latitude. The main disadvantage of the solution is its singularity at the equator. Hence this model is incapable of describing the behaviour of the current as it encounters the equator.

The principal goal of this thesis is to model the equatorward propagation of a grounded abyssal current in a differentially rotating meridional channel with parabolic bottom topography. In this sense we will resolve the singularity that develops in the Swaters (2013) solution and provide a detailed description of the dependence of the cross-equatorial volume flux on all the flow parameters. The plan of this thesis is as follows.

In chapter 2 we introduce several approximations to the Navier-Stokes equations in order to derive the reduced-gravity shallow water equations appropriate for our problem. The resulting model takes into account frictional and topographic effects that previous studies found to be important when considering the dynamics of cross-equatorial abyssal flow. Chapter 3 presents the spatial discretization of the domain

as well as computational methods that were used to numerically solve the reduced-gravity shallow water equations. The final section in chapter 3 contains a table of the default physical parameters used in our simulations. In chapter 4 we verify that our numerical procedure produces solutions that are consistent with two previously known analytical results. In chapter 5 we present different numerical simulations that were conducted by varying each physical parameter individually. To help us interpret results of the numerical simulations, we apply a relatively simple model of a particle in a differentially rotating channel. Finally, in chapter 6 we summarize the obtained results, discuss the impact of our research and describe ways to improve the numerical model to be more realistic and consistent with modern-day oceanographic observations.

# Chapter 2

## Derivation of our Model Equations

### 2.1 Navier-Stokes Equations

In this chapter we derive the reduced gravity shallow water equations that we used for our numerical simulations. We start with the primitive Navier-Stokes equations in Cartesian coordinates for a differentially rotating fluid assuming the hydrostatic approximation (Pedlosky, 1982). The Navier-Stokes equations are a system of non-linear partial differential equations derived from Newton's second law of motion for an incompressible fluid parcel at some point in space and time. The hydrostatic balance is the assumption that gravity balances the pressure gradient in the vertical equation of motion and that the vertical accelerations can be neglected.

We will work with a two-layer reduced gravity model that assumes that the density in the upper layer is equal to a constant  $\rho_1$  and the density in the lower layer is given by a constant  $\rho_2$  (with a stable stratification, i.e.,  $\rho_2 > \rho_1$ ). Furthermore, the upper layer is assumed to be infinitely deep and motionless. The geometrical set-up of the problem is shown in Figure 2.1. This figure shows the west-to-east cross-section view at the initial location of the current located at  $y = y_0$ , where  $y$  increases in the northward direction and  $y = 0$  corresponds to the equator. The positive  $x$  and  $z$  directions are pointing eastward and radially outward (as shown in Figure 2.2), respectively.

If we define a plane tangent to the surface of the Earth at a latitude  $\phi$ , then  $\phi \simeq \frac{y}{R}$

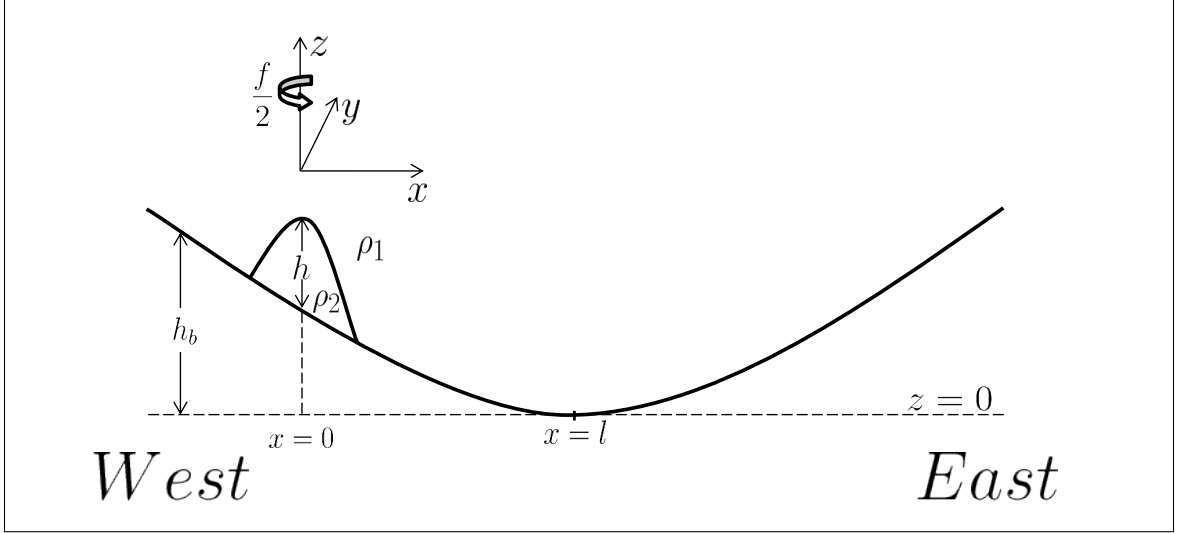


**Figure 2.1:** Geometry of the model. The west-to-east cross section view at  $y = y_0$ .  $h_b(x)$  is the bottom topography,  $h(x)$  is the height of the abyssal current (lower layer),  $\rho_1$  and  $\rho_2$  are the densities in the upper and lower layers, respectively. The center of the current is located at  $x = 0$ . The point of maximum depth is located at  $x = l$ .

and the Coriolis acceleration is

$$\mathbf{a}_c = 2\boldsymbol{\Omega} \times \mathbf{v} = 2(\Omega^y w - \Omega^z v)\mathbf{i} + 2(\Omega^z u - \Omega^x w)\mathbf{j} + 2(\Omega^x v - \Omega^y u)\mathbf{k}, \quad (2.1)$$

where  $u$ ,  $v$ ,  $w$  are the velocities and  $\mathbf{i}$ ,  $\mathbf{j}$ ,  $\mathbf{k}$  are the unit vectors in the eastward, northward and vertical directions, respectively, and the rotation vector is given by

$$\boldsymbol{\Omega} = \Omega^x \mathbf{i} + \Omega^y \mathbf{j} + \Omega^z \mathbf{k}, \quad (2.2)$$

and  $\Omega^x = 0$ ,  $\Omega^y = \Omega \cos(y/R)$ ,  $\Omega^z = \Omega \sin(y/R)$  in local Cartesian coordinates,  $R$  is the radius of the Earth,  $\Omega$  is the magnitude of the angular frequency vector associated with the Earth's rotation, i.e.  $\frac{2\pi \times \text{radians}}{\text{day}}$  (Figure 2.2). Then we make the traditional rapidly-rotating approximation (Pedlosky, 1982) and neglect the components of  $\boldsymbol{\Omega}$  not in the direction of the local vertical. This simplifies the Coriolis acceleration to  $\mathbf{a}_c = (-fv, fu, 0)$  where  $f$  is the Coriolis parameter given by

$$f = 2\Omega \sin(y/R). \quad (2.3)$$

The coordinate system, the rotation vector and a latitude  $\phi$  are shown in Figure 2.2.

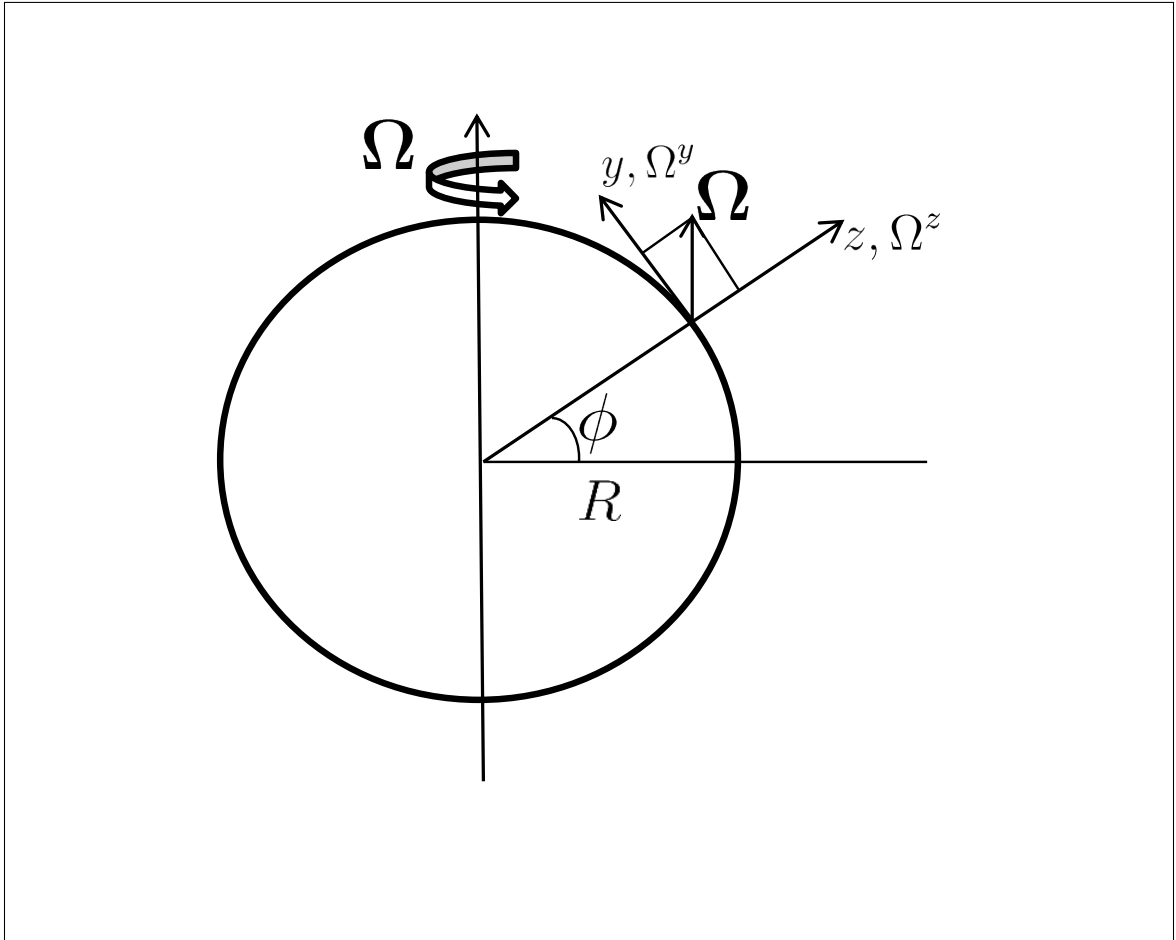


**Figure 2.2:** The local Cartesian coordinate system ( $x$ -axis is directed into the page), the Earth's radius is  $R$ , the magnitude of the rotation vector is  $\Omega$  and the reference latitude is  $\phi$ .

There exist two commonly used approximations of the Coriolis parameter (Valis, 2006). Their purpose is to simplify the governing equations in order to obtain dynamical insight and analytic solutions.

First, there is a so-called  $f$ -plane approximation that assumes this parameter to be constant and equal to its value at some fixed latitude  $\phi^* \simeq y^*/R$

$$f_0 = 2\Omega \sin(\phi)|_{\phi=y^*/R} = 2\Omega \sin(y^*/R). \quad (2.4)$$

It is largely used to represent mid-latitude phenomena of limited meridional extent, where the effect of the curvature of the Earth's surface can be neglected.

Secondly, if the variation of the Coriolis parameter has important dynamical consequences, we can approximate it by assuming a relatively small change in latitude and expanding  $f(\phi)$  about  $\phi = \phi^*$  as follows

$$f(\phi) = 2\Omega \sin(\phi^*) + 2\Omega \cos(\phi^*)(\phi - \phi^*) + \dots, \quad (2.5)$$

so that on the plane tangent to the Earth's surface at the fixed latitude  $\phi^*$ , where  $\phi - \phi^* \simeq \frac{\Delta y}{R}$ , we have

$$f(y) \simeq f_0 + \beta \Delta y, \quad (2.6)$$

where  $f_0 = 2\Omega \sin(y^*/R)$  and  $\beta = \frac{2\Omega}{R} \cos(y^*/R)$ . This approximation is known as the  $\beta$ -plane approximation.

In this thesis, the problem will be approached using numerical techniques for large scale flows. Thus, we will not be making either of these two approximations, and the Coriolis parameter will be used in the form of (2.3).

Under all of the above mentioned assumptions, the basic two-dimensional equations for an incompressible fluid with two external forces (gravity force and Coriolis force) can be written as follows (Pedlosky, 1982):

- x-momentum (or eastward-momentum) conservation equation

$$u_t + uu_x + vu_y + wu_z - fv = -\frac{p_{2x}}{\rho_2}, \quad (2.7)$$

- y-momentum (or northward-momentum) conservation equation

$$v_t + uv_x + vv_y + wv_z + fu = -\frac{p_{2y}}{\rho_2}, \quad (2.8)$$

- mass conservation equation for an incompressible fluid

$$u_x + v_y + w_z = 0, \quad (2.9)$$

- hydrostatic balance equations

$$\begin{aligned} p_{1z} &= -\rho_1 g, \\ p_{2z} &= -\rho_2 g, \end{aligned} \quad (2.10)$$

in which subscripts denote partial derivatives and where  $u$ ,  $v$  and  $w$  are the velocities of a fluid parcel inside the current in the eastward, northward and  $z$ -directions, respectively.  $f$  is the Coriolis parameter,  $p_1$ ,  $\rho_1$  and  $p_2$ ,  $\rho_2$  are the pressures and densities in the upper and lower layers, respectively.

## 2.2 Shallow Water Equations

Now we derive the non-linear shallow water equations based on the hydrostatic Navier-Stokes equations (2.7), (2.8), (2.9) and (2.10). First, integration of the hydrostatic balance equations (2.10) implies

$$\begin{aligned} p_1 &= -\rho_1 g z, \\ p_2 &= -\rho_2 g z + \hat{p}(x, y, t), \end{aligned} \quad (2.11)$$

Then, after applying the pressure continuity condition across the interface between the two layers located at  $z = h_b(x) + h(x, y, t)$ , we have

$$p_1|_{z=h_b+h} = p_2|_{z=h_b+h} \Rightarrow \hat{p} = \rho_2 g'(h_b + h), \quad (2.12)$$

where  $g' = \frac{\rho_2 - \rho_1}{\rho_2} g$  is the reduced gravity,  $h$  is the height of the abyssal current (lower layer), and  $h_b$  is the bottom topography. Using equations (2.11) and (2.12), we rewrite the  $x$  and  $y$  momentum equations (2.7) and (2.8) as

$$u_t + uu_x + vu_y - 2\Omega \sin\left(\frac{y}{R}\right)v = -g'(h_b + h)_x, \quad (2.13)$$

$$v_t + uv_x + vv_y + 2\Omega \sin\left(\frac{y}{R}\right)u = -g'(h_b + h)_y. \quad (2.14)$$

Observing that the pressure gradient terms in (2.13) and (2.14) are both independent of  $z$  leads us to assume that  $u$  and  $v$  are also independent of  $z$  if they are as such initially. Integration of the mass conservation equation (2.9) with respect to  $z$  from  $h_b$  to  $h_b + h$  gives

$$\int_{h_b}^{h_b+h} (u_x + v_y)dz + \int_{h_b}^{h_b+h} w_z dz = (u_x + v_y)h + w|_{z=h_b+h} - w|_{z=h_b}.$$

And since (Pedlosky, 1982)

$$\begin{aligned} w|_{z=h_b} &= uh_{b_x} + vh_{b_y}, \\ w|_{z=h_b+h} &= h_t + u(h + h_b)_x + v(h + h_b)_y, \end{aligned}$$

the mass continuity equation for the shallow water equations becomes

$$h_t + (hu)_x + (hv)_y = 0. \quad (2.15)$$

In the literature (e.g, Gent, 1993; Bresch, 2009; Curchitser *et al.*, 1999), viscosity is often neglected in the derivation and added *a posteriori* to the system of shallow water equations. We will adopt the same approach and add the viscosity term to our momentum equations in the form  $\nu \nabla \cdot (h \nabla \mathbf{u})/h$ , as was done, for example, in (Gustafsson & Sundstrom, 1978). According to Gent (1993) this form of the viscosity term is energetically consistent unlike another commonly used form  $\nu \nabla^2 \mathbf{u}$  (e.g, Lorenz, 1980; Gent & McWilliams, 1982; Curry & Winsand, 1986).

Finally, we rewrite the system of equations in conservation form, because our numerical methods are based on discretizing “conservative” quantities

$$\mathbf{q}_t + \mathbf{F}_x + \mathbf{G}_y = \mathbf{S}^b + \mathbf{S}^c + \mathbf{S}^\nu, \quad (2.16)$$

where

$$\mathbf{q} = \begin{pmatrix} h \\ hu \\ hv \end{pmatrix},$$

$$\mathbf{F} = \mathbf{q}u = \begin{pmatrix} hu \\ hu^2 \\ huv \end{pmatrix},$$

$$\mathbf{G} = \mathbf{q}v = \begin{pmatrix} hv \\ huv \\ hv^2 \end{pmatrix},$$

$$\mathbf{S}^b = \begin{pmatrix} 0 \\ -g'h(h+h_b)_x \\ -g'h(h+h_b)_y \end{pmatrix},$$

$$\mathbf{S}^c = \begin{pmatrix} 0 \\ 2\Omega \sin(\frac{y}{R}) hv \\ -2\Omega \sin(\frac{y}{R}) hu \end{pmatrix},$$

$$\mathbf{S}^\nu = \begin{pmatrix} 0 \\ \nu \nabla \cdot (h \nabla u) \\ \nu \nabla \cdot (h \nabla v) \end{pmatrix}.$$

# Chapter 3

## Numerical Scheme

### 3.1 Spatial Discretization

We shall use a finite volume method (FVM) to discretize our equations numerically. It was initially developed by McDonald (1971) and MacCormack & Paullay (1972) to solve the two-dimensional Euler equations.

The main idea behind FVM is simple and can be easily explained using the following physical interpretation. We divide our domain into a number of non-overlapping regions (finite volumes) in such a way that every nodal point is located inside a region. The differential equations are then integrated over each finite volume. Piecewise constant profiles are used to calculate integral quantities that describe the change of the dependent physical variable between the nodal points. Finally, we arrive at discrete analogs of our differential equations that contain values of the dependent variables at several nodal points. The FVM suits our purposes for a number of reasons:

1. In comparison to finite difference methods (FDM), FVM is more reliable if the solution has discontinuities or sharp gradients.
2. FVM has a more intuitive formulation and is usually less expensive computationally than finite element methods (FEM).
3. The resulting discretization is conservative locally and globally, i.e. mass, momentum and energy are conserved in a discrete sense even on a coarse grid.

The values of our physical quantities are updated every time step by the exchanges of fluxes across each grid cell boundary, and the main problem is to determine a good numerical procedure that approximates and corrects the fluxes in and out of the grid cell reasonably well. Our choice for this procedure is the flux-corrected transport (FCT) algorithm (Boris & Book, 1976; Zalesak, 1979), which will be introduced later.

There are two types of grid arrangements used to discretize fluid flow equations: staggered grids and collocated (non-staggered) grids. In collocated grids, both scalar and vector variables are sampled at the same locations. It is well known (e.g., Churbanov *et al.*, 1995; Ye & McCorquodale, 1997; Rahman *et al.*, 1996) that a collocated grid arrangement with the use of linear interpolation of velocities in the continuity equation causes non-physical oscillations in the fluid height distribution, the so-called checkerboard effect.

In staggered grids, scalar and vector variables are evaluated at different locations, shifted half of finite volume size in each coordinate direction. This arrangement of staggered grids requires us to handle different control volumes for different variables and thus makes their implementation slightly more challenging. In spite of this difficulty, staggered grids are very popular because, unlike collocated grids, staggered grids do not require any special treatment to prevent the checkerboard effect (Rhie & Chow, 1983). Figure 3.1 shows the configuration of the staggered Arakawa C-grid (Arakawa & Lamb, 1977; Arakawa & Hsu, 1990) that is implemented in our model. This grid is frequently used in numerical simulations of fluid flow (e.g., Choboter & Swaters, 2004; Stephens & Marshall, 2000; Nof & Borisov, 1998). Due to the aforementioned properties it is a very suitable choice for our shallow water equations.

## **3.2 Implementation of the Flux-Corrected Transport Algorithm**

FVM formulation of the flux-corrected transport (FVM-FCT) method is used to solve our shallow water equations. The FCT method was developed as a method that accurately solves the conservation equations without violating important properties of

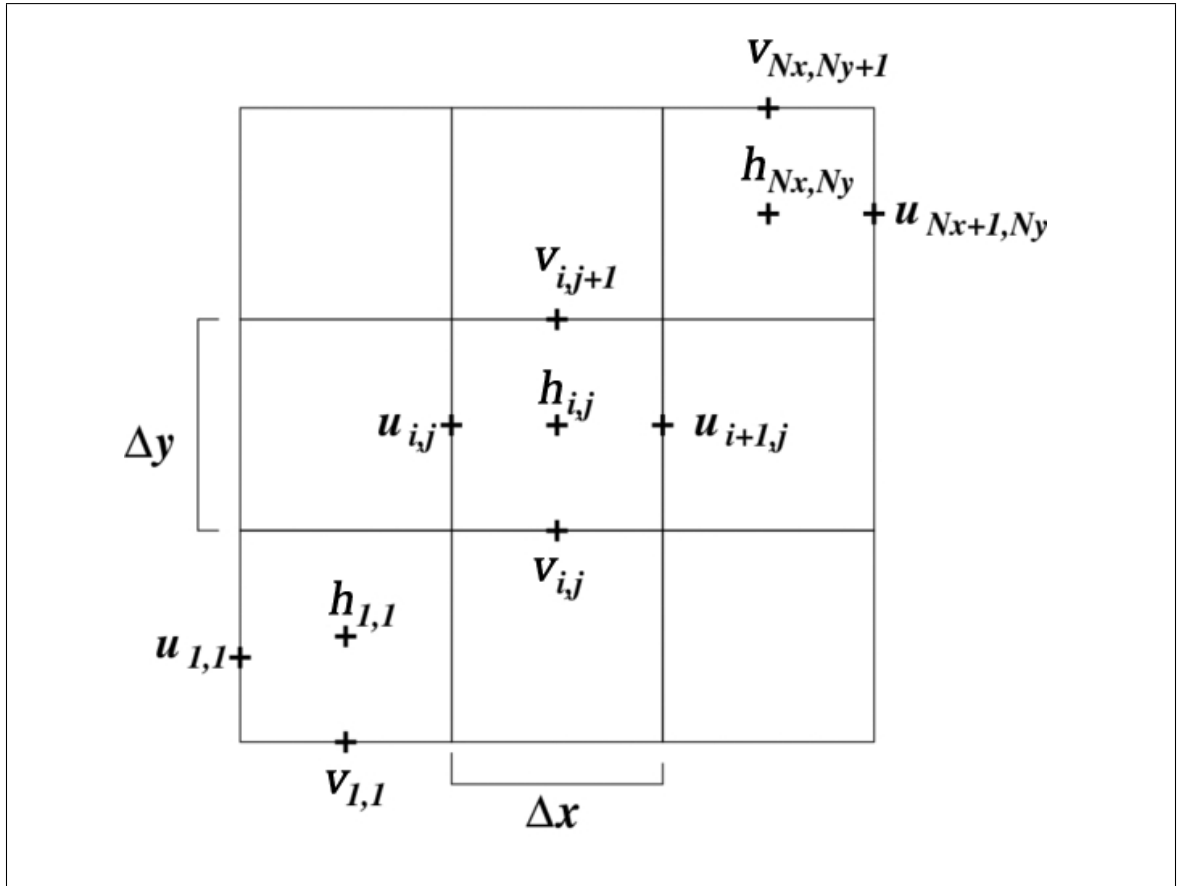


**Figure 3.1:** The staggered Arakawa C-grid. The heights  $h$  are located in the center of each grid cell, velocity components  $u$  are located on the vertical edges of each grid cell, and velocity components  $v$  are located on the horizontal edges of each grid cell. Grid cell sizes  $\Delta y$ ,  $\Delta x$  are constant throughout the domain.

the solution like positivity of mass, particularly near discontinuities (Boris & Book, 1973). This is achieved by using low-order fluxes (i.e., adding to the equations a strong numerical diffusion), which guarantees not to generate unphysical values (e.g., Courant *et al.*, 1952; Patankar, 1980), followed by application of high-order fluxes (an antidiffusion step), which reduces the numerical error due to the high resolving power of the latter fluxes (Colella & Sekora, 2008; Colella *et al.*, 2008). The main objective behind the FCT method is not to introduce unphysical extrema to the solution by limiting (correcting) the antidiffusive fluxes before they are applied. The FCT method was later generalized and adjusted to multidimensions by Zalesak (1979).

The following summarizes the procedure:

1. Compute the fluxes using both low-order and high-order methods. For low-order fluxes we used a first-order accurate two-dimensional upwind scheme (e.g., Courant *et al.*, 1952; Patankar, 1980) given by

$$q_{i+1/2,j}^L = \begin{cases} q_{i,j}^n & \text{if } u_{i+1/2,j} > 0, \\ q_{i+1,j}^n & \text{if } u_{i+1/2,j} \leq 0, \end{cases} \quad (3.1)$$

$$q_{i,j+1/2}^L = \begin{cases} q_{i,j}^n & \text{if } v_{i,j+1/2} > 0, \\ q_{i,j+1}^n & \text{if } v_{i,j+1/2} \leq 0, \end{cases} \quad (3.2)$$

$$F_{i+1/2,j}^L = q_{i+1/2,j}^L u_{i+1/2,j} \Delta y \Delta t, \quad (3.3)$$

$$G_{i,j+1/2}^L = q_{i,j+1/2}^L v_{i,j+1/2} \Delta x \Delta t, \quad (3.4)$$

where subscripts indices  $(i, j)$  denote  $x$  and  $y$  coordinates of a grid cell, respectively.

High-order fluxes are fourth-order accurate (Colella & Sekora, 2008) and computed as follows

$$g_{i+1/2,j}^H = 7/12(q_{i+1,j}^n + q_{i,j}^n) - 1/12(q_{i+2,j}^n + q_{i-1,j}^n), \quad (3.5)$$

$$g_{i,j+1/2}^H = 7/12(q_{i,j+1}^n + q_{i,j}^n) - 1/12(q_{i,j+2}^n + q_{i,j-1}^n), \quad (3.6)$$

$$F_{i+1/2,j}^H = g_{i+1/2,j}^H u_{i+1/2,j} \Delta y \Delta t, \quad (3.7)$$

$$G_{i,j+1/2}^H = g_{i,j+1/2}^H v_{i,j+1/2} \Delta x \Delta t. \quad (3.8)$$

2. Introduce “antidiffusive fluxes” by subtracting the high-order fluxes and low-order fluxes given by

$$A_{i+1/2,j} = F_{i+1/2,j}^H - F_{i+1/2,j}^L, \quad (3.9)$$

$$A_{i,j+1/2} = G_{i,j+1/2}^H - G_{i,j+1/2}^L. \quad (3.10)$$

3. Compute the solution for the next time step using low-order fluxes (transported and diffused) given by

$$q_{i,j}^{td} = q_{i,j}^n - \frac{1}{\Delta x \Delta y} (F_{i+1/2,j}^L - F_{i-1/2,j}^L + G_{i,j+1/2}^L - G_{i,j-1/2}^L). \quad (3.11)$$

4. Limit the antidiffusive fluxes in such way that no new extrema are introduced to the solution. At this point all unphysical oscillations will be cut off so that

$$A_{i+1/2,j}^C = C_{i+1/2,j} A_{i+1/2,j}, \quad 0 \leq C_{i+1/2,j} \leq 1, \quad (3.12)$$

$$A_{i,j+1/2}^C = C_{i,j+1/2} A_{i,j+1/2}, \quad 0 \leq C_{i,j+1/2} \leq 1. \quad (3.13)$$

5. Compute the flux-corrected solution by applying the antidiffusive fluxes to the low-order solution in the form

$$q_{i,j}^{n+1} = q_{i,j}^{td} - \frac{1}{\Delta x \Delta y} (A_{i+1/2,j}^C - A_{i-1/2,j}^C + A_{i,j+1/2}^C - A_{i,j-1/2}^C). \quad (3.14)$$

Finding the appropriate procedure for calculation of the limiting factors  $C_{i+1/2,j}$  and  $C_{i,j+1/2}$  is the most challenging part of the FCT algorithm. Here we used the procedure described by Zalesak (1979):

1. Compute upper  $q_{i,j}^{max}$  and lower  $q_{i,j}^{min}$  bounds on the solution as follows

$$\begin{aligned} q_{i,j}^+ &= \max(q_{i,j}^n, q_{i,j}^{td}), \\ q_{i,j}^{max} &= \max(q_{i-1,j}^+, q_{i,j}^+, q_{i+1,j}^+, q_{i,j-1}^+, q_{i,j+1}^+), \\ q_{i,j}^- &= \min(q_{i,j}^n, q_{i,j}^{td}), \\ q_{i,j}^{min} &= \min(q_{i-1,j}^+, q_{i,j}^+, q_{i+1,j}^+, q_{i,j-1}^+, q_{i,j+1}^+). \end{aligned}$$

2. For the upper bound compute coefficients  $P$ ,  $Q$  and their ratio  $R$ , i.e.,

$$\begin{aligned} P_{i,j}^+ &= \max(A_{i-1/2,j}, 0) - \min(A_{i+1/2,j}, 0) + \max(A_{i,j-1/2}, 0) - \min(A_{i,j+1/2}, 0), \\ Q_{i,j}^+ &= \frac{1}{\Delta x \Delta y} (q_{i,j}^{max} - q_{i,j}^{td}), \\ R_{i,j}^+ &= \begin{cases} \min(1, \frac{Q_{i,j}^+}{P_{i,j}^+}) & \text{if } P_{i,j}^+ > 0, \\ 0 & \text{if } P_{i,j}^+ \leq 0. \end{cases} \end{aligned}$$

3. For the lower bound compute coefficients  $P$ ,  $Q$  and their ratio  $R$ , i.e.,

$$\begin{aligned} P_{i,j}^- &= \max(A_{i+1/2,j}, 0) - \min(A_{i-1/2,j}, 0) + \max(A_{i,j+1/2}, 0) - \min(A_{i,j-1/2}, 0), \\ Q_{i,j}^- &= \frac{1}{\Delta x \Delta y} (q_{i,j}^{td} - q_{i,j}^{min}), \\ R_{i,j}^- &= \begin{cases} \min(1, \frac{Q_{i,j}^-}{P_{i,j}^-}) & \text{if } P_{i,j}^- > 0, \\ 0 & \text{if } P_{i,j}^- \leq 0. \end{cases} \end{aligned}$$

4. Compute the limiting factors

$$\begin{aligned} C_{i+1/2,j} &= \begin{cases} \min(R_{i+1,j}^+, R_{i,j}^-) & \text{if } A_{i+1/2,j} > 0, \\ \min(R_{i,j}^+, R_{i+1,j}^-) & \text{if } A_{i+1/2,j} \leq 0, \end{cases} \\ C_{i,j+1/2} &= \begin{cases} \min(R_{i,j+1}^+, R_{i,j}^-) & \text{if } A_{i,j+1/2} > 0, \\ \min(R_{i,j}^+, R_{i,j+1}^-) & \text{if } A_{i,j+1/2} \leq 0. \end{cases} \end{aligned}$$

### 3.3 Initialization and Boundary Conditions

In the remainder of this thesis we restrict our attention to a parabolically shaped abyssal current located on the western side of the topography and centered at  $x = 0$  km and  $y_0 = 3000$  km, which is approximately  $27^\circ$  N. The height of the inflow current is

$$h(x, y_0) = h_0(x) = \begin{cases} H(1 - (\frac{x}{a})^2) & \text{for } |x| \leq a, \\ 0 & \text{for } |x| > a, \end{cases} \quad (3.15)$$

where  $H$  is the maximum height of the initial current in meters,  $a$  is its half-width in kilometers. The shape of the depth channel is  $h_b = \frac{s}{2l}x^2 - sx$ , where  $s = \frac{1}{2a} \int_{-a}^a h_{b_x} dx$  is the average slope of the topography below the initial inflow current. Estimates for the value of  $s$  can be determined by observations (e.g., Sandoval & Weatherly, 2001). The distance between the center of the current and point of the maximum depth is denoted by  $l$  (see Figure 2.1). The domain used in our numerical simulations along with the location of the boundary conditions is depicted in Figure 3.2.

Previous attempts to numerically simulate cross-equatorial abyssal flows (e.g., Choboter & Swaters, 2000, 2003; Nof & Borisov, 1998; Borisov & Nof, 1998) showed that after the current reaches the equator it moves eastward while oscillating meridionally until reaching the eastern side of the basin. The resulting outflow can move meridionally into either hemisphere. The location and structure of the outflow current is not known in advance, and therefore our boundary conditions should not have any effect on the motion inside of the domain. For these reasons we used open boundary conditions (e.g., Stevens, 1990; Kirkpatrick & Armfield, 2009) for all four boundaries, which means that  $x$ -derivatives and  $y$ -derivatives of the abyssal current height and velocities are equal to zero on the boundaries located at  $y = y_0, -y_0$  and  $x = x_1, x_2$ , respectively.

The shape of the current's height  $h$  at the inflow boundary is given by (3.15). However to initialize the numerical code we also need to know boundary conditions for the other two unknown variables  $u$  and  $v$ . In order to obtain them, we make use of the geostrophic balance approximation, which implies that in mid-latitudes the main balance occurs between the slope-induced gravitational force and the Coriolis force.

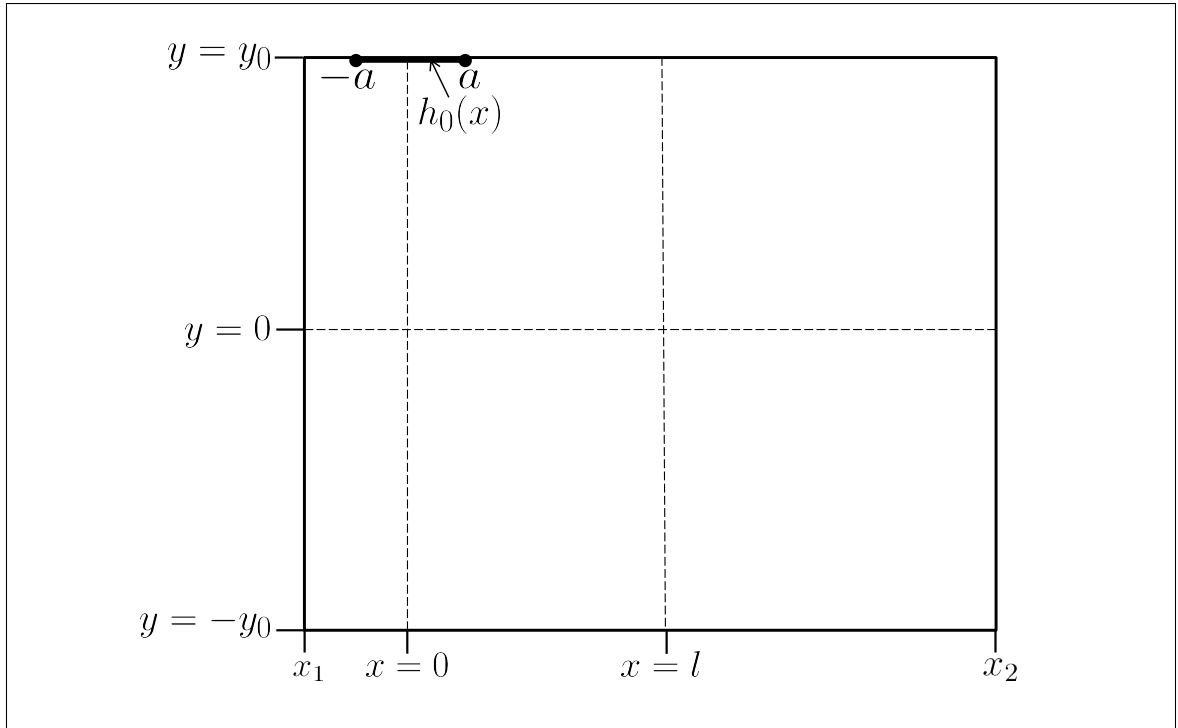


**Figure 3.2:** Domain used in the numerical simulations. The boundaries of the domain are located at  $y = y_0, -y_0$  and  $x = x_1, x_2$ , respectively. The initial current's height  $h_0(x)$  is located at  $y = y_0$  between  $x = -a$  and  $x = a$ . The center of the current is located at  $x = 0$ .  $x = l$  is the distance between the center of the current and point of the maximum depth.

The geostrophic balance equations at  $y = y_0$  are obtained from our system of shallow water equations by neglecting the acceleration terms in the  $x$ - and  $y$ -momentum equations (2.13) and (2.14)

$$\begin{aligned} 2\Omega \sin\left(\frac{y_0}{R}\right)v &= g'(h_b + h)_x, \\ 2\Omega \sin\left(\frac{y_0}{R}\right)u &= -g'(h_b + h)_y. \end{aligned} \tag{3.16}$$

We limit our analysis to topography  $h_b$  that varies only in the zonal direction (i.e.,  $h_b = h_b(x)$ ). Thus the geostrophic equations allow us to complete our set of boundary conditions at  $y = y_0$

$$h(x, y_0) = h_0(x) = \begin{cases} H\left(1 - \left(\frac{x}{a}\right)^2\right) & \text{for } |x| \leq a, \\ 0 & \text{for } |x| > a, \end{cases} \tag{3.17}$$

$$v(x, y_0) = \begin{cases} -v_{\text{Nof}} \frac{(h_b + h_0)_x}{s} & \text{for } |x| \leq a, \\ 0 & \text{for } |x| > a, \end{cases} \tag{3.18}$$

$$u(x, y_0) = 0, \tag{3.19}$$

in which we have defined

$$v_{\text{Nof}} = -\frac{g's}{f_0} \tag{3.20}$$

to be the Nof-velocity that is determined by a balance between the Coriolis and the gravitational forces on a slope  $s$  at the initial latitude  $y = y_0$  where the Coriolis parameter is  $f_0 = 2\Omega \sin(y_0/R)$ .

### 3.4 Default set of parameter values

In this thesis, unless otherwise specified, we will use the parameter values given in Table 3.1. These values are estimated from observations (e.g., Sandoval & Weatherly, 2001; De Madron & Weatherly, 1994; Amante & Eakins, 2009).

Variable	Description	Value
$H$	maximum current's height	200 m
$a$	current's half-width	80 km
$s$	average slope below the current	$6 \times 10^{-3}$
$l$	distance between the center of the current and point of the maximum depth	1000 km
$g'$	reduced gravity	$8 \times 10^{-4}$ m/s
$\Omega$	angular speed of the Earth's rotation	$7.29 \times 10^{-5}$ rad/s
$\nu$	viscosity coefficient	$100 \text{ m}^2/\text{s}$
$R$	radius of the Earth	6371 km
$\phi_0$	initial latitude	27° N
$y_0$	$y_0 = \phi_0 R$	3000 km
$x_1$	western boundary of the domain	-500 km
$x_2$	eastern boundary of the domain	2500 km

Table 3.1: Default values of parameters

## Chapter 4

# Comparison of Numerical Solution with Two Exact Solutions

In this chapter we will compare the results of the numerical simulations against two exact solutions. In order to do that, a preliminary analysis of the governing equations needs to be performed. First the steady solution of the model equations based on an  $f$ -plane approximation is found. Despite the fact that this approximation is not realistic throughout the entire domain because of the variability of the Coriolis parameter,  $f$ , with latitude, it does provide an analytical solution that serves as a starting point to verify that the developed numerical method is consistent with an analytical prediction. As shown in section 4.1, the maximum discrepancy (around 10%) between the numerical and exact solutions occurs near the groundings of the current. The discrepancy decreases down to 1% as we move closer to the central axis of the current.

Next we compare the numerical solution of the fully nonlinear equations to the solution of the steady planetary geostrophic equations (Vallis, 2006). This model corresponds mathematically to a quasi-linear hyperbolic partial differential equation and can be solved explicitly (Swaters, 2006, 2013). In section 4.2 we show that the two solutions are in good agreement in the region between the initial latitude  $27^\circ$  N down to approximately  $6^\circ$  N. After that point the discrepancy grows rapidly as the current moves in the equatorward direction. This is not surprising since the planetary geostrophic model approximation breaks down in the vicinity of the equator.

## 4.1 Steady solution of governing SWE on an $f$ -plane

Under the  $f$ -plane approximation introduced in section 2.1 and the assumption that the topography does not change in the meridional direction (i.e.  $h_{b_y} = 0$ ) our fully non-linear system of shallow water equations (2.13),(2.14) and (2.15) becomes

$$u_t + uu_x + vu_y - f_0v = -g'(h_b + h)_x, \quad (4.1)$$

$$v_t + uv_x + vv_y + f_0u = -g'h_y, \quad (4.2)$$

$$h_t + (hu)_x + (hv)_y = 0. \quad (4.3)$$

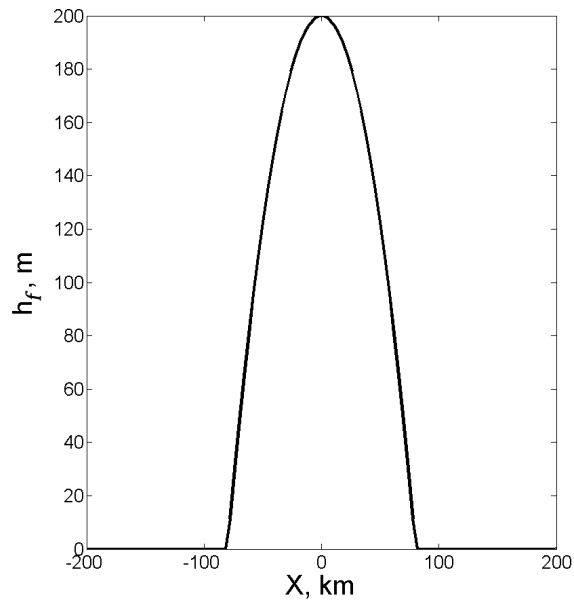
in which  $f_0 = 2\Omega \sin(\frac{y_0}{R})$  is the Coriolis parameter at  $y_0$ . This system has an exact analytic solution

$$h_f(x) = \begin{cases} H(1 - (\frac{x}{a})^2) & \text{for } |x| \leq a \\ 0 & \text{for } |x| > a \end{cases}, \quad (4.4)$$

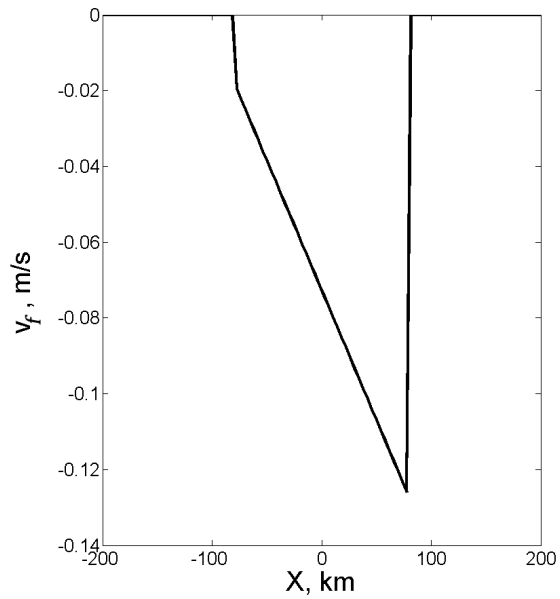
$$v_f(x) = \begin{cases} -v_{\text{Nof}} \frac{(h_b + h_f)_x}{s} & \text{for } |x| \leq a \\ 0 & \text{for } |x| > a \end{cases}, \quad (4.5)$$

$$u_f(x) = 0. \quad (4.6)$$

in which  $v_{\text{Nof}}$  is given by (3.20) and  $s$  is the slope beneath the current at  $x = 0$ . That is, the boundary conditions set at  $y = y_0$  as in (3.17)-(3.19) extend uniformly for all  $y$ . Explicitly, for the physical parameters introduced in Table 3.1, we have that  $|h_{b_x}| > |h_{f_x}|$  and calculation of the meridional velocity  $v_f$  shows that it is strictly negative for  $|x| \leq a$ . Figure 4.1 shows the cross-section views of the current's height  $h_f$  of the  $f$ -plane and its corresponding meridional velocity  $v_f$ . The zonal velocity  $u_f$  is equal to zero throughout the entire domain. This solution represents a deep western boundary current that flows equatorward without changing its shape and position, i.e. it is  $y$ -independent.



(a) Cross-section view,  $h_f$



(b) Cross-section view,  $v_f$

**Figure 4.1:** Cross-sections of the exact analytic solutions  $h_f$  ((4.4)) and  $v_f$  ((4.5)) to the model equations assuming an  $f$ -plane approximation. (a) Cross-section view of the height  $h_f$ . (b) Cross-section view of the meridional velocity  $v_f$ .

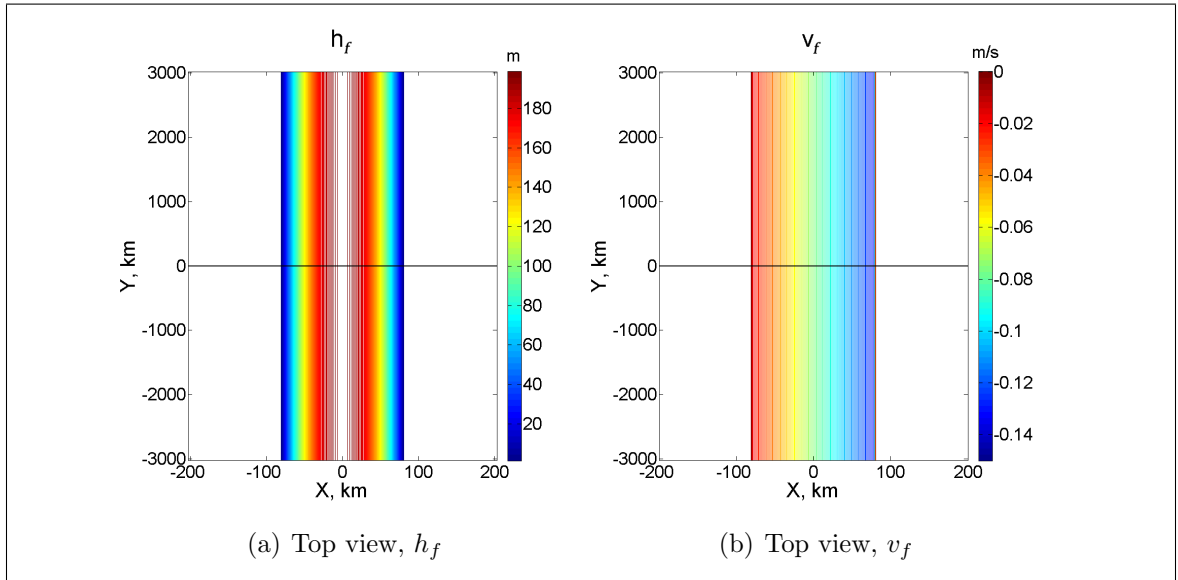


**Figure 4.2:** Contour plots of the analytical solution to the f-plane equations with  $l = 1000 \text{ km}$ . (a) Current height,  $h_f$ . and (b) Current meridional velocity,  $v_f$ .

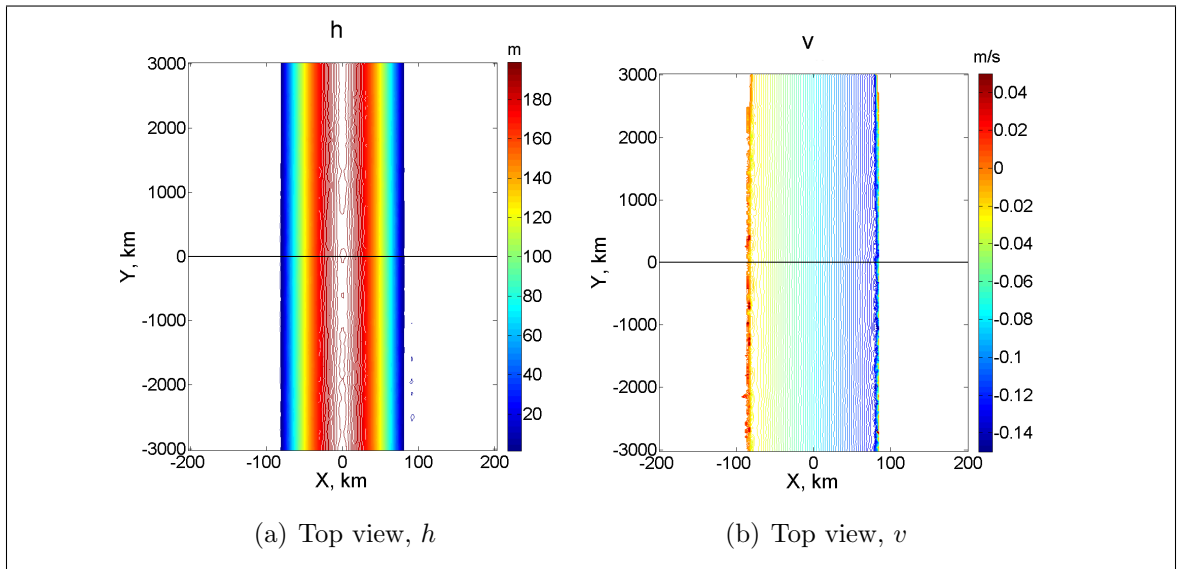


**Figure 4.3:** As in 4.2 but showing the contour plots of the numerical solution of the fully nonlinear equations on the f-plane.

To obtain the numerical solution we used the procedure described in chapter 3 to solve (4.1), (4.2) and (4.3) with the boundary conditions  $h(x, y_0) = h_f(x)$ ,  $u(x, y_0) = u_f(x)$  and  $v(x, y_0) = v_f(x)$  in (3.17)-(3.19). The contour plots of the numerical and analytical solutions are depicted in Figures 4.2 and 4.3, respectively. In spite of a very good agreement between the two solutions, there are some distortions observed in the numerically obtained results that will be addressed later.

As a measure of the errors between the exact analytical  $h_f, u_f, v_f$  solutions and the numerical  $h, u, v$  solutions, we chose the following quantities:

- $\tilde{h} = \left| \frac{h_f - h}{H} \right|$  is the difference between the heights  $h_f$  and  $h$  normalized by the maximum current height  $H$  at the northern boundary.
- $\tilde{u} = \left| \frac{u_f - u}{v_{\text{Nof}}} \right|$  is the difference between the eastward velocities  $u_f$  and  $u$  normalized by the Nof velocity  $v_{\text{Nof}}$ .
- $\tilde{v} = \left| \frac{v_f - v}{v_{\text{Nof}}} \right|$  is the difference between the northward velocities  $v_f$  and  $v$  normalized by the Nof velocity  $v_{\text{Nof}}$ .

It can be observed that the errors in heights near the upslope ( $x \simeq -80$  km) grounding (Figure 4.4(a)) and along the central axis of the current ( $x \simeq 0$  km) (Figure 4.4(b)) reach around 1%. On the other hand, the numerically calculated eastward and northward velocities display a significant decrease in errors (from 18% to 1% and from 16% to 1% for  $\tilde{u}$  and  $\tilde{v}$ , respectively) when we move away from the upslope grounding closer to the central axis (Figures 4.4(c), 4.4(d), 4.4(e) and 4.4(f)).

Figures 4.5(b), 4.5(d) and 4.5(f) show errors between the heights and the velocities on the equatorial west-to-east cross-section. Figures 4.5(a), 4.5(c) and 4.5(e) are the same except that the cross-section is taken along the southern boundary  $y = -y_0$ . All of these figures indicate that the errors near the downslope grounding ( $x = 80$  km) are of the same order as the ones near the upslope grounding ( $x = -80$  km).

We observed that the errors grow as we move closer to the groundings, where  $v$  is discontinuous and  $h$  is not smooth. This can be explained by the fact that near sharp gradients the FCT algorithm resembles the low-order scheme (Boris & Book,

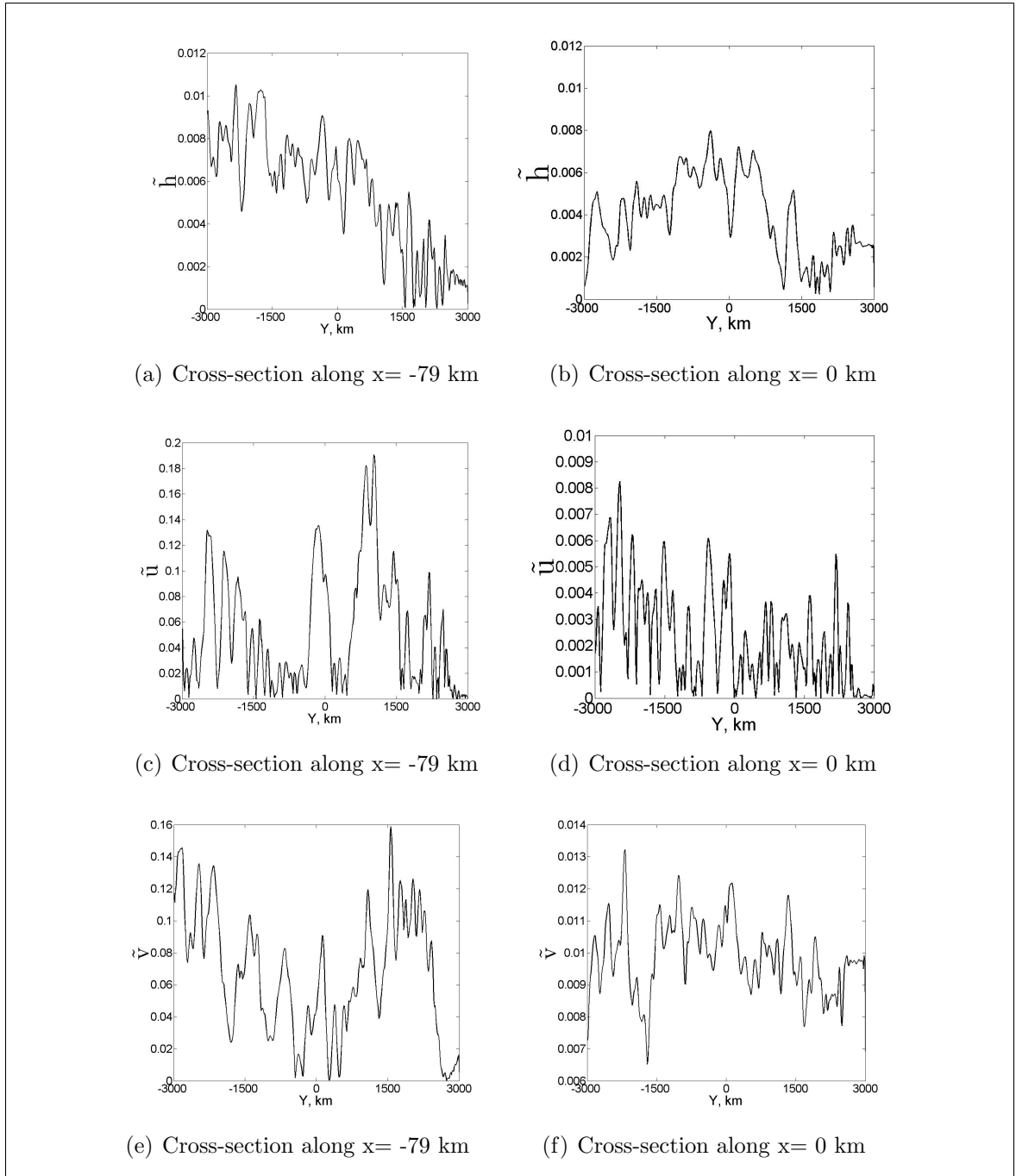


**Figure 4.4:** The errors between the exact analytical  $h_f, u_f, v_f$  and numerical  $h, u, v$  solutions along constant longitudes (constant  $x$ ). (a)  $\tilde{h}$  along  $x = -79$  km, (b)  $\tilde{h}$  along  $x = 0$  km, (c)  $\tilde{u}$  along  $x = -79$  km, (d)  $\tilde{u}$  along  $x = 0$  km, (e)  $\tilde{v}$  along  $x = -79$  km and (f)  $\tilde{v}$  along  $x = 0$  km.

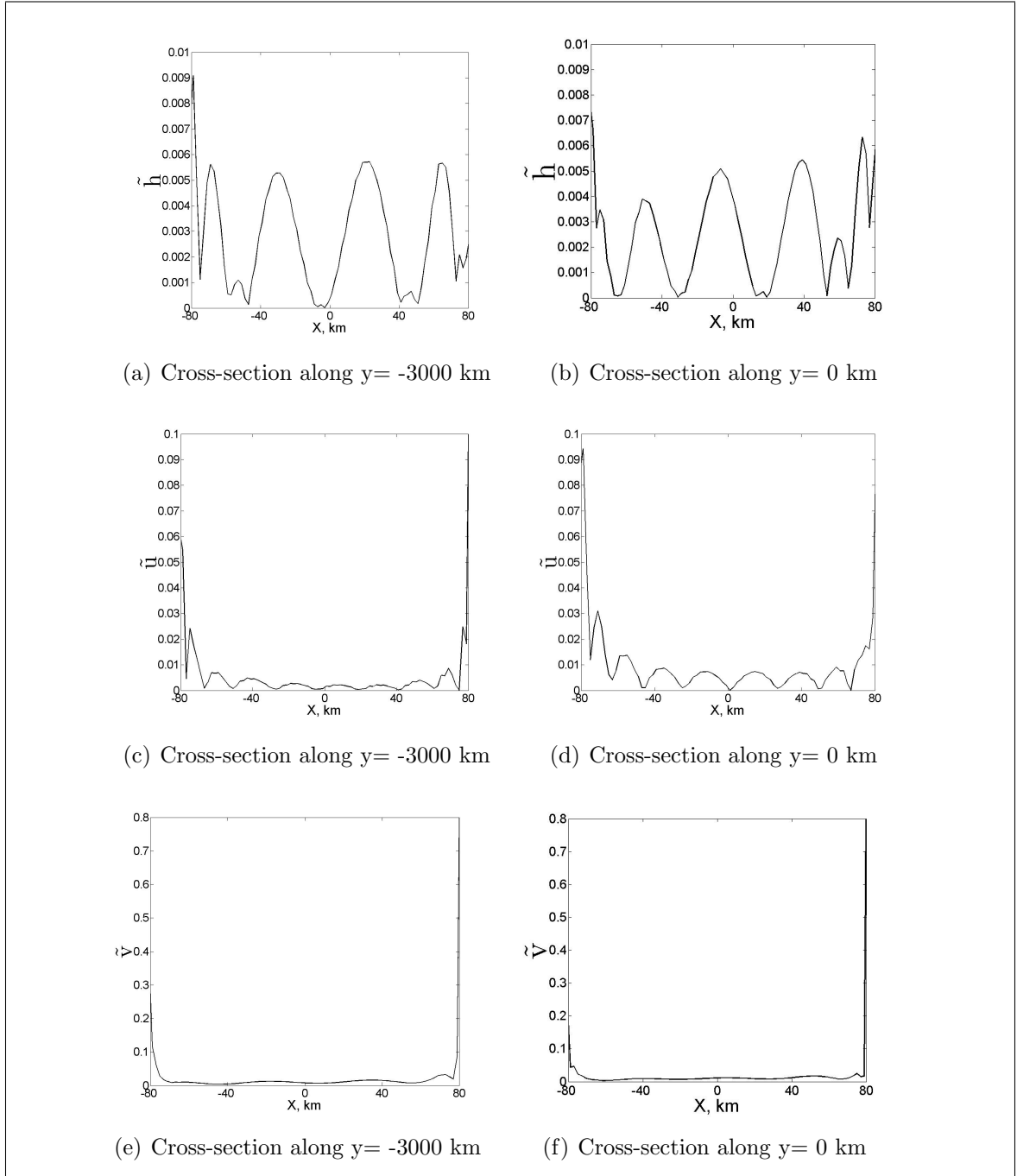


**Figure 4.5:** The errors between the exact analytical  $h_f, u_f, v_f$  and numerical  $h, u, v$  solutions along constant latitudes (constant  $y$ ). Figures indicate that the errors near the downslope grounding ( $x = 80$  km) are of the same order as the ones near the upslope grounding ( $x = -80$  km). (a)  $\tilde{h}$  along  $y = -3000$  km, (b)  $\tilde{h}$  along  $y = 0$  km, (c)  $\tilde{u}$  along  $y = -3000$  km, (d)  $\tilde{u}$  along  $y = 0$  km, (e)  $\tilde{v}$  along  $y = -3000$  km and (f)  $\tilde{v}$  along  $y = 0$  km.

1973; Kuzmin *et al.*, 2005), which does not have high resolving properties, but allows the algorithm not to introduce unphysical values.

## 4.2 Planetary Geostrophic Model

In section 3.3 we introduced the geostrophic approximation to the momentum conservation equations. Assuming a geostrophic balance and steady-state solutions, we arrive at the planetary geostrophic model equations given by

$$f(y)v = g'(h_b + h)_x, \quad (4.7)$$

$$f(y)u = -g'h_y, \quad (4.8)$$

$$(hu)_x + (hv)_y = 0. \quad (4.9)$$

where now the Coriolis parameter  $f(y) = 2\Omega \sin(\frac{y}{R})$  is a function of meridional distance. Eliminating  $v$  and  $u$  in (4.9) using (4.7) and (4.8) yields

$$\tan\left(\frac{y}{R}\right)Rh_y - \frac{h}{h_{b_x}}h_x = h. \quad (4.10)$$

This quasi-linear hyperbolic partial differential equation has an exact explicit solution which was derived by Swaters (2006, 2013). First, given the initial current height  $h_0(\tau(x, y_0))$  the following equation

$$h_b(\tau) + \frac{\sin(y_0/R) - \sin(y/R)}{\sin(y_0/R)}h_0(\tau) = h_b(x), \quad (4.11)$$

needs to be solved for  $\tau(x, y)$  given  $(x, y)$ . Given  $\tau$ , the current height  $h_p(x, y)$  is determined from

$$h_p(x, y) = \frac{\sin(y/R)}{\sin(y_0/R)}h_0(\tau). \quad (4.12)$$

The corresponding meridional and zonal velocity components determined from (4.7) and (4.8), respectively, are

$$\begin{aligned} v_p &= \frac{g'(h_b + h)_x}{f(y)} = \frac{g'(h'_b(\tau) + h'(\tau))\tau_x}{f(y)}, \\ u_p &= -\frac{g'h_y}{f(y)} = -\frac{g'h'(\tau)\tau_y}{f(y)}. \end{aligned} \quad (4.13)$$

Figures 4.6 and 4.7 show the heights  $h_p$  and  $h$  obtained from the geostrophic model approximation and fully nonlinear numerical simulations, respectively. According to Figure 4.8(a) the height  $h_p$  along its central axis ( $x = 0$  km) decreases with latitude almost linearly. The same can be observed for the height  $h$  obtained numerically (Figure 4.8(b)) with the exception for a small region close to the equator ( $y = 0$  km). The normalized difference  $\tilde{h} = \frac{|h-h_p|}{H}$  is shown in Figure 4.9.

It can be observed that the two solutions  $h_p$  and  $h$  are in good agreement in the region between the initial location  $y_0 = 3000$  km ( $27^\circ$  N) down to approximately  $y = 700$  km ( $6^\circ$  N), where the error  $\tilde{h} = \frac{|h-h_p|}{H}$  does not exceed 3%. Then the discrepancy grows rapidly as the current approaches the vicinity of the equator. In this region the groundings of the numerically calculated height turn rapidly in the downslope direction, while the groundings of  $h_p$  do not change their location. The comparison of the velocity components also showed significant disagreement in the equatorial region. The large discrepancy is expected since the geostrophic assumptions are no longer valid in the vicinity of the equator where  $f(y)$  becomes vanishingly small (e.g., Nof & Borisov, 1998; Edwards & Pedlosky, 1998; Swaters, 2006, 2013).

It is important to highlight some properties that the two solutions share:

- 1 There is almost no change in the location of the groundings in the numerical solution  $h$  far from the equator. This fact is consistent with the predictions given by geostrophic model in (Swaters, 2006, 2013). The analysis of that model indicates that once the location of the groundings is set by the initial conditions, it does not change with latitude.
- 2 Both solutions show decrease in thickness of the current as the current approaches the equator.
- 3 The maximum height of the current moves slightly up slope as it approaches the equator.

The most crucial difference between the two solutions is that unlike the numerical solution  $h$ , the planetary geostrophic current  $h_p$  does not experience the eastward

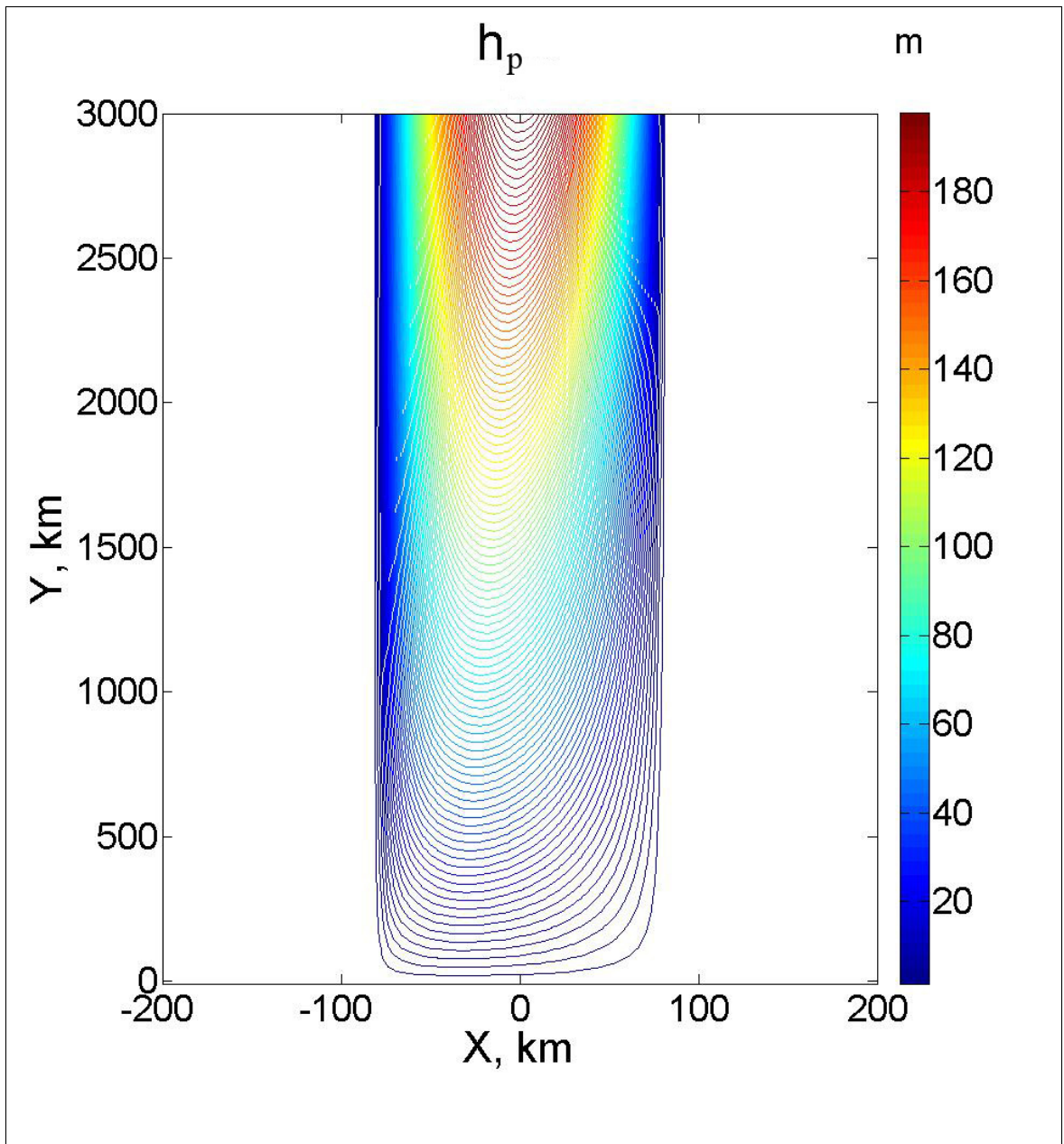


**Figure 4.6:** Contour plot of the current's height determined from the geostrophic model equations  $h_p$  (Swaters, 2006, 2013).

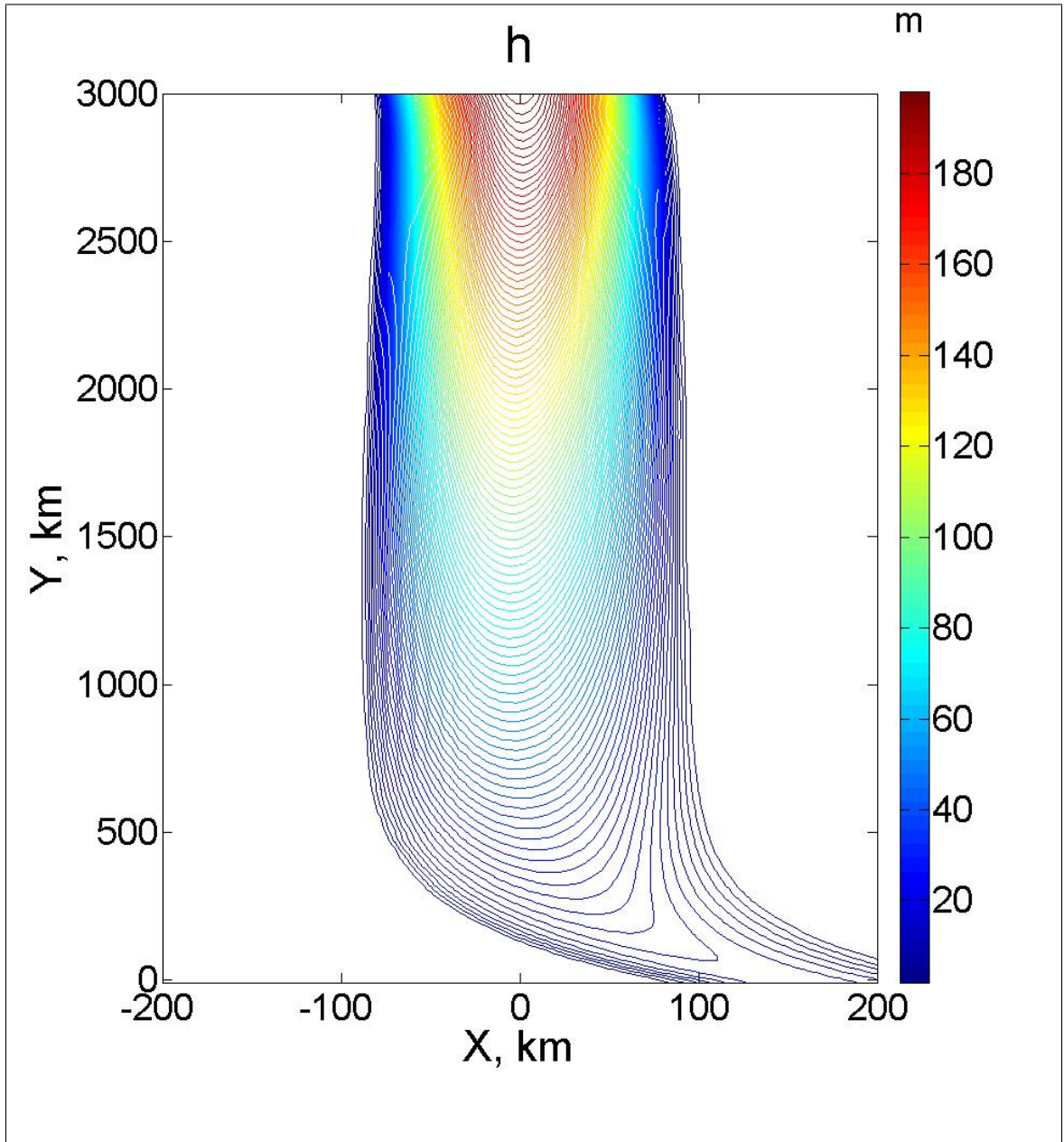


**Figure 4.7:** Contour plot of the current's height  $h$  obtained from the numerical simulations.

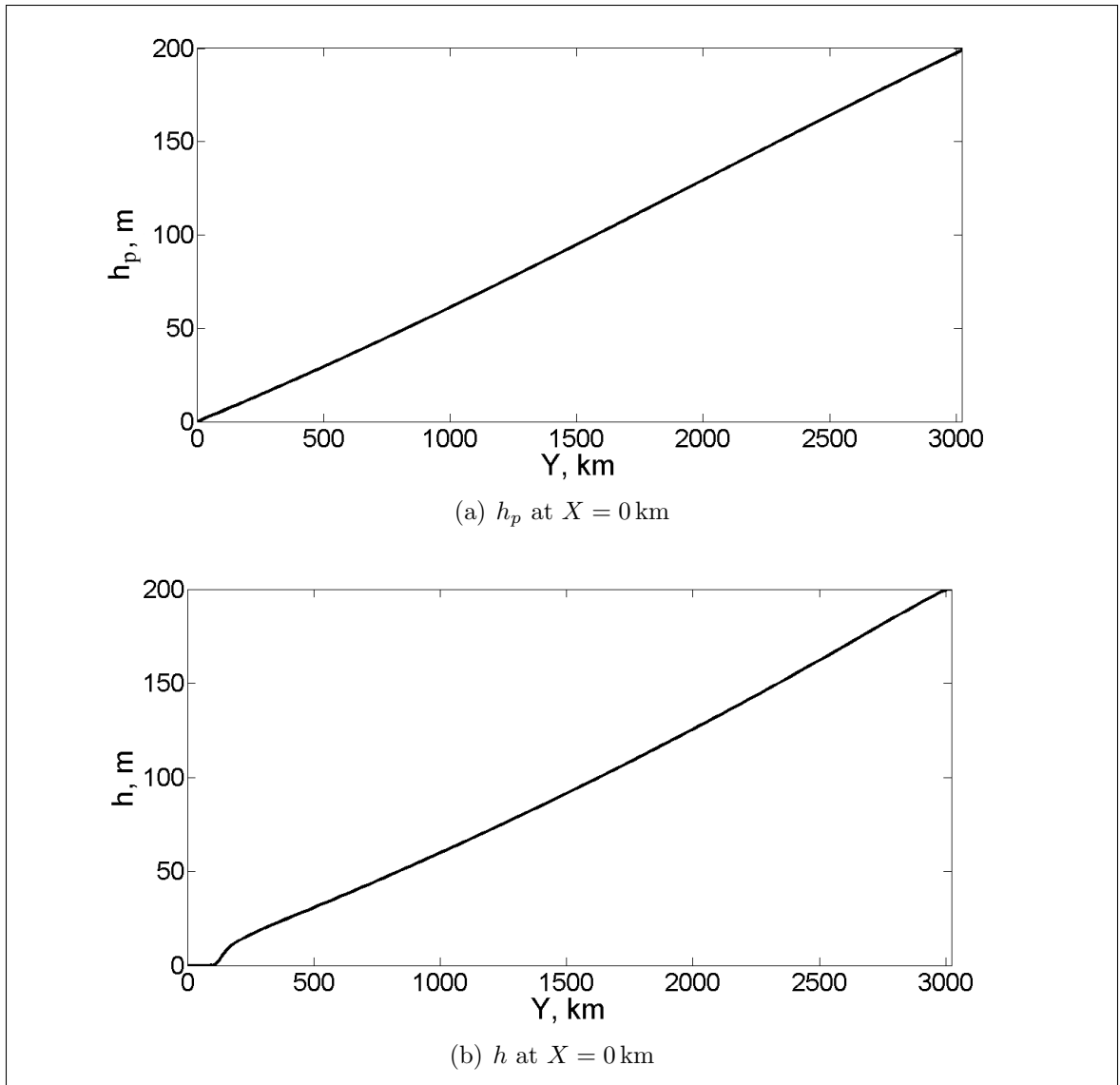


**Figure 4.8:** Heights  $h_p$  and  $h$  at  $x = 0$  km vs.  $y$ , the meridional distance from the equator.

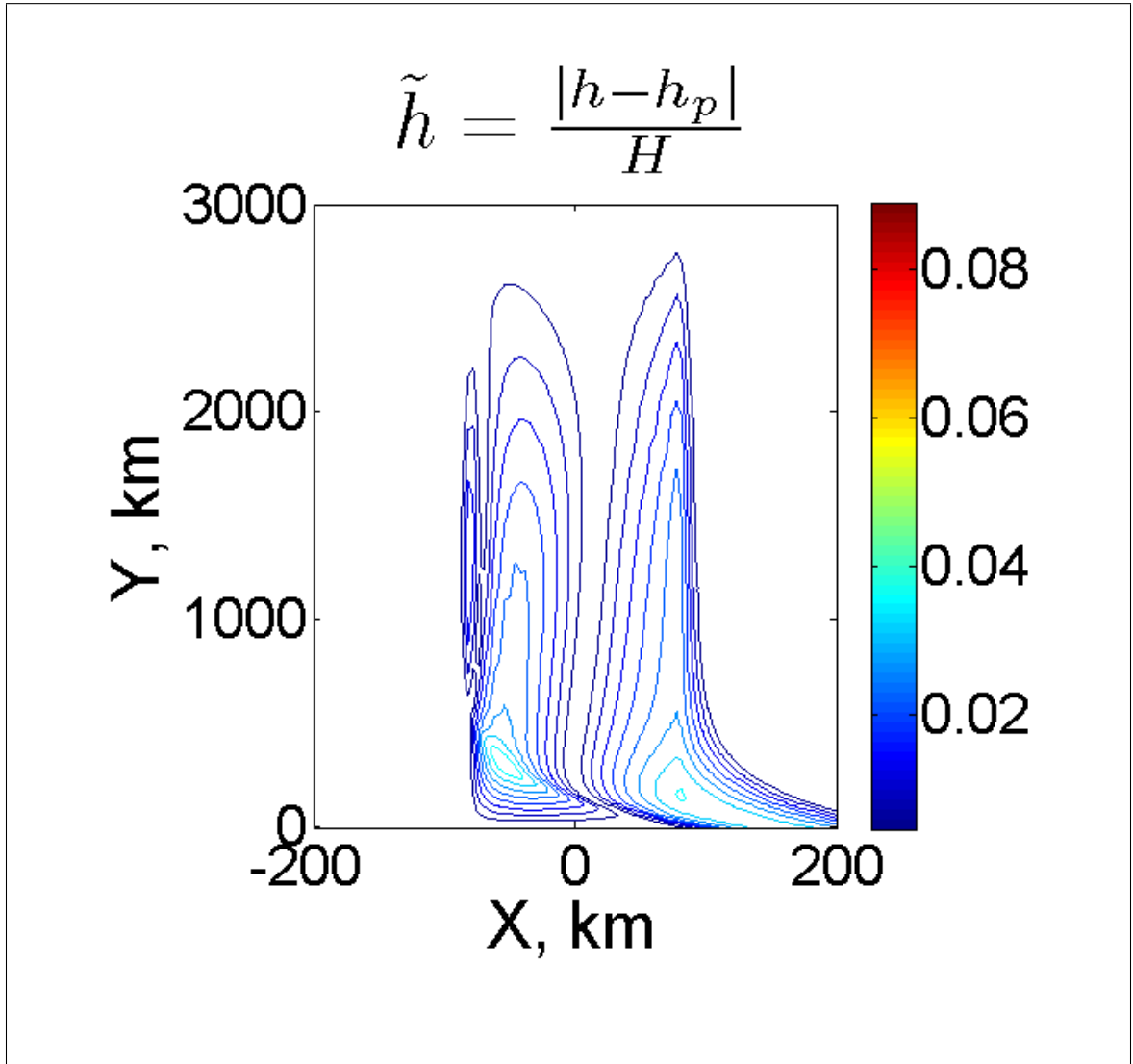


**Figure 4.9:** Difference between the numerical solution  $h$  and geostrophic model solution  $h_p$  normalized by  $H$ .

turning in the vicinity of the equator. Thus geostrophic model can not be used to describe the cross-equatorial flow of grounded abyssal currents. However the above comparison successfully confirmed that the developed numerical procedure captures important properties of the previously known analytical results.

# Chapter 5

## Results and Discussion

### 5.1 Numerical Simulations of a Grounded Abyssal Current Approaching the Equator

We started our analysis by using the numerical procedure presented in chapter 3 to solve (2.16) subject to the boundary conditions derived in section 3.3 assuming the geostrophic approximation. The boundary values are computed according to (3.17), (3.18) and (3.19) using the default set of physical parameters (Table 3.1). These are the same as those used in the plot shown in Figure 4.1. Figure 5.1 shows the contour plots of the heights  $h$  at different times ( $t=197, 255, 347$  and  $428$  days) after the initialization ( $t=0$  days) with the default parameters.

During the first stages of its motion the current is seen to propagate along the continental slope with almost no change in the location of its groundings (Figure 5.1(a)). Upon entering the equatorial region the fluid forms a narrow current where frictional effects play a non-negligible role. The current slightly overshoots the equator while it slides in the downslope direction, then it gradually returns back to the northern hemisphere as it passes the line of the maximum depth at  $x = 1000$  km. Subsequently, the fluid rises up on the opposite side of the topography and begins to head southward as it reaches the point of a maximum run-up (easternmost point in the equatorial region) (Figure 5.1(b)). Thereafter the current increases its height and width as it leaves the vicinity of the equator (Figure 5.1(c)). In this simulation the entire current eventually ends up propagating southward on the eastward side of the

topography in the southern hemisphere (Figure 5.1(d)).

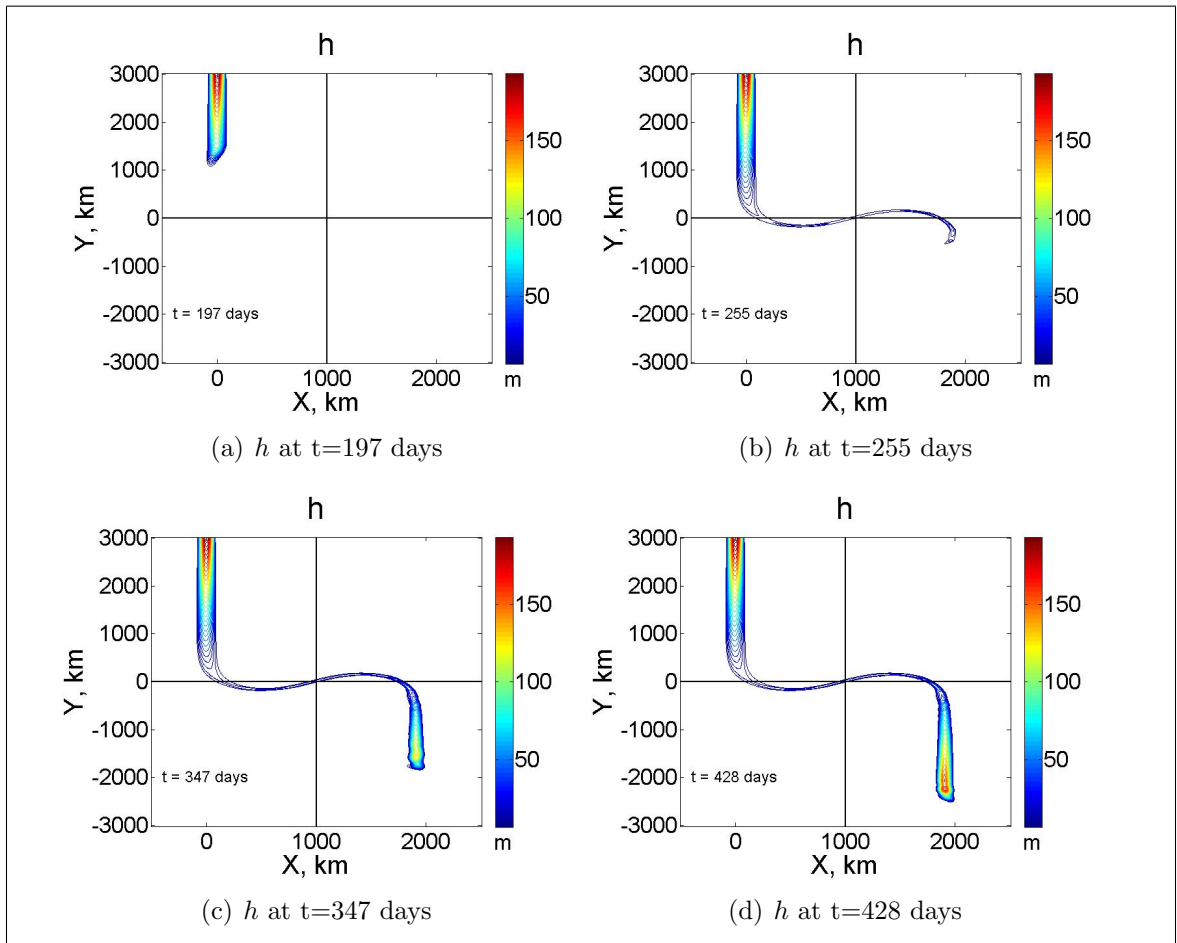


**Figure 5.1:** Experiment with the default initialization parameters:  $H_0 = 200$  m,  $a_0 = 80$  km,  $s_0 = 6 \times 10^{-3}$ ,  $l_0 = 1000$  km,  $g'_0 = 8 \times 10^{-4}$  m/s<sup>2</sup>,  $\Omega_0 = 7.29 \times 10^{-5}$  rad/s and  $R_0 = 6371$  km. The horizontal line represents the equator. The vertical line represents the location of the channel's axis at greatest depth. Figures (a) to (d) show the contour of the height  $h$  at different times: (a)  $h$  at  $t=231$  days, (b)  $h$  at  $t=255$  days, (c)  $h$  at  $t=347$  days, and (d)  $h$  at  $t=428$  days.

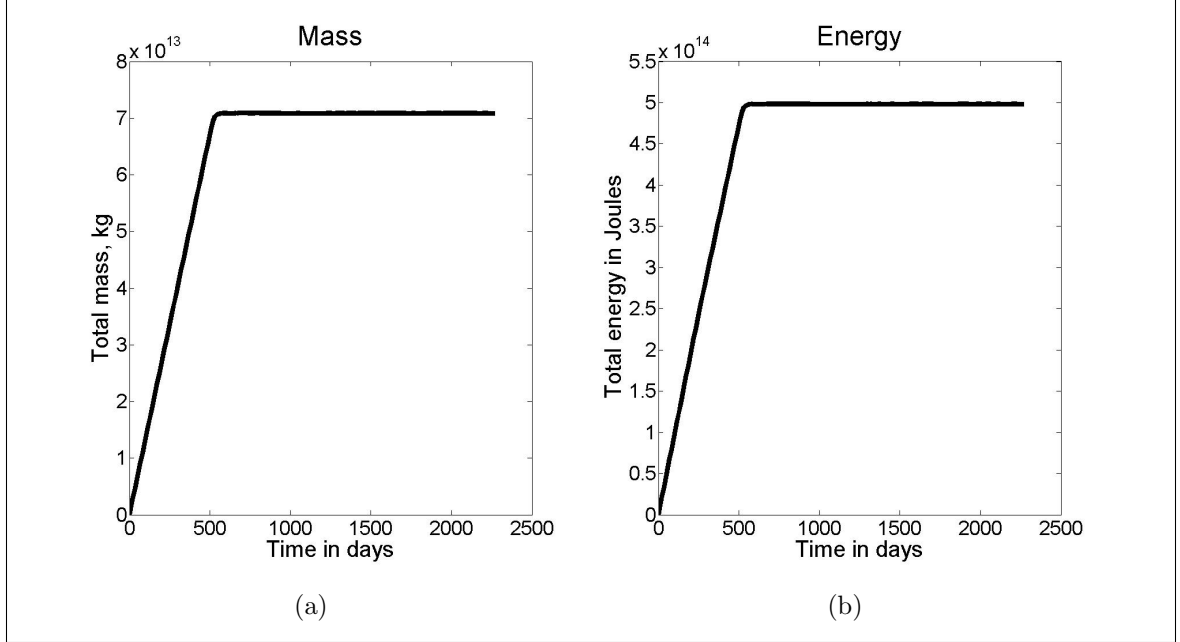


**Figure 5.2:** Experiment with the physical parameters set to their default values. (a) Total mass of fluid in the current vs. time. (b) Total energy vs. time.

The increase of the total energy and mass of the current with time within the computational domain is shown in Figure 5.2. Both graphs show almost linear growth until  $t \approx 500$  days, when the flow reaches the southern boundary at the eastern side of the channel. After this moment we consider the current to be at a near steady state, which is characterized by constant values of mass and energy in the domain between  $y = -3000$  km and  $y = 3000$  km.

The contour plots of the solutions  $h$ ,  $u$  and  $v$  after the current has reached the constant energy level are depicted in Figures 5.3, 5.4 and 5.5, respectively. It is observed that in the northern hemisphere the thickness of the abyssal current decreases with decreasing latitude almost linearly, as was mentioned in section 4.2. In the immediate vicinity of the equator between approximately  $y = -300$  km and  $y = 300$  km the height of the current does not exceed 20 m. At the same time the eastward velocity,  $u$ , experiences a significant increase on the western side of the channel, reaches its maximum value in the equatorial region of approximately 2 m/s, and then decreases as the fluid approaches the eastern side of the channel. The northward velocity, on the other hand, changes its value in the range between  $-1.5$  m/s and 1.5 m/s as the

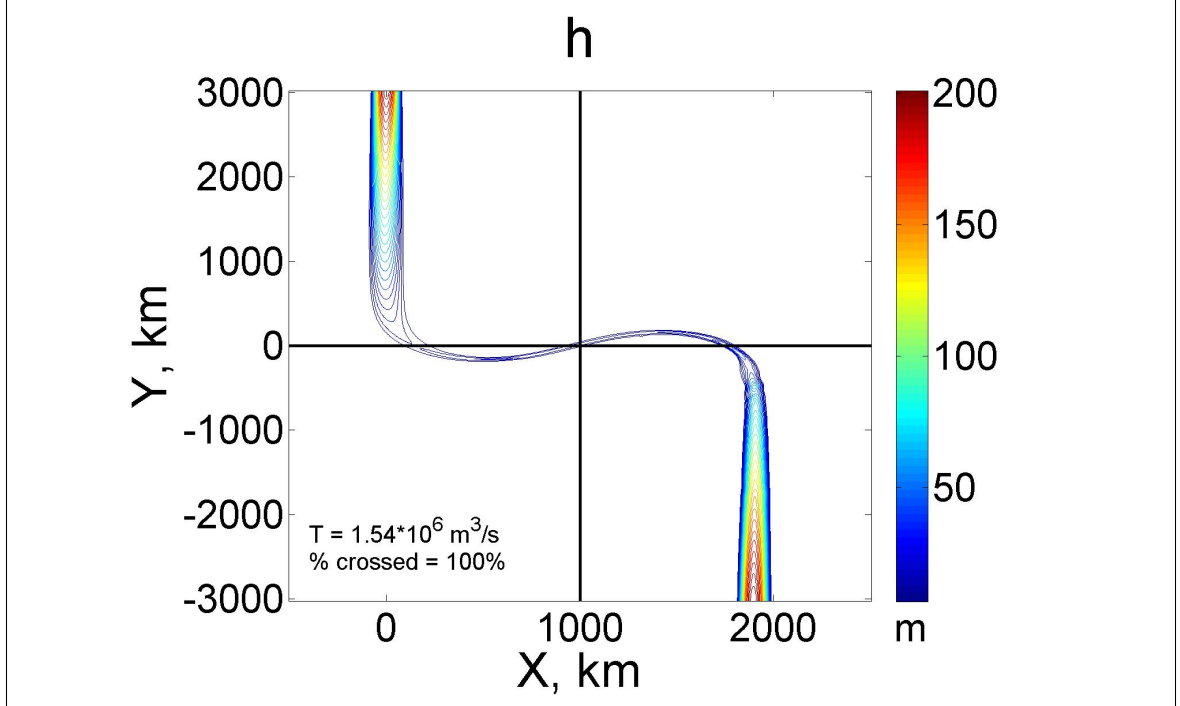


**Figure 5.3:** Contour plot of the current’s height  $h$  after the current has reached the state of constant energy. The physical parameters are set to their default values as given in Figure 5.1

fluid travels along the equator. In comparison, the average southward speed of the incident current at the northern boundary is 0.08 m/s.

Several other experiments were conducted by changing the value of only one parameter and holding the rest of them equal to their default values. This way we could isolate the effect of each parameter on the behaviour of the current.

The meandering of the flow along the equator was observed in all numerical simulations. Hereafter, we refer to this meandering as the “zonal wave”. As will be shown later, the wavelength of this zonal wave plays a key role in determining into what hemisphere the current will propagate after its ascent up the eastern slope of the channel.

For Figures 5.1-5.5 the reduced gravity is equal to the default value of  $g'_0 = 8 \times 10^{-4} \text{ m/s}^2$ . Next we analysed the effect of this parameter on the structure of the flow. Varying the reduced gravity in the range between  $2 \times 10^{-4}$  and  $32 \times 10^{-4} \text{ m/s}^2$  resulted in the steady solutions for the current’s height shown in Figure 5.6. For

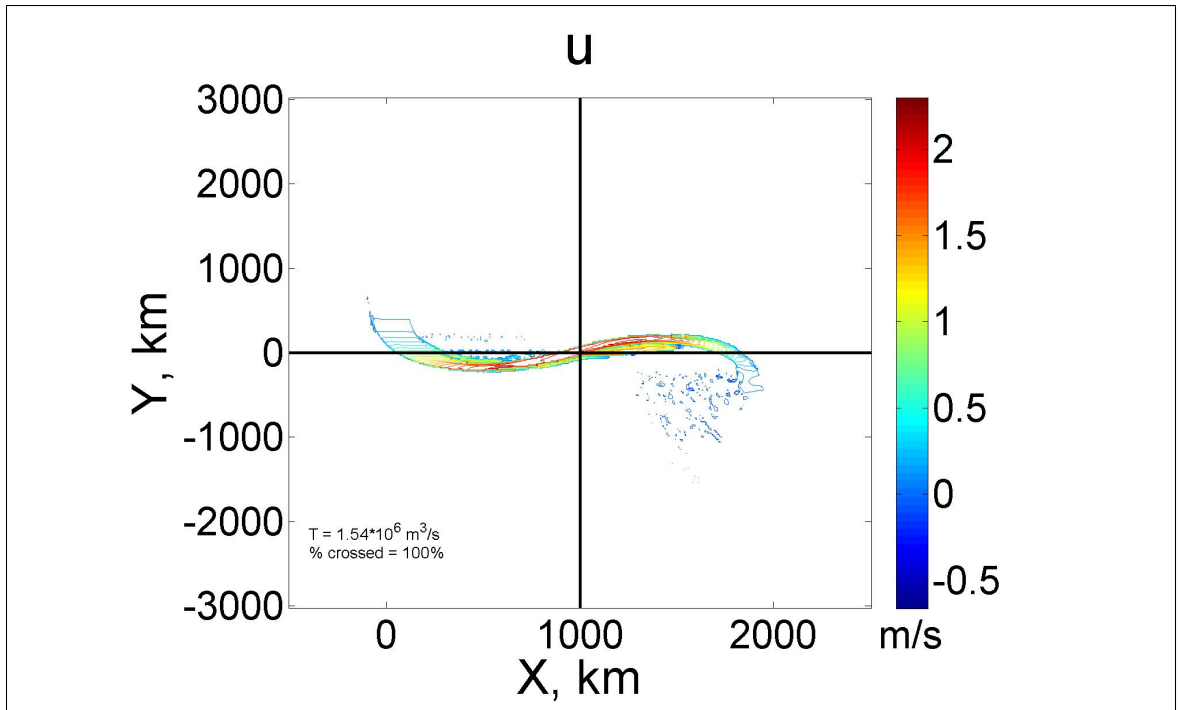


**Figure 5.4:** Contour plot of the current's eastward velocity  $u$  after the current has reached the state of constant energy. The physical parameters are set to their default values as given in Figure 5.1

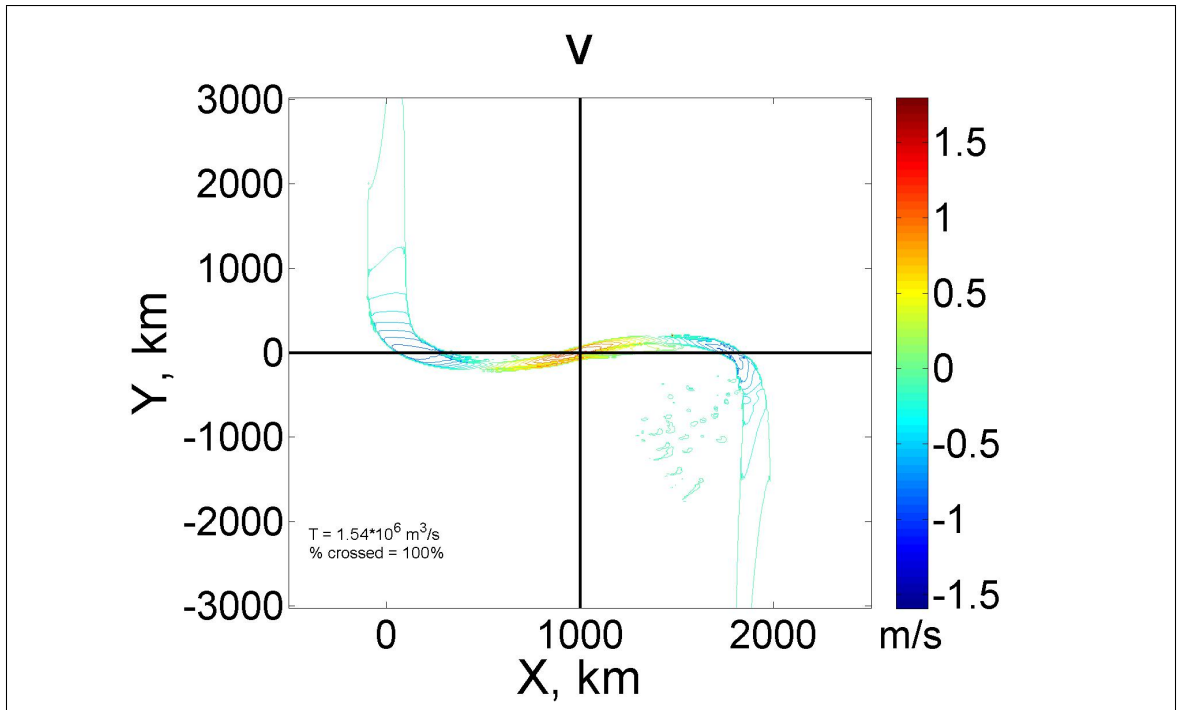


**Figure 5.5:** Contour plot of the current's northward velocity  $v$  after the current has reached the state of constant energy. The physical parameters are set to their default values as given in Figure 5.1

each of the 4 experiments, values of the reduced gravity, inflow volume transport and fraction  $T_s$  of the source meridional volume flux that ultimately crossed the southern boundary are presented in Table 5.1. Explicitly,

$$T_s = \frac{\int_{x^1}^{x^2} h(x, -y_0)v(x, -y_0)dx}{\int_{-a}^a h(x, y_0)v(x, y_0)dx}. \quad (5.1)$$

It is found that for some values of the reduced gravity the structure of the current after its interaction with the equator is completely different from the one presented in Figure 5.3. For example, decreasing the reduced gravity by a factor of 4 compared to the default value of  $g'_0 = 8 \times 10^{-4} \text{ m/s}^2$  (Figure 5.6(a)) made the entire current recirculate back to the northern hemisphere.

For  $g' = 2.7 \times 10^{-4} \text{ m/s}^2$  (Figure 5.6(b)) we observe the transitional regime which is characterized by the splitting of the current in two parts after it reaches the maximum run-up point on the eastern side of the channel. The current partially penetrates the southern hemisphere with the remainder returning back to the northern hemisphere. In general, our simulations indicated that, if the splitting does take place, the amounts of fluid that ends up in either hemisphere are very rarely equal.

In most simulations we find the current exits either entirely northward or southward. For example, when  $g' = 4 \times 10^{-4} \text{ m/s}^2$  (Figure 5.6(c)), the current exits entirely to the south as in the experiment with the default parameter values. In this case the picture is not as symmetric because the fluid experiences minor zonal oscillations perpendicular to the direction of the current's propagation after leaving the equatorial region. These oscillations originate when the incident current overshoots the position of geostrophic equilibrium. If the fluid finds itself to be higher upslope than this position, the gravity force acting on it becomes greater than the Coriolis force, therefore making the fluid slide down the slope. Due to inertia, the fluid overshoots the equilibrium position so that the Coriolis force exceeds the gravity force. This process repeats itself until the oscillations disappear due to the process of viscous relaxation. The bulk of the current continues southward with little change in the location of its groundings, similar to the motion of the incident current in the northern hemisphere.

High values of the reduced gravity (Figure 5.6(d)) make the outflow current switch from the southern hemisphere to the northern hemisphere. In this case the oscillations of the current as it moves in the northward direction are distinct and are not fully damped by the time the current reaches the northern boundary.

The results of several numerical simulations with different values of the reduced gravity  $g'$  are summarized by Figure 5.7, which shows the computed southward transmission coefficient,  $T_s$ , versus the reduced gravity  $g'$ . The plot clearly shows a step-like transition from  $T_s \approx 0\%$  to  $T_s \approx 100\%$ , and from  $T_s \approx 100\%$  to  $T_s \approx 0\%$  for  $g' \approx 4 \times 10^{-4} \text{ m/s}^2$  and  $g' \approx 17 \times 10^{-4} \text{ m/s}^2$ , respectively. We note that the zonal wave increases in wavelength so that a smaller number of waves span the domain as  $g'$  increases in this channel of fixed zonal extent. In the analysis that follows, we will show that the ratio of zonal wavelength to zonal extent determines the transition in  $T_s$ .

Numerical simulations were also performed by individually varying other physical parameters (default values are given in Table 3.1). Contours of the current's height in steady-state and of southward transmission coefficients  $T_s$  are shown for simulations with varying slope,  $s$  (Figures 5.8, 5.9), planetary rotation,  $\Omega$  (Figures 5.10, 5.11), zonal channel extent,  $l$  (Figures 5.12, 5.13), planetary radius,  $R$  (Figures 5.14, 5.15), incident current half-width,  $a$  (Figures 5.16, 5.17) and incident current height,  $H$  (Figures 5.18, 5.19).

All our simulations indicated that the value of the meridional velocity  $v$  on the eastern slope is rarely zero and plays an important role in determining into what hemisphere the current will penetrate. If the current close to where it completes its ascent up the eastern slope of the channel is heading northward, then it continues northward to the northern boundary. Otherwise, if it is heading southward, it continues southward. All of this is to say that the meridional direction of the current near the eastern slope is set by the phase of the zonal wave at that location. If southward displacement from the equator is considered a “trough” and northward displacement a “crest”, then the current ends up northward if the flow in the zonal wave moves from a trough to crest near the eastern slope. It moves southward if the flow is from a

crest to trough instead. In some rare cases, the crests or the troughs of the zonal wave coincide with the location of the maximum run-up point and the meridional velocity  $v$  there has values that are close to zero. This means that at that point the current did not particularly favour propagation into one or the other of the hemispheres. This situation corresponds to a splitting of the current in two parts following partial recirculation (e.g. see, Figure 5.6(b)).

From the range of simulations we find that varying some parameters ( $g'$ ,  $s$ ,  $\Omega$ ,  $l$  and  $R$ ) affects the zonal wave phase at the eastern slope and makes the current switch between the hemispheres, while the variability in other parameters ( $a$  and  $H$ ) has little effect on the final structure of the flow. In particular, increasing  $g'$ ,  $s$  and  $R$  increases the zonal wavelength, increasing  $\Omega$  decreases the zonal wavelength and increasing  $l$  allows more waves to fit along the zonal extent of the domain. In order to quantify how the zonal wavelength depends upon  $g'$ ,  $s$ ,  $\Omega$  and  $R$ , we examine an idealized “particle-model” for the motion of an equator-crossing fluid parcel.

Experiment	Physical parameter, $g' \times 10^{-4} \frac{m}{s^2}$	Inflow volume transport, $Q$ (Sv)	$T_s(\%)$
1	2	0.39	0
2	2.7	0.52	79
3	4	0.77	100
4	32	6.17	0

Table 5.1: Numerical simulations for various values of  $g'$ .

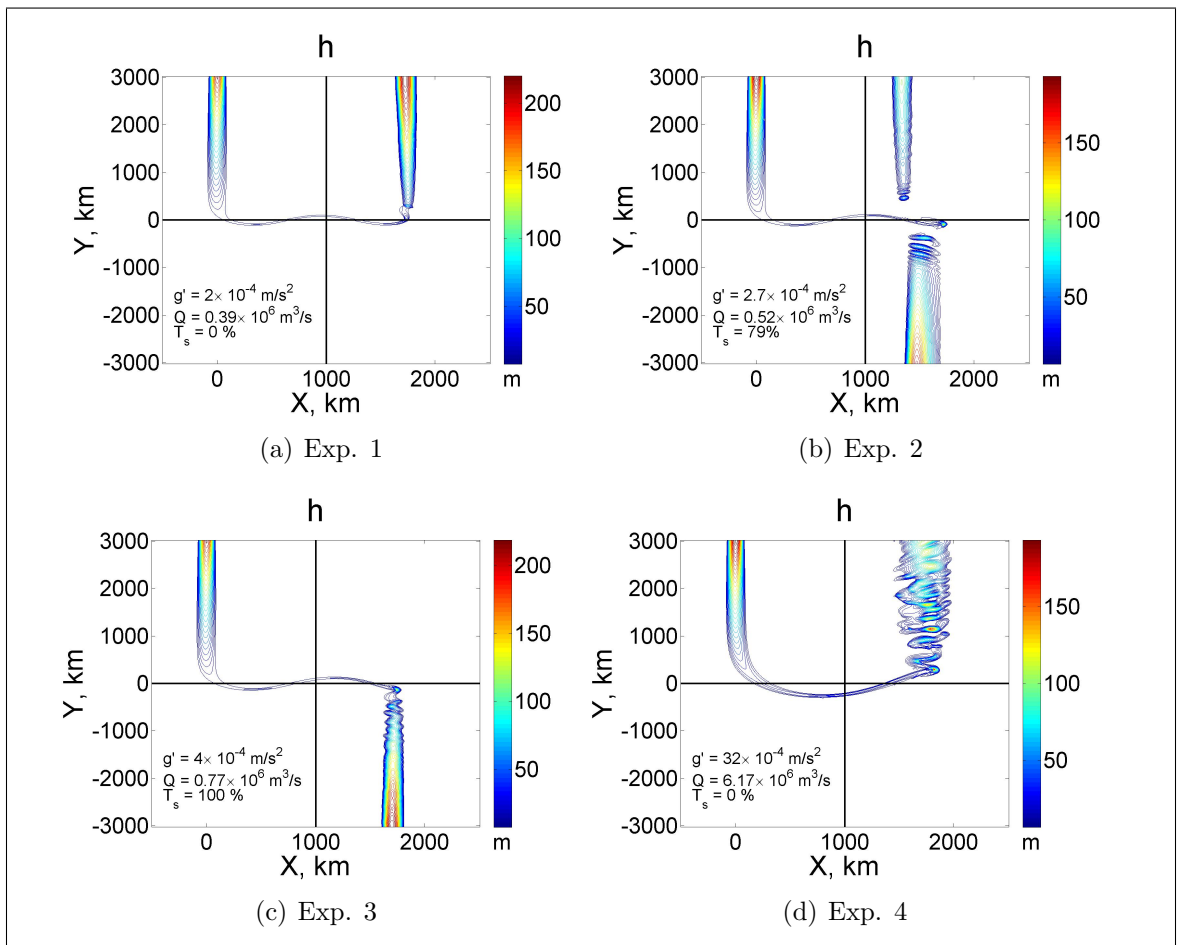


Figure 5.6: Contour plots of  $h$  for various values of  $g'$  (Table 5.1).

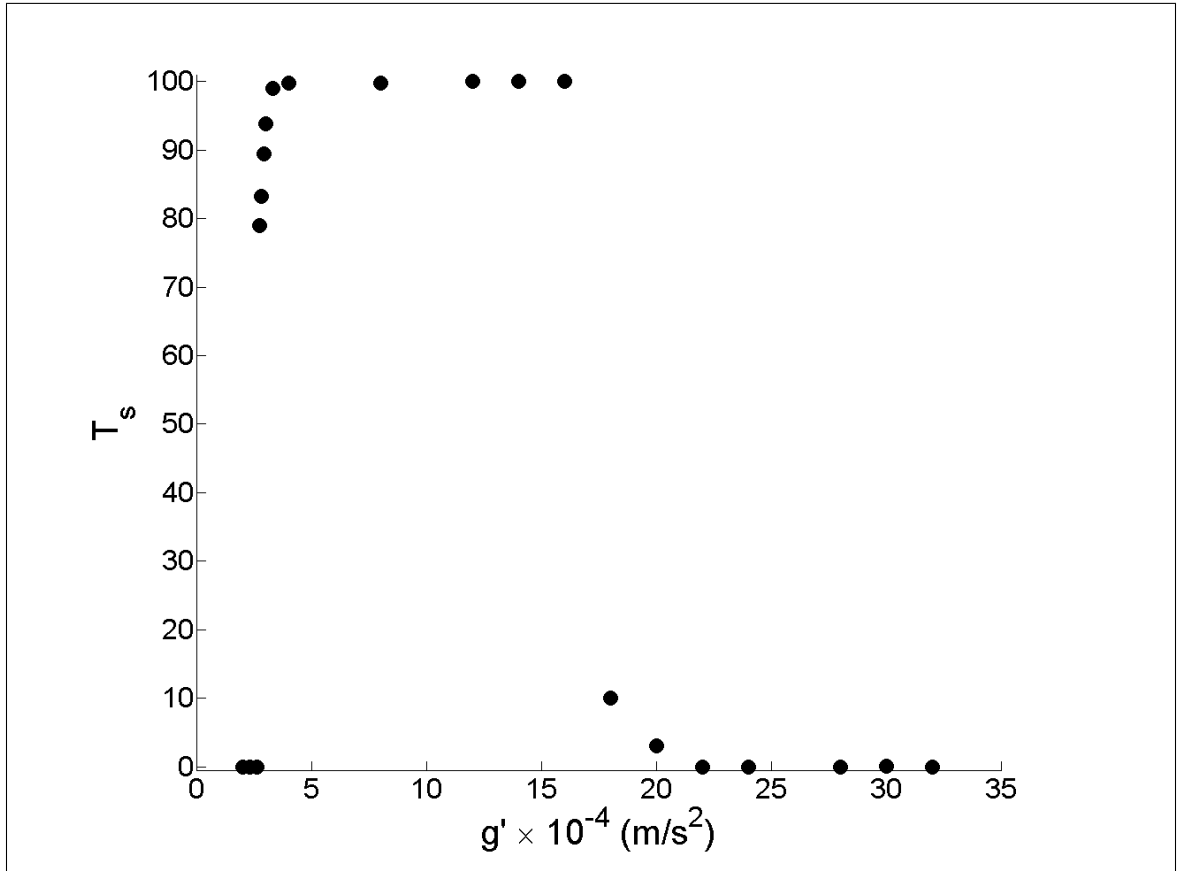


Figure 5.7: Southward transmission coefficients  $T_s$  vs.  $g'$ .

Experiment	Physical parameter, $s \times 10^{-3}$	Inflow volume transport, $Q$ (Sv)	$T_s$ (%)
5	1.5	0.39	0
6	2.3	0.58	65
7	9	2.31	100
8	16	4.11	0

Table 5.2: Numerical simulations for various values of  $s$ .

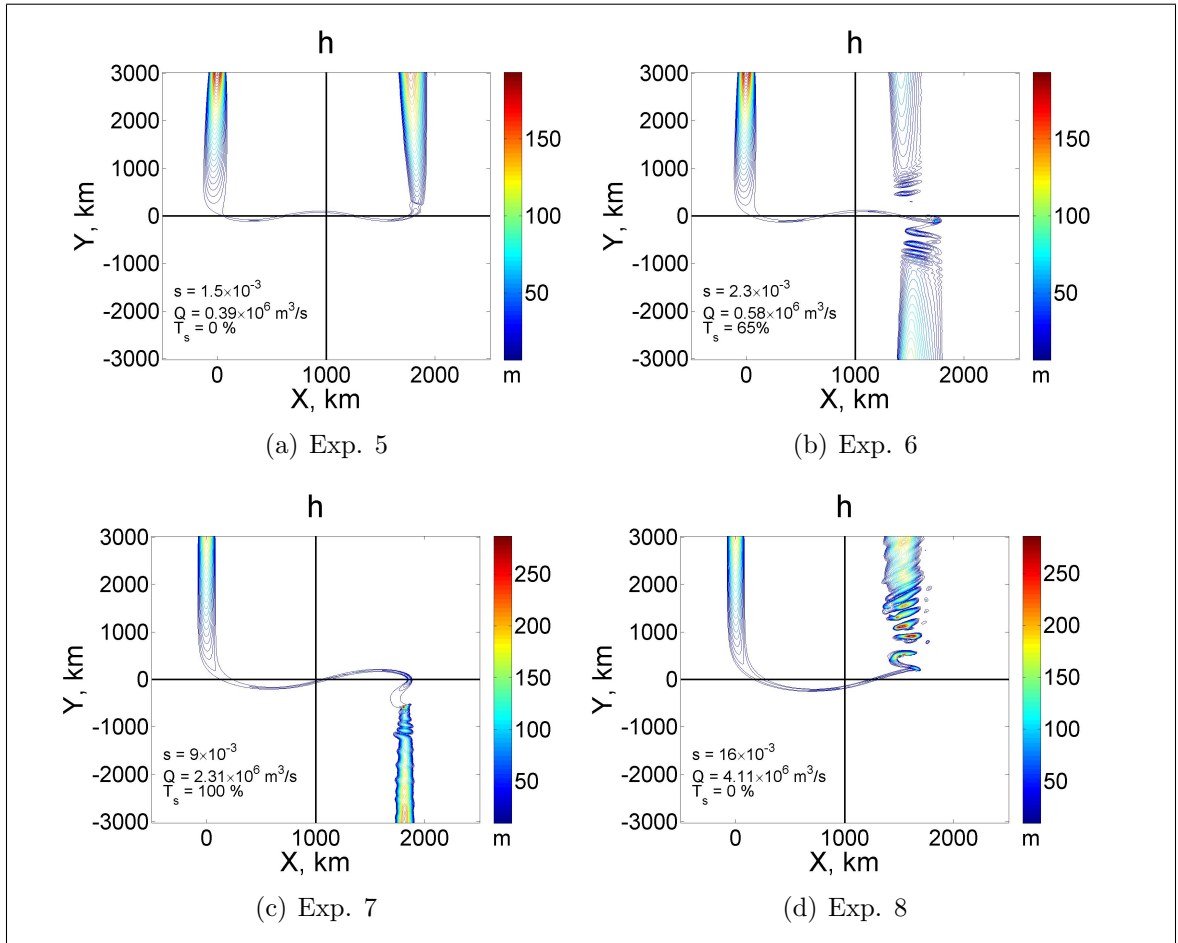


Figure 5.8: Contour plots of  $h$  for various values of  $s$  (Table 5.2).

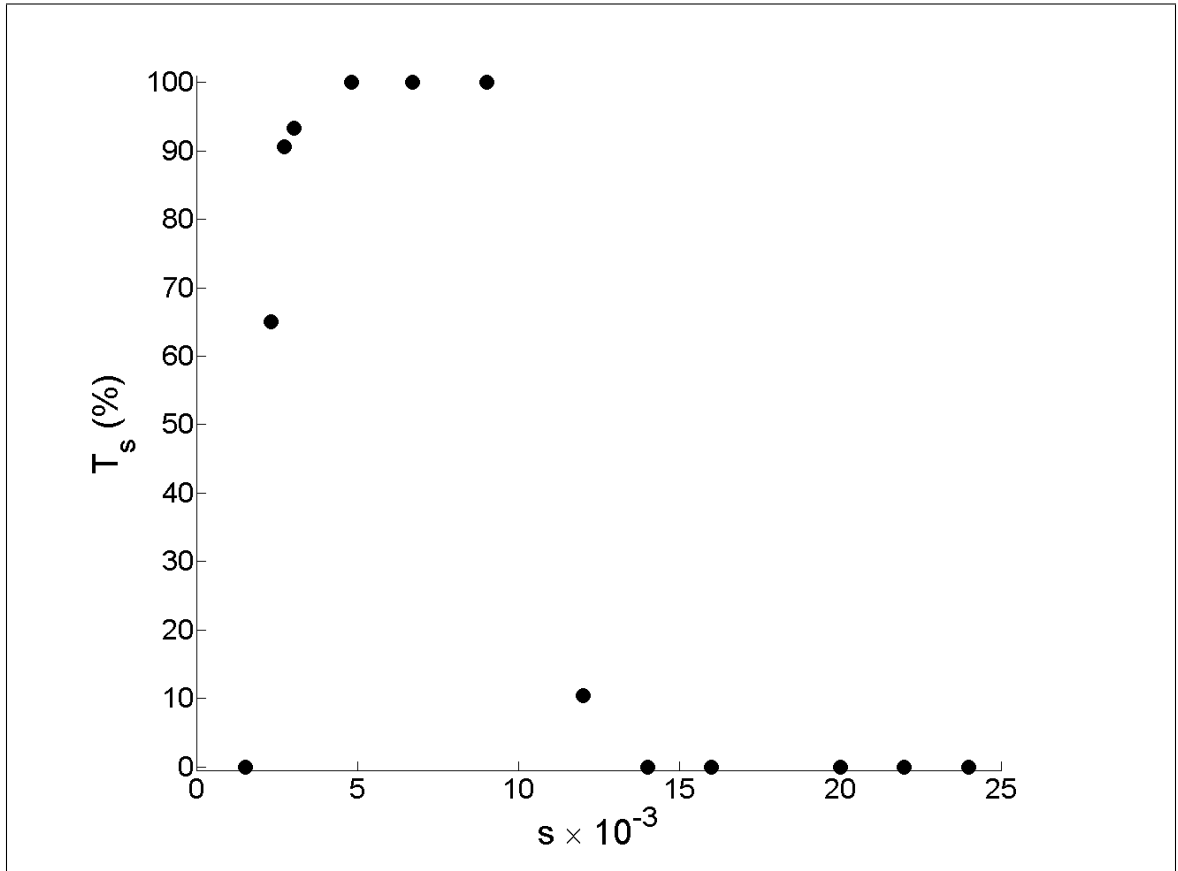


Figure 5.9: Southward transmission coefficients  $T_s$  vs.  $s$ .

Experiment	Physical parameter, $\Omega, 10^{-5} \frac{rad}{s}$	Inflow volume transport, $Q$ (Sv)	$T_s$ (%)
9	2.55	4.40	0
10	4.96	2.27	8.8
11	5.98	1.88	100
12	12.1	0.93	75

Table 5.3: Numerical simulations for various values of  $\Omega$ .

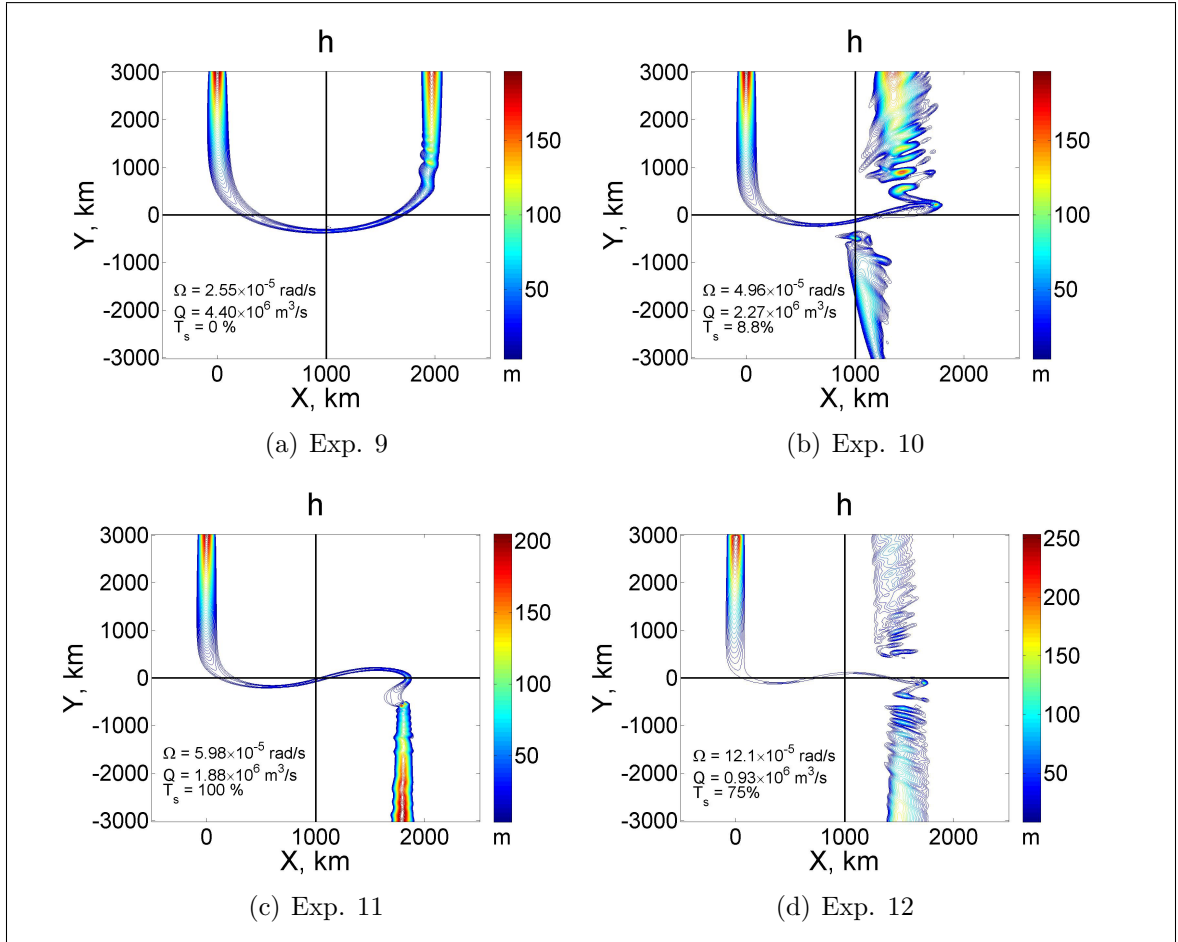


Figure 5.10: Contour plots of  $h$  for various values of  $\Omega$  (Table 5.3).

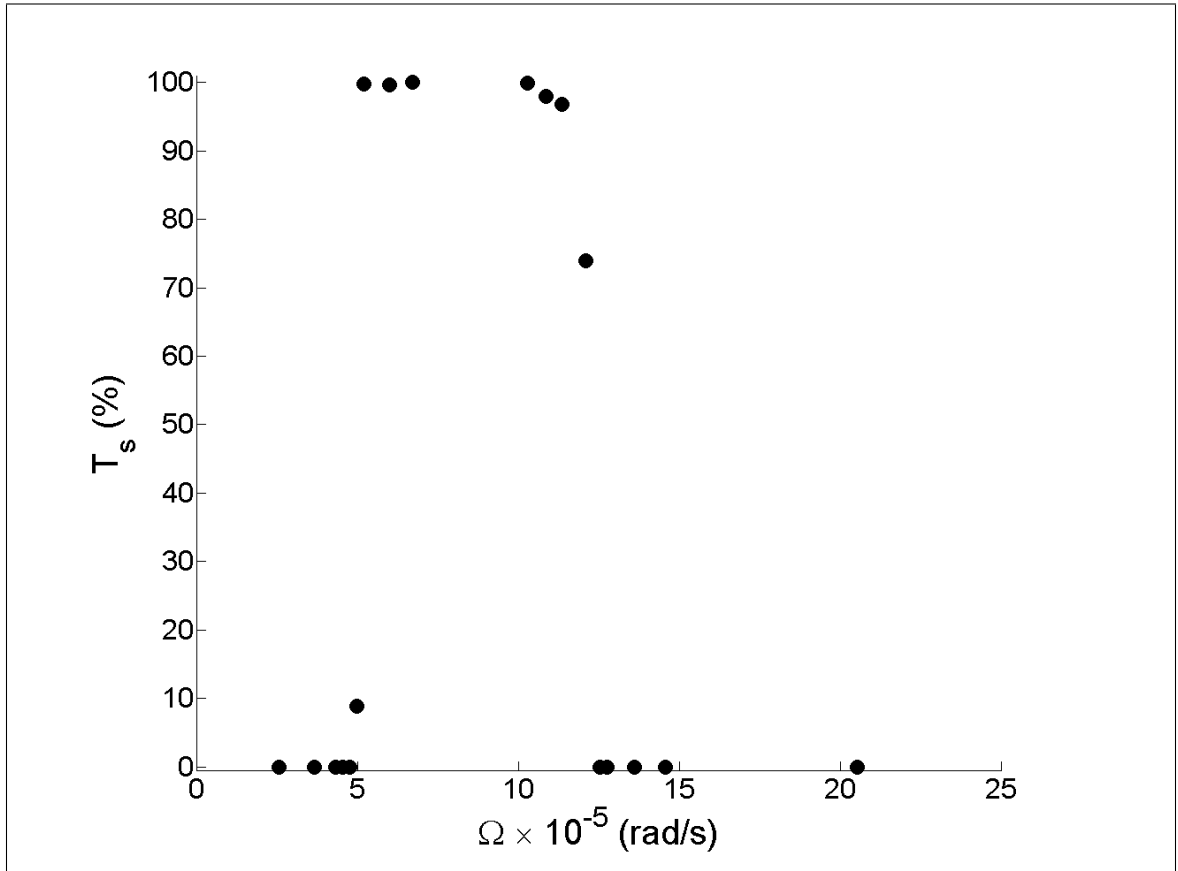


Figure 5.11: Southward transmission coefficients  $T_s$  vs.  $\Omega$ .

Experiment	Physical parameter, $l, km$	Inflow volume transport, $Q$ (Sv)	$T_s(\%)$
13	600	1.54	0
14	900	1.54	100
15	1200	1.54	100
16	1600	1.54	0

Table 5.4: Numerical simulations for various values of  $l$ .

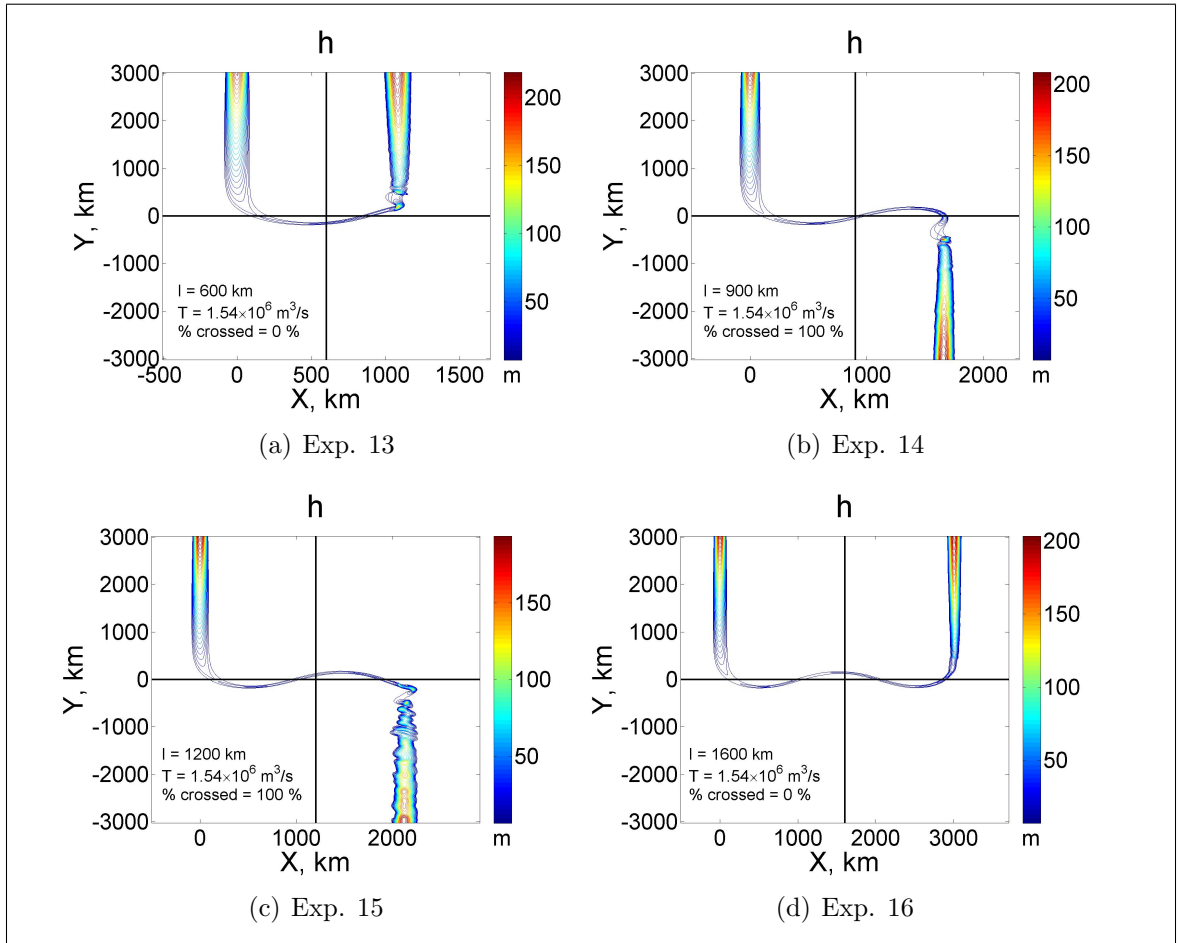
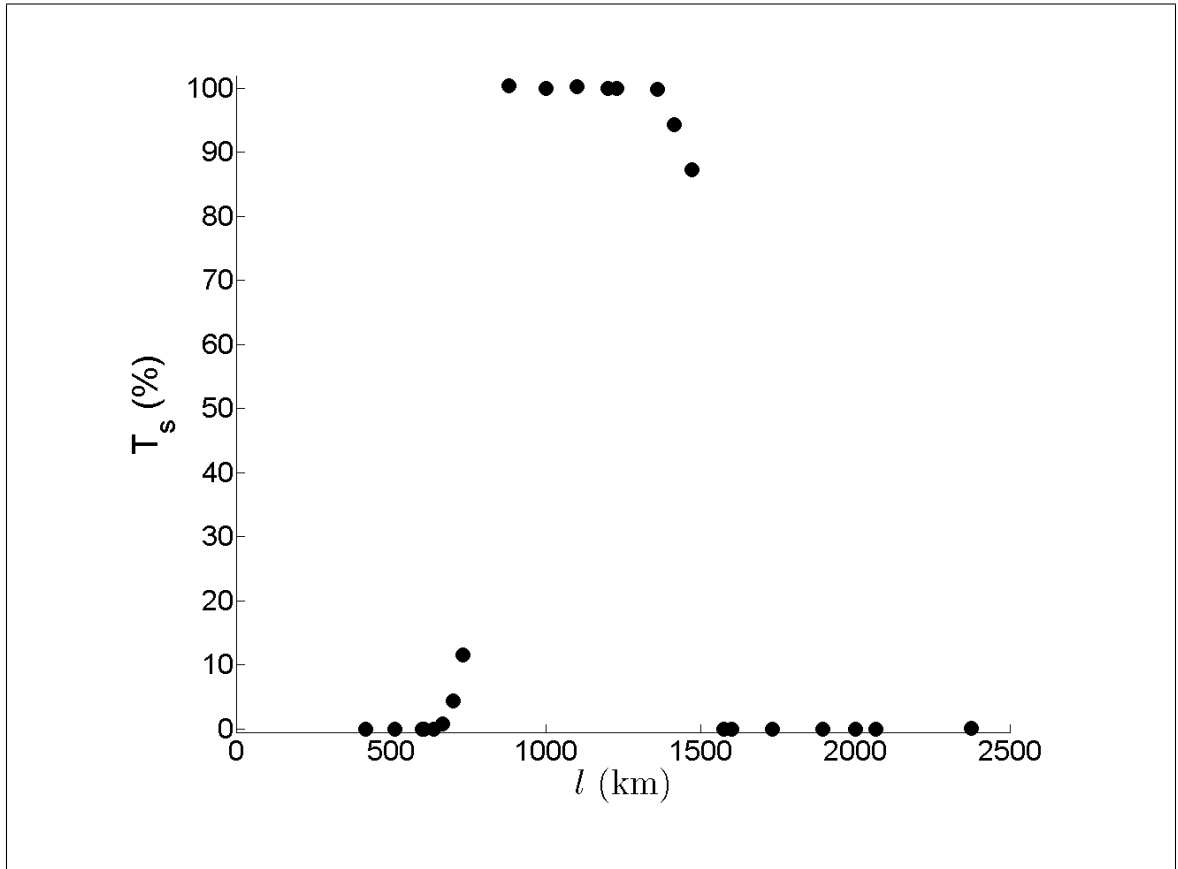


Figure 5.12: Contour plots of  $h$  for various values of  $l$  (Table 5.4).



**Figure 5.13:** Southward transmission coefficients  $T_s$  vs.  $l$ .

Experiment	Physical parameter, $R, km$	Inflow volume transport, $Q (Sv)$	$T_s(\%)$
17	3122	0.85	0
18	3823	0.99	66
19	5097	1.26	100
20	11468	2.70	0

Table 5.5: Numerical simulations for various values of  $R$ .

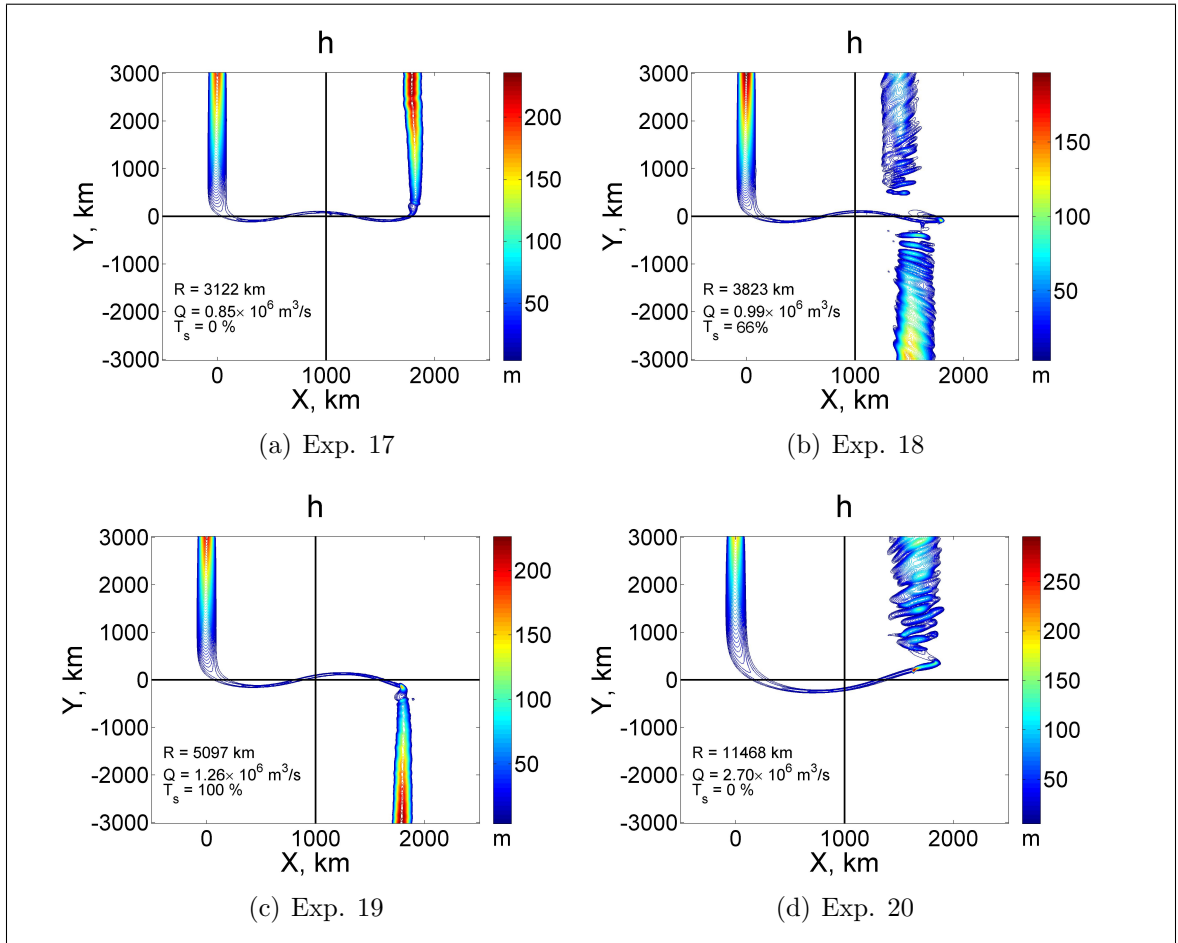


Figure 5.14: Contour plots of  $h$  for various values of  $R$  (Table 5.5).

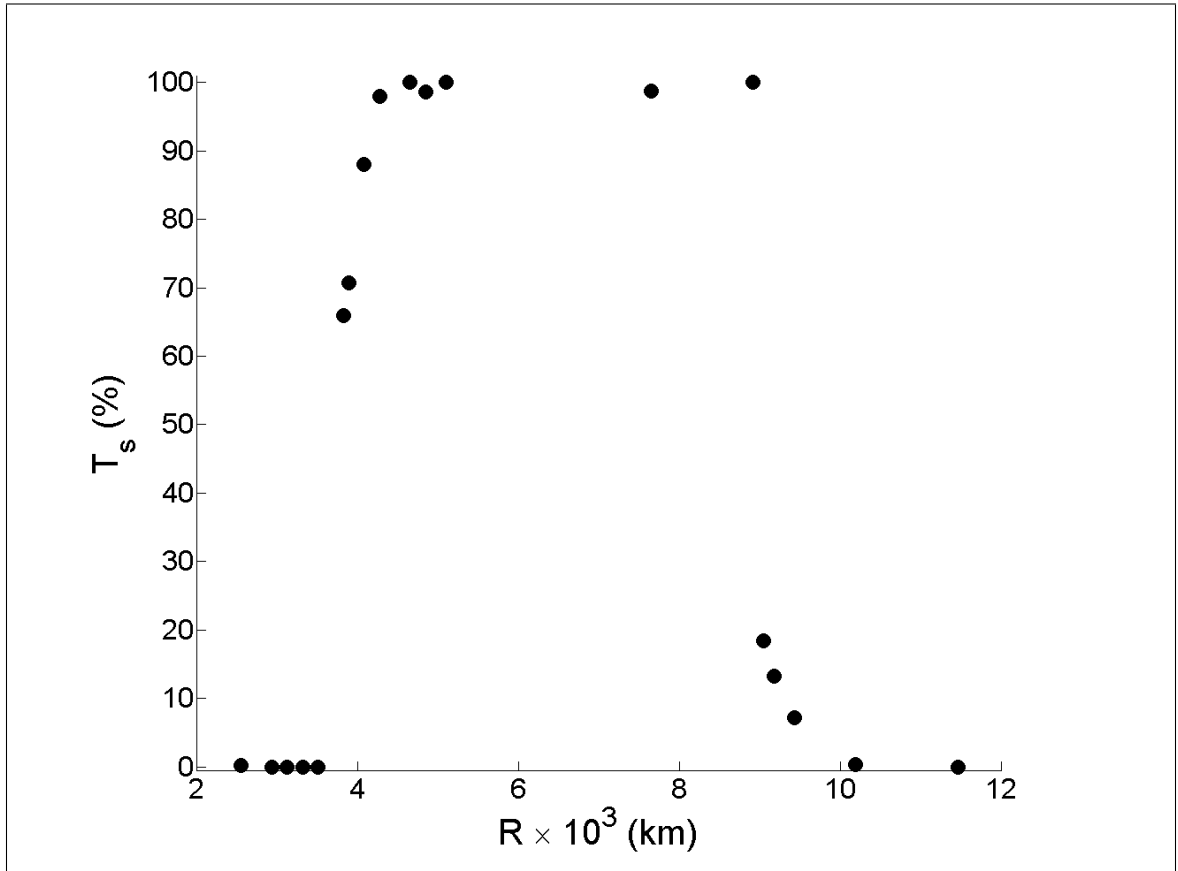


Figure 5.15: Southward transmission coefficients  $T_s$  vs.  $R$ .

Experiment	Physical parameter, $a, km$	Inflow volume transport, $Q$ (Sv)	$T_s(\%)$
21	20	0.38	100
22	53.3	1.03	100
23	160	3.08	100
24	320	6.16	100

Table 5.6: Numerical simulations for various values of  $a$ .

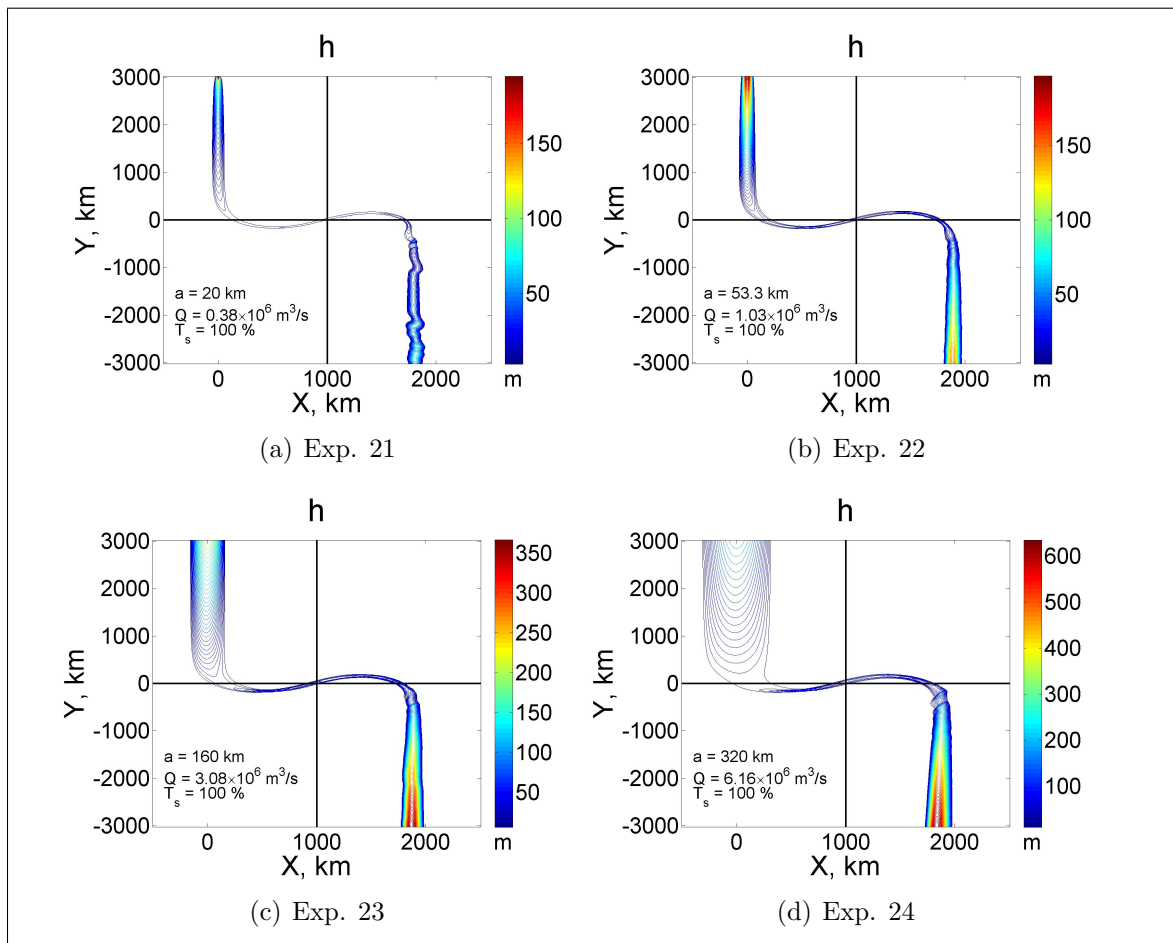


Figure 5.16: Contour plots of  $h$  for various values of  $a$  (Table 5.6).

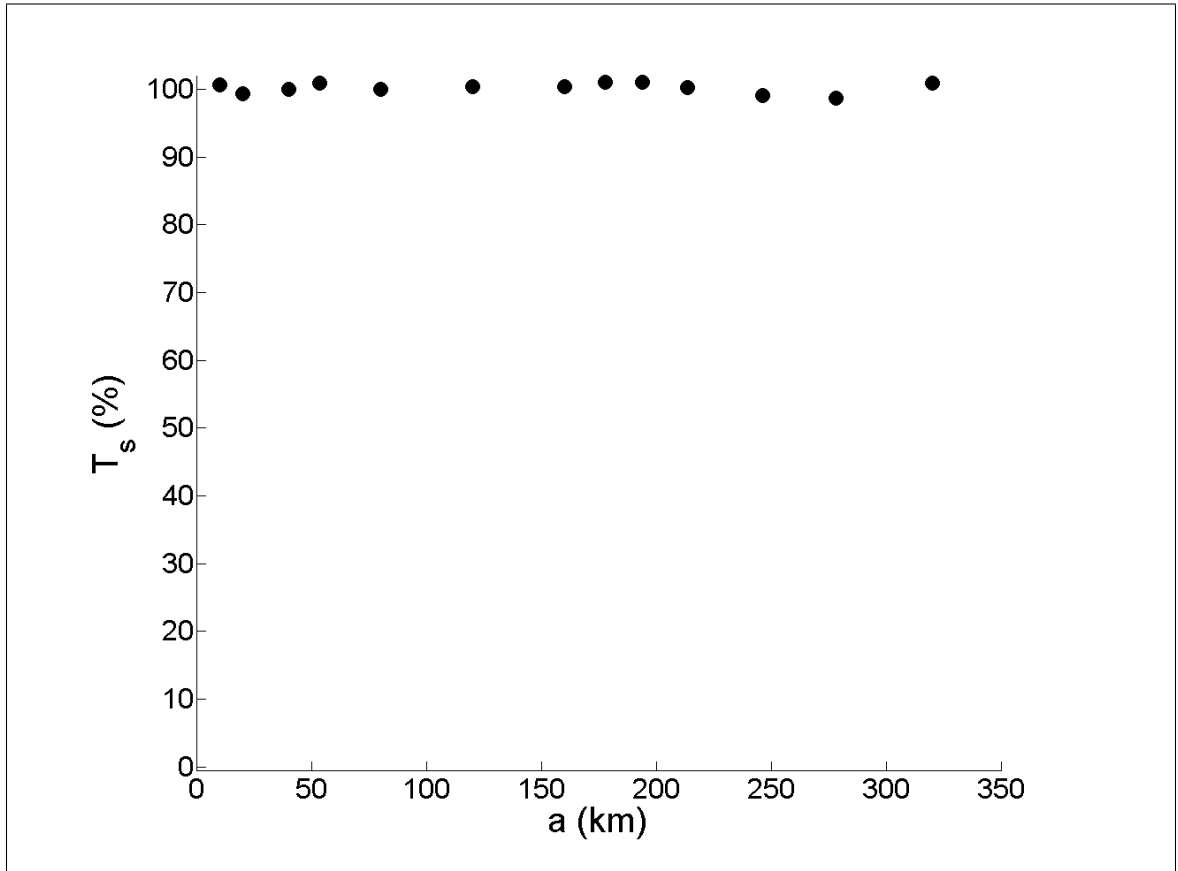


Figure 5.17: Southward transmission coefficients  $T_s$  vs.  $a$ .

Experiment	Physical parameter, $H, m$	Inflow volume transport, $Q$ (Sv)	$T_s(\%)$
25	50	0.39	100
26	95	0.73	100
27	400	3.08	100
28	600	4.62	100

Table 5.7: Numerical simulations for various values of  $H$ .

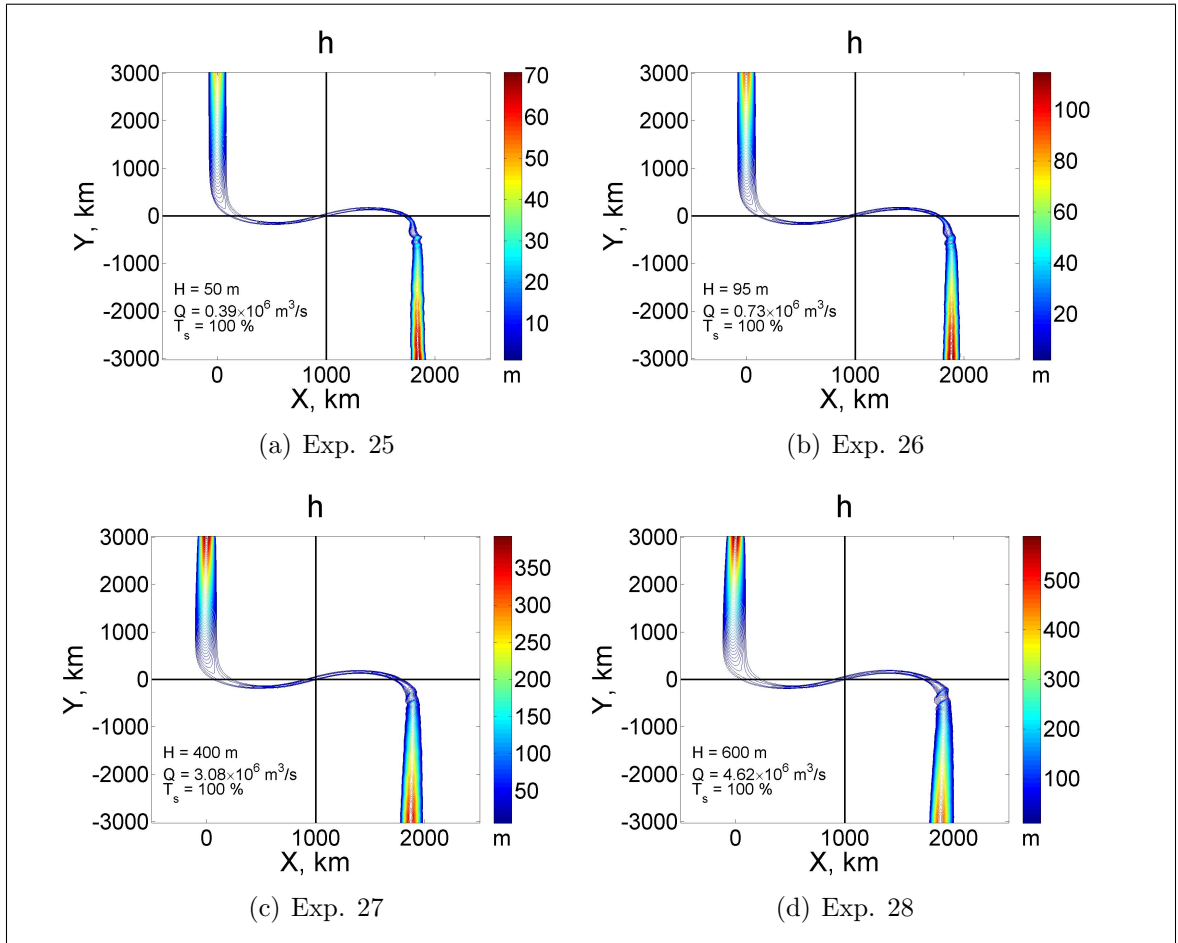


Figure 5.18: Contour plots of  $h$  for various values of  $H$  (Table 5.7).

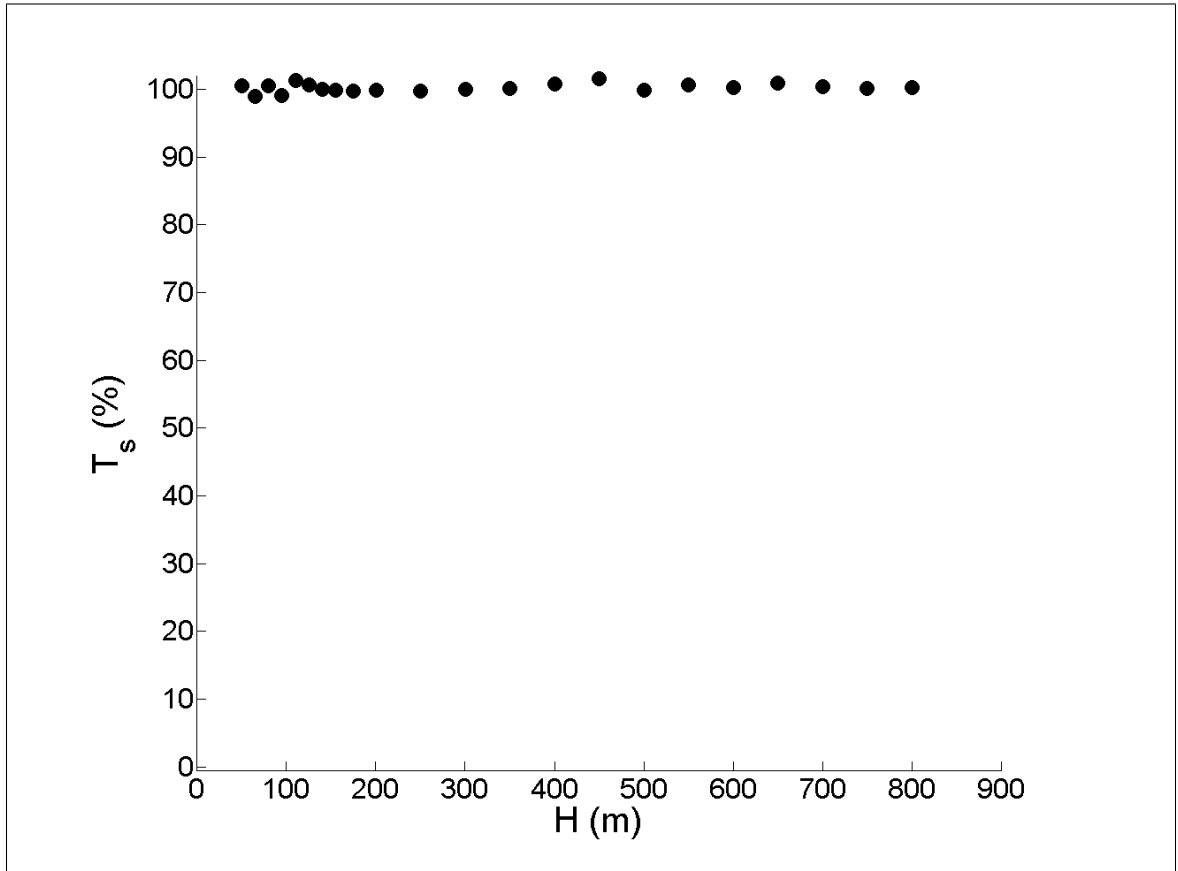


Figure 5.19: Southward transmission coefficients  $T_s$  vs.  $H$ .

## 5.2 Auxiliary Model of a Particle in a Rotating Channel

In this section we will study the motion of a particle in a rotating cross-equatorial channel. This simplified approach allows us to consider purely inertial motion as it is influenced by rotation and topography while neglecting other complicated effects such as pressure and viscosity.

The question of how the motion of a particle relates to the motion of a fluid parcel in mid-latitudes and in the equatorial region is of considerable interest in oceanography and meteorology, and has been extensively studied in the past (e.g. Paldor & Killworth, 1988; Ripa, 1997; Pennell & Seitter, 1990; Paldor & Sigalov, 2006; Dvorkin & Paldor, 1999; Cushman-Roisin, 1982).

The governing equations that describe this motion are given by four coupled ordinary differential equations:

$$\frac{du}{dt} = 2\Omega \sin(y/R) v - g'h'_b, \quad (5.2)$$

$$\frac{dv}{dt} = -2\Omega \sin(y/R) u, \quad (5.3)$$

$$\frac{dx}{dt} = u, \quad (5.4)$$

$$\frac{dy}{dt} = v. \quad (5.5)$$

Here  $h'_b(x)$  represents the zonal slope of the bottom topography .

We prescribe the initial state of a particle to be analogous to the initial conditions used for numerical simulations of the abyssal current. The particle is placed at  $x = 0$  km (the same as the center of the inflow current) and starts its motion from the same latitude  $y_0 = 3000$  km in the northern hemisphere with no eastward velocity  $u$ . The northward velocity  $v$ , on the other hand, is given by the Nof velocity (3.20).

Explicitly, the full set of the initial conditions is given by

$$x|_{t=0} = 0, \tag{5.6}$$

$$y|_{t=0} = y_0, \tag{5.7}$$

$$u|_{t=0} = 0, \tag{5.8}$$

$$v|_{t=0} = v_{\text{Nof}}. \tag{5.9}$$

Despite the seemingly simple structure of the governing equations (5.2)-(5.5), the particle model does not have an explicit analytic solution. To gain insight we solved this system numerically varying one physical parameter at a time as was done in the numerical simulations of the abyssal current.

For example, Figure 5.20 shows the trajectories of a particle computed by solving (5.2-5.5) with different values of the reduced gravity. As in the abyssal current simulations, the particle initially travels southward along a straight line parallel to the axis of the channel towards the equator. Upon entering the vicinity of the equator the particle turns eastward in the downslope direction and continues to propagate from west to east oscillating northward and southward about the equator. Eventually, the particle rises up on the eastern side of the channel. In some cases the particle, after it leaves the equatorial region, ends up in one of the hemispheres (Figures 5.20(a), 5.20(b), 5.20(d) and 5.20(f)). This behaviour is similar to that observed for the simulated abyssal current. Likewise we see that the zonal wavelength increases with increasing  $g'$  in these 4 cases. Unlike those simulations, the particle is sometimes observed to follow chaotic trajectories (Figures 5.20(c), 5.20(e)), switching back and forth between the western and eastern sides of the channel. In spite of this generally chaotic behaviour, each individual part of the trajectory is consistent with the trajectories determined for a particle moving along the flat bottom in the equatorial region (Ripa, 1997; Paldor & Sigalov, 2006; Cushman-Roisin, 1982; Paldor & Killworth, 1988).

Because our interest is mainly focused on the zonal wave in the vicinity of the equator, we derived a simplified version of the model equations (5.2) and (5.3) that revealed what combination of the physical parameters defines the wavelength of the

zonal wave. In order to simplify the equations we introduced the following approximations:

- equatorial  $\beta$ -plane approximation to the Coriolis parameter,
- in the equatorial region the particle travels along the flat bottom ( $h_{bx} = 0$ ),
- the eastward velocity  $u$  in the equatorial region is constant and proportional to the velocity set by the boundary conditions at  $y = y_0$ . That is  $u \sim v_{\text{Nof}}$  given by (3.20).

Making the above approximations reduces the system of the governing equations (5.2)-(5.5) to a single equation for the meridional position as a function of time:

$$\frac{d^2 y}{dt^2} + \beta u y = 0, \quad (5.10)$$

in which  $\beta = \frac{2\Omega}{R}$  is the equatorial value of the beta-plane. Equation 5.10 describes simple harmonic oscillations with angular frequency  $\omega$  and corresponding zonal wavelength  $\lambda = \frac{2\pi}{\omega} v_{\text{Nof}}$  given by

$$\omega_p = (\beta u)^{1/2} \sim \left( \frac{g' s}{y_0} \right)^{1/2}, \quad (5.11)$$

$$\lambda_p \sim 2\pi \left( \frac{v_{\text{Nof}}}{\beta} \right)^{1/2} = 2\pi L_{Rh}. \quad (5.12)$$

The scale

$$L_{Rh} \equiv \left( \frac{v_{\text{Nof}}}{\beta} \right)^{1/2} = \frac{1}{2} \left( \frac{g' s}{y_0} \right)^{1/2} \frac{R}{\Omega} \quad (5.13)$$

is called the Rhines scale (Rhines, 1975). It is most commonly used to predict the meridional spacing of the zonal jets in the atmospheres of giant planets or the scales of the boundary currents in the Earth's oceans that depend upon  $\beta$  and turbulence velocity scales (Galperin *et al.*, 2004; Richards *et al.*, 2006). More generally, the Rhines scale is the length scale derived from a characteristic velocity scale and  $\beta$ . It describes the balance between non-linear advection of the relative vorticity and linear advection of the planetary vorticity (Olbers *et al.*, 2012; Pinardi & Woods, 2002).

Figure 5.21 compares the prediction (5.12) to the zonal wavelength measured in numerical solutions of the particle model (5.2-5.5). This wavelength was determined as twice the distance between the first zonal wave crest and trough. The figure shows an excellent collapse of data for simulations with widely varying parameters  $s$ ,  $\Omega$ ,  $R$  and  $g'$ . Thus, in spite of the equatorial  $\beta$ -plane and flat-bottom approximations, we were able to capture the essential dynamics governing the cross-equatorial oscillations of a particle. For sufficiently large  $L_{Rh}$  we find

$$\lambda = 10.2L_{Rh} + \lambda_0, \text{ with } \lambda_0 = 933 \text{ km.} \quad (5.14)$$

Furthermore, consistent with the abyssal current simulations, we find that the zonal wavelength increases with increasing  $g'$ ,  $s$  and  $R$  and decreases with  $\Omega$ . In the following section we use these results to interpret the abyssal current simulations.

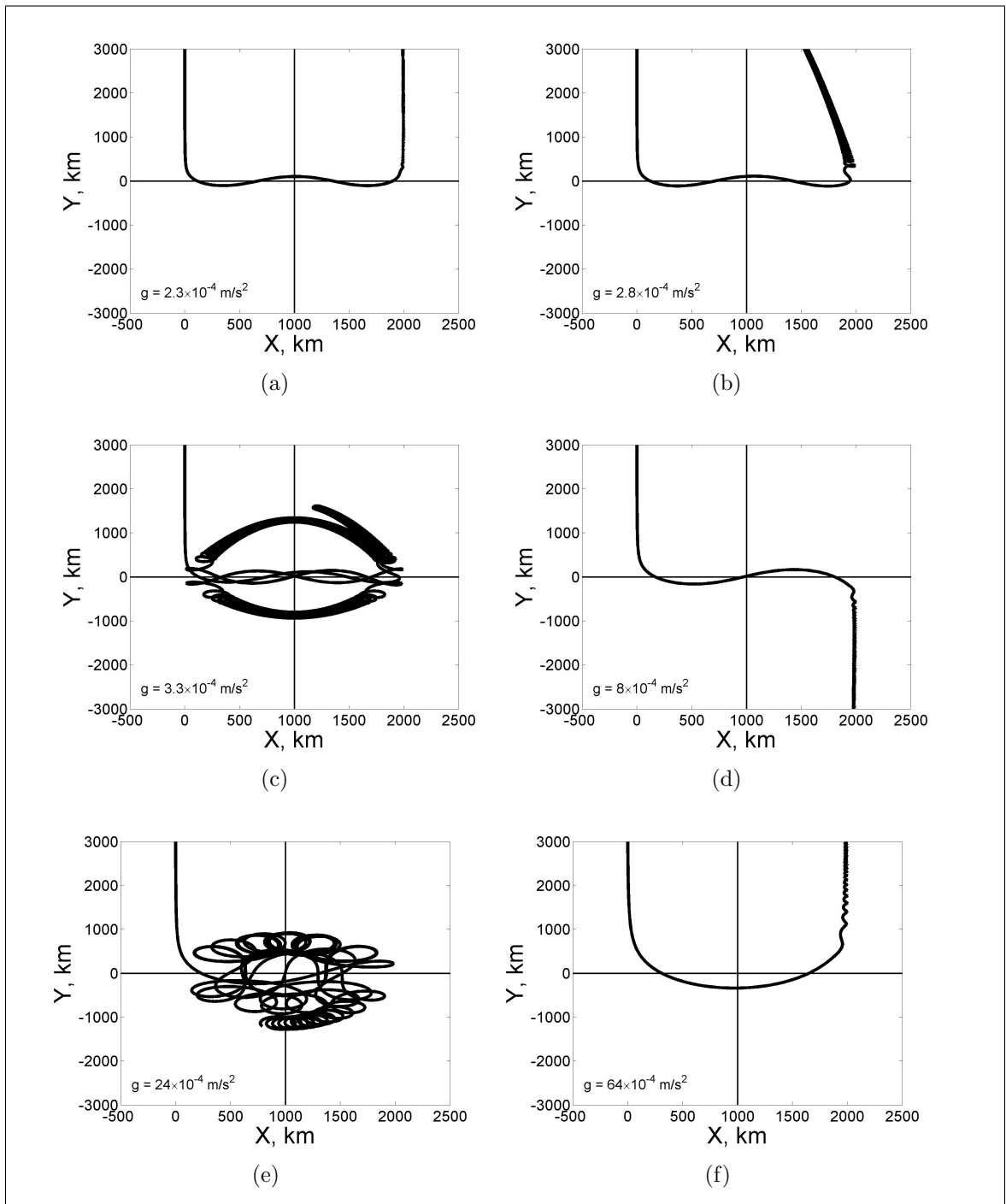


**Figure 5.20:** Trajectories of a particle in a rotating cross-equatorial channel for various value of  $g'$ .

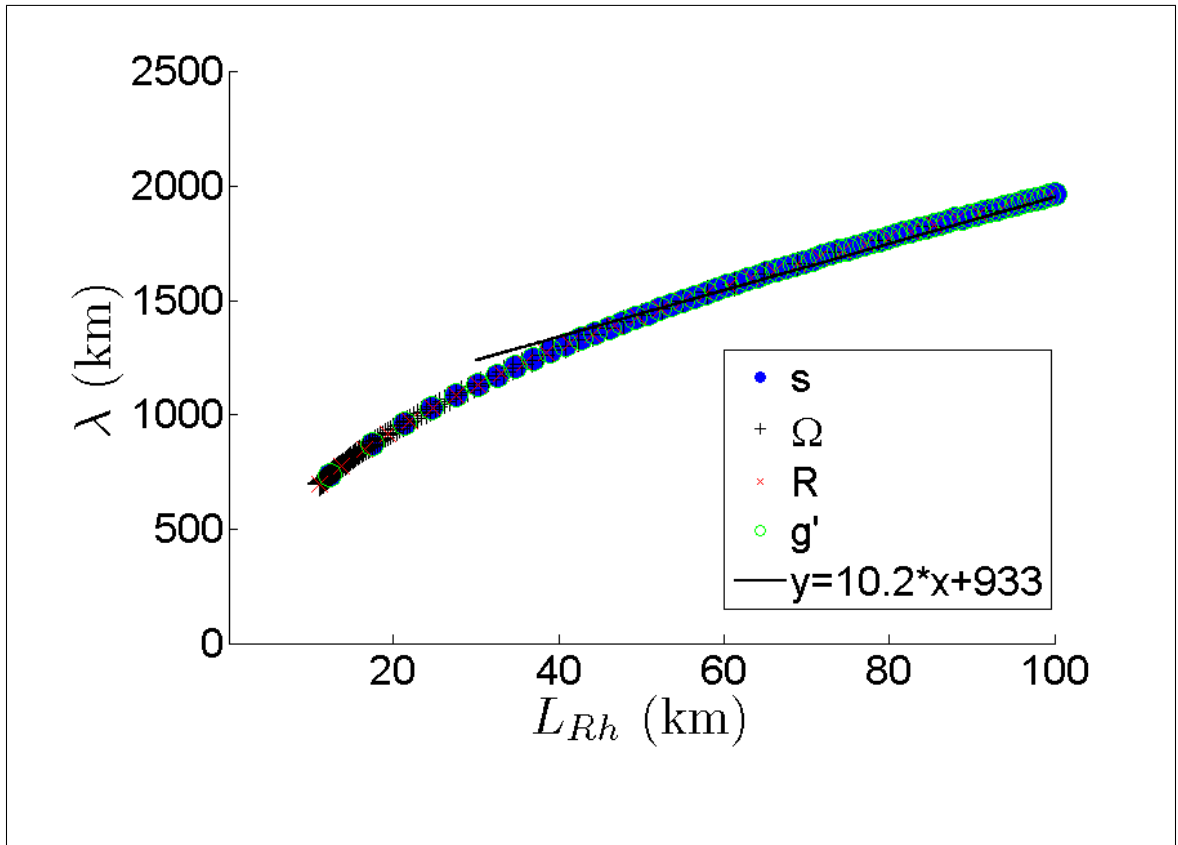


**Figure 5.21:** Particle model. Wavelength  $\lambda$  of the zonal wave in the equatorial area vs. the Rhines scale  $L_{Rh}$  given by (5.13).

### 5.3 Comparison of Two Models

In the previous section we showed that a strictly inertial model of a particle in the rotating channel is able to capture many important features of the motion of the cross-equatorial abyssal currents, thus indicating that the inertial forces play the dominant role in the dynamics of the abyssal currents. Analogous to (5.12) we anticipate the zonal wavelength in the abyssal current simulations should depend upon the Rhines scale. Indeed, Figure 5.22 shows that the measured wavelength of the zonal wave formed by the current in the equatorial region is well predicted by  $L_{Rh}$ .

Similar to Figure 5.21, all points in Figure 5.22 show an almost linear increase of the wavelength with  $L_{Rh}$ . The best-fit line through these data points gives

$$\lambda = 18.5L_{Rh} + \lambda_0, \text{ with } \lambda_0 = 779 \text{ km.} \quad (5.15)$$

This prediction indicates that in the numerical simulations of the abyssal current the wavelength grows faster with  $L_{Rh}$  than that predicted by the particle model in (5.14). That is to be expected because we introduced several crude approximations to the particle model in order to make it solvable analytically.

In section 5.1 we argued that the position of the maximum run-up point relative to the crest and troughs of the zonal wave (i.e., the ratio between the zonal wavelength  $\lambda$  and the width of the topography  $2l$ ) is ultimately responsible for determining the hemisphere into which the current will flow. Our hypothesis is strongly supported by Figure 5.23 that shows the percentage of the fluid that flows southward depends on the phase of the wave expressed by the ratio  $\frac{\lambda}{2l}$  (top axis) and  $\frac{L_{Rh}}{2l}$  (bottom axis). The combination of values of  $T_s$  determined from all numerical simulations collapse to form a well defined step-like curve. The fact that the initial half-width and maximum height ( $a$  and  $H$ ) of the current are not present in the Rhines scale indicates that the zonal wavelength and, consequently, the percentage of the fluid that crossed the equator southward are also independent of  $a$  and  $H$ , consistent with our simulations (Figures 5.17 and 5.19).

For relatively small and large values of  $\frac{\lambda}{2l}$  the current experiences full recirculation to the northern hemisphere. These values correspond to the situations when the zonal

channel width contains between 0 to  $\approx \frac{1}{2}$  or  $\approx 1$  to  $\approx \frac{3}{2}$  wavelengths, respectively. In these cases the eastern run-up point occurs after a trough of the zonal wave but before its crest (e.g., Figures 5.6(a) and 5.6(d)). However, if the channel contains between  $\approx \frac{1}{2}$  to  $\approx 1$  wavelength, the run-up point occurs after a crest and before a trough, and the entire current ends up in the southern hemisphere. Two narrow transitional regions correspond situations when the current splits in two parts:  $\frac{\lambda_1}{2l} \approx 0.68$  and  $\frac{\lambda_2}{2l} \approx 1.13$ .

Considering the fact that we based our analysis on (5.12) derived from the simplified particle model, we observed a surprisingly good agreement in the location of the transitional regions between the different sets of the numerical simulations. Generalizing these results using (5.15), we predict southward recirculation if

$$\frac{(0.68)(2l) - \lambda_0}{18.5} < L_{Rh} < \frac{(1.13)(2l) - \lambda_0}{18.5}, \quad (5.16)$$

and northward otherwise.

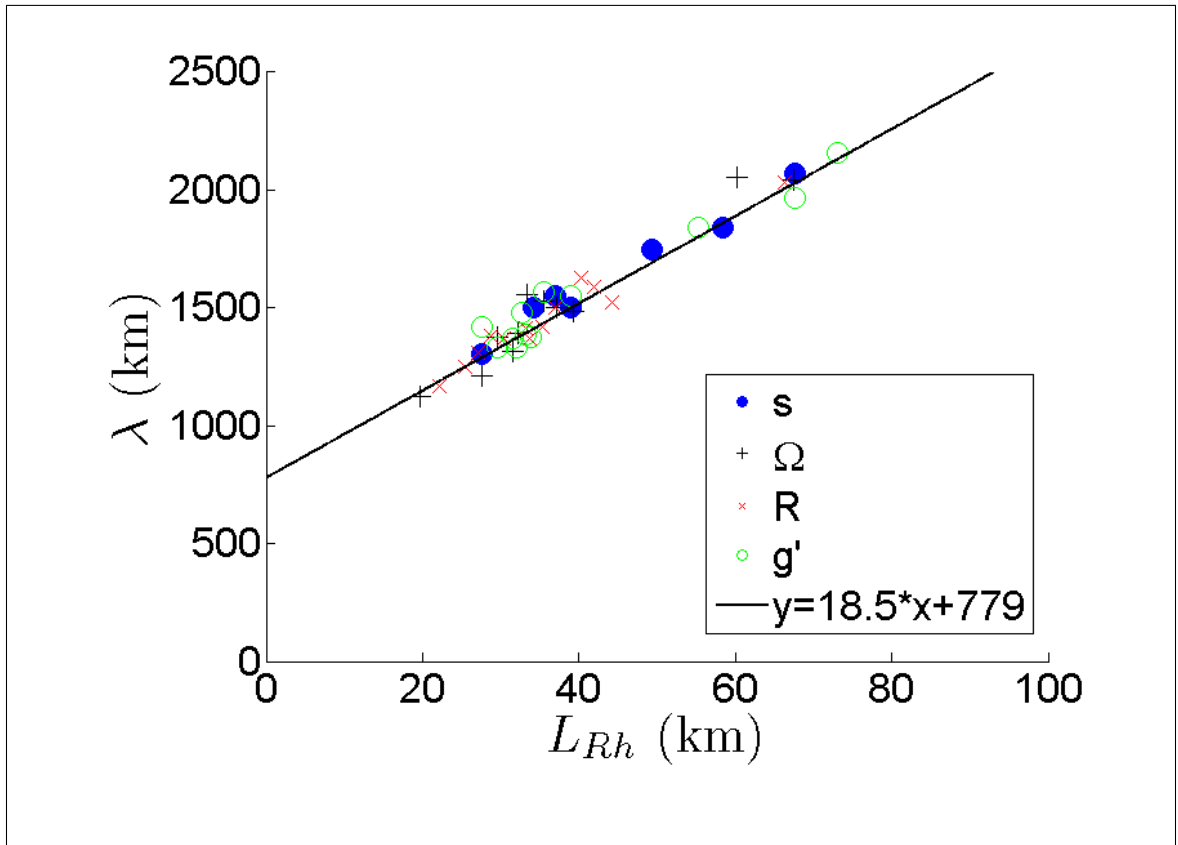


**Figure 5.22:** Numerical simulations. Wavelength  $\lambda$  of the zonal wave in the equatorial area vs. the Rhines scale  $L_{Rh}$  given by (5.13).

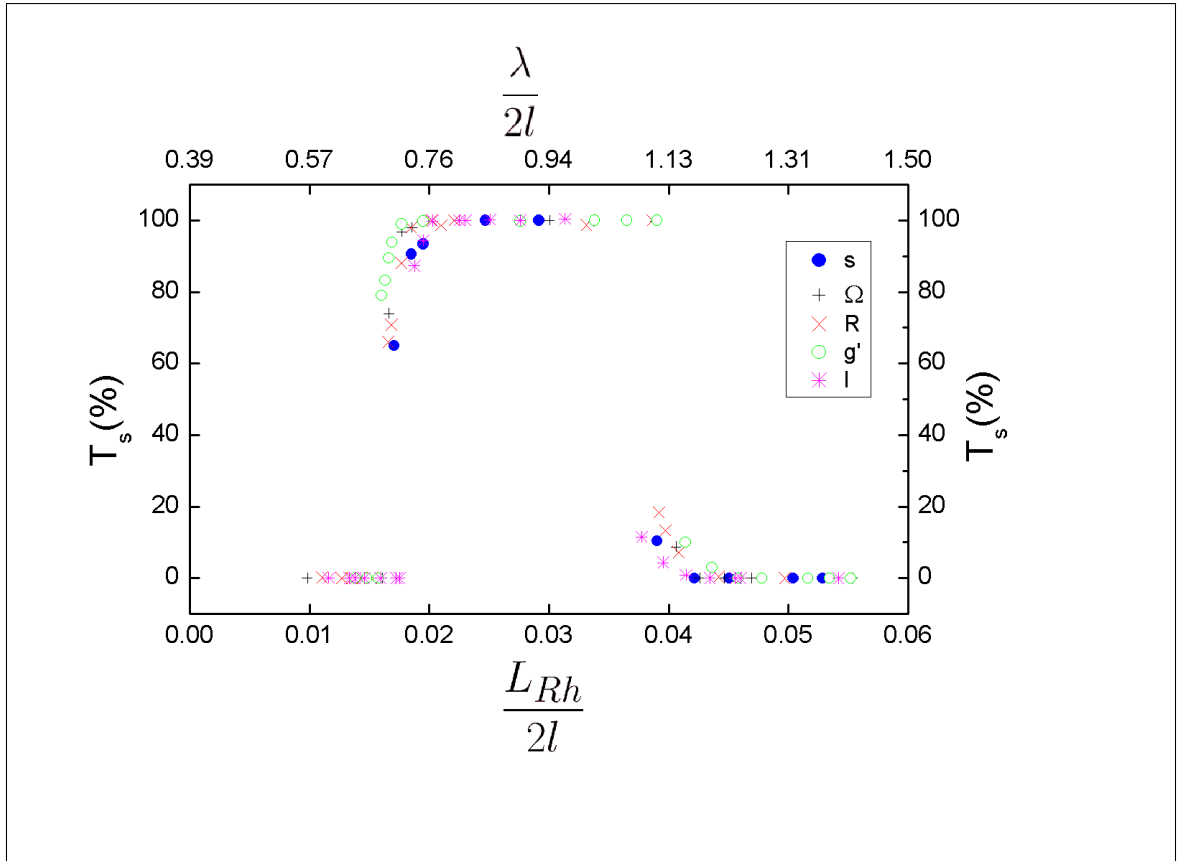


**Figure 5.23:** Southward transmission coefficients  $T_s$  vs.  $\frac{\lambda}{2l}$  (top axis) and  $\frac{L_{Rh}}{2l}$  (bottom axis).

# Chapter 6

## Conclusions

### 6.1 Summary

The main goal of this research was to study the behaviour of the cross-equatorial currents over idealized topography. Our analysis was based on numerical methods using the reduced-gravity shallow water model derived from the primitive incompressible Navier-Stokes equations. Several approximations were made, including approximating the ocean by two layers, where the top layer was assumed to be indefinitely deep and motionless and bottom layer represented the abyssal current. Each layer was assumed to have constant density. The pressure field was approximated as hydrostatic and the fluid was approximated as shallow. We also made the traditional approximation of a rapidly-rotating Earth by neglecting the components of the rotation vector that are not in the direction of the local vertical.

We then introduced the numerical procedure used in our numerical simulations. The domain discretization was based on the highly effective finite volume method (FVM) using a staggered Arakawa C-grid arrangement. FVM formulation of the flux-corrected transport (FCT) method was used to solve the reduced gravity shallow water equations in their conservation form. We also derived the initial/boundary conditions by applying geostrophic approximation to our model equations and introduced the default set of physical parameters used in our simulations.

The developed numerical procedure was tested in order to verify its validity. First, using an  $f$ -plane approximation, the analytical steady solution to the model equations

was found. The solution represented the  $y$ -independent parabolically shaped current centred at  $x = 0$  km, i.e., every meridional cross-section of the current was identical to that set by the boundary conditions at the northern boundary. Next we obtained the same solution using numerical techniques. By comparing the two solutions, we concluded that the error associated with the numerical solution grows rapidly as we move away from smooth parts of the solution closer to the areas of sharp gradients, but the overall discrepancy between the analytical and numerical solutions was found to be insignificant. Secondly, we compared the result of our numerical simulations with variable Coriolis force to the analytical solution of the planetary geostrophic model presented by (Swaters, 2013). The latter solution possesses several important properties. The groundings of the planetary geostrophic current can not vary with latitude and are therefore set by the northern boundary conditions. The thickness of the geostrophic current experiences almost linear decrease with latitude, while the meridional transport is independent of latitude. We concluded that in mid-latitude region our numerically simulated current shared all of the above-mentioned properties. On the contrary, in the immediate vicinity of the equator the numerically obtained solution showed significantly different behaviour than that of the planetary geostrophic current. Most notably, the simulated current experiences eastward turning and downhill acceleration when it enters the equatorial region, while the geostrophic current keeps moving along the slope and diminishes in height when it approaches the equator.

In the numerical simulation with the default initialization parameters it was observed that during the first stage of its motion the current was propagating equatorward with little change in the location of its groundings, while accelerating equatorward and decreasing in height. Interaction with the equator forced the fluid to form a narrow current with further downhill acceleration and the eastward propagation. In the case with default parameters the entire current ended up in the south hemisphere after it reached the maximum run-up point on the eastern side of the topography.

To explore what sets the meridional direction of the current on the eastern boundary we performed several numerical simulations with wide-ranging parameters gov-

erning the initial/boundary conditions and topographic extent. Each set of numerical simulations was obtained by changing only one physical parameter at a time. The simulations clearly showed that the abyssal current can either cross the equator and end up in the southern hemisphere or recirculate back to the northern hemisphere. In some rare cases the current partially penetrates into the southern hemisphere with the remainder returning back to the northern hemisphere. We examined the change in the southward transmission coefficient  $T_s$  with physical parameters  $g'$ ,  $s$ ,  $\Omega$ ,  $R$  and  $l$ . The plots versus each parameter formed step-like curves, where  $T_s \approx 1$  for some range of values and  $T_s \approx 0$  for values outside that range. Changing the incident current width and height,  $a$  and  $H$ , did not have any effect on  $T_s$ .

We determined that the position of the maximum run-up point relative to the crest and troughs of the zonal wave in the equatorial region is ultimately responsible for determining into which hemisphere the current will flow. In order to find an appropriate combination of the physical parameters that fully describes the behaviour of the abyssal current, we turned to a model of a particle in a rotating cross-equatorial channel. It was determined that, in spite of the simplicity of this model, it is able capture the essential dynamics of the cross-equatorial abyssal currents.

Further analysis of that model showed that the zonal wavelength of the along-equatorward flow can be represented by the Rhine scale  $L_{Rh} = \sqrt{\frac{v_{Nof}}{\beta}} = \frac{1}{2} \left(\frac{g's}{y_0}\right)^{1/2} \frac{R}{\Omega}$ . Explicitly, in the particle model the wavelength of the equatorial zonal wave was found to depend linearly upon  $L_{Rh}$  as  $\lambda \approx 10.2L_{Rh} + \lambda_0$ , with  $\lambda_0 = 933$  km. Likewise, a linear dependence of zonal wavelength upon  $L_{Rh}$  was found by analysis of fully nonlinear simulations, i.e.,  $\lambda \approx 18.5L_{Rh} + \lambda_0$ , with  $\lambda_0 = 779$  km. We conclude that values of  $T_s$  are set by the number of wavelengths that can fit into the zonal extent of the topography (i.e., the ratio between the zonal wavelength  $\lambda$  and the width of the topography  $2l$ ). The series of values of  $T_s$  determined from all numerical simulations plotted against  $\frac{\lambda}{2l}$  collapsed to form a well defined step-like curve proving that the motion of equator-crossing abyssal ocean currents is driven by inertia. The transitional regions of this top-hat curve are located at  $\frac{\lambda_1}{2l} \approx 0.68$  and  $\frac{\lambda_2}{2l} \approx 1.13$ . These correspond to partial penetration of the current into the southern and northern

hemispheres. The extent of the transitional regions was found to be much narrower than those described by Nof & Borisov (1998).

Although there is considerable variability and uncertainty, oceanographically observed estimates for the order of magnitudes for the parameters of deep currents in the Atlantic at  $26.5^\circ$  N ( $y_0 \approx 2900$  km) (e.g. see, Baehr *et al.*, 2009; Meinen *et al.*, 2012; Peña-Molino *et al.*, 2012) are about  $g' \approx 0.002$  m/s<sup>2</sup> and  $s \approx 0.008$ . Taking the radius and rotation of the Earth to be  $R \approx 6371$  km and  $\Omega \approx 7.3 \times 10^{-5}$  rad/s, respectively, and estimating  $2l = 2500$  km to be the zonal extent of equatorial Atlantic, we calculate that  $\frac{L_{Rh}}{2l} \approx 0.04$ . Hence, the relative zonal wavelength is  $\frac{\lambda}{2l} \approx 1.06$ . Considering these values our models predicts (see Figure 5.23) full penetrations of the abyssal current into the southern hemisphere. However, in this case the current's state is described by the point located near the transition at  $\frac{\lambda_2}{2l}$ , which means that even slight increase in  $\frac{\lambda}{2l}$ , for example through shortening of the zonal extent  $l$  by the influence of the Mid-Atlantic Ridge, might dramatically change the pathway of the abyssal current.

## 6.2 Future Directions

This research has offered and explained one of the possible mechanisms of the observed recirculation of North Atlantic Deep Water as it approaches the equator (McCartney, 1993; McCartney & Curry, 1993; Schmid *et al.*, 2005; Sarafanov *et al.*, 2007).

The model presented in this thesis uses a highly idealized topography and shape of the abyssal current. We hope that future numerical simulations will take into account some important phenomena that take place in real ocean, but are omitted in our model.

In order to improve this model one might consider the analysis of multi-layered or continuously stratified models with the implementation of some important features such as a more realistic topography, mixing and turbulent effects, etc. For example, it is argued that taking into account the horizontal component of the Earth's rotation vector will increase the cross-equatorial transport by 10-30 % (Stewart & Dellar,

2012). Including all of the above-mentioned processes in a numerical model might reveal alternative recirculation mechanisms in the abyss of the world ocean.

# Bibliography

- AMANTE, C. & EAKINS, B. W. 2009 *ETOPO1 1 arc-minute global relief model: procedures, data sources and analysis*. US Department of Commerce, National Oceanic and Atmospheric Administration, National Environmental Satellite, Data, and Information Service, National Geophysical Data Center, Marine Geology and Geophysics Division.
- ARAKAWA, A. & HSU, Y.-J. G. 1990 Energy conserving and potential-enstrophy dissipating schemes for the shallow water equations. *Monthly Weather Review* **118** (10), 1960–1969.
- ARAKAWA, A. & LAMB, V. R. 1977 Computational design of the basic dynamical processes of the ucla general circulation model. *General circulation models of the atmosphere. (A 78-10662 01-47)* New York, Academic Press, Inc. pp. 173–265.
- ARONS, A. & STOMMEL, H. 1958 A  $\beta$ -plane analysis of free periods of the second class in meridional and zonal oceans. *Deep Sea Research (1953)* **4**, 23–31.
- BAEHR, J., CUNNINGHAM, S., HAAK, H., HEIMBACH, P., KANZOW, T. & MAROTZKE, J. 2009 Observed and simulated estimates of the meridional overturning circulation at 26.5 n in the atlantic. *Ocean Science* **5** (5), 575–589.
- BORIS, J. P. & BOOK, D. 1976 Flux-corrected transport. iii. minimal-error fct algorithms. *Journal of Computational Physics* **20** (4), 397–431.
- BORIS, J. P. & BOOK, D. L. 1973 Flux-corrected transport. i. shasta, a fluid transport algorithm that works. *Journal of computational physics* **11** (1), 38–69.
- BORISOV, S. & NOF, D. 1998 Deep, cross-equatorial eddies. *Geophysical & Astrophysical Fluid Dynamics* **87** (3-4), 273–310, iD: 4893986589.
- BRESCH, D. 2009 Shallow-water equations and related topics. *Handbook of differential equations: evolutionary equations* **5**, 1–104.
- CHOBOTER, P. F. & SWATERS, G. E. 2000 Modeling equator-crossing currents on the ocean bottom. *Can. Appl. Math. Quart* **8**, 367–385.
- CHOBOTER, P. F. & SWATERS, G. E. 2003 Two-layer models of abyssal equator-crossing flow. *Journal of Physical Oceanography* **33** (7), 1401–1415, iD: 437675506.
- CHOBOTER, P. F. & SWATERS, G. E. 2004 Shallow water modeling of antarctic bottom water crossing the equator (doi 10.1029/2003jc002048). *Journal of geophysical research*. **109**, C03038, iD: 109612071.

- CHURBANOV, A. G., PAVLOV, A. N. & VABISHCHEVICH, P. N. 1995 Operator-splitting methods for the incompressible navier-stokes equations on non-staggered grids. part 1: First-order schemes. *International journal for numerical methods in fluids* **21** (8), 617–640.
- COLELLA, P., DORR, M. R., HITTINGER, J. A., MCCORQUODALE, P. & MARTIN, D. F. 2008 High-order, finite-volume methods on locally-structured grids. In *Proceedings of the Astronom-2008 Meeting, Astronomical Society of the Pacific Conference Series*, , vol. 406.
- COLELLA, P. & SEKORA, M. D. 2008 A limiter for ppm that preserves accuracy at smooth extrema. *Journal of Computational Physics* **227** (15), 7069–7076.
- COURANT, R., ISAACSON, E. & REES, M. 1952 On the solution of nonlinear hyperbolic differential equations by finite differences. *Communications on Pure and Applied Mathematics* **5** (3), 243–255.
- CUNNINGHAM, S. A., KANZOW, T., RAYNER, D., BARINGER, M. O., JOHNS, W. E., MAROTZKE, J., LONGWORTH, H. R., GRANT, E. M., HIRSCHI, J. J.-M., BEAL, L. M. *et al.* 2007 Temporal variability of the atlantic meridional overturning circulation at 26.5 n. *science* **317** (5840), 935–938.
- CURCHITSER, E. N., HAIDVOGEL, D. B. & ISKANDARANI, M. 1999 On the transient adjustment of a mid-latitude abyssal ocean basin with realistic geometry: The constant depth limit. *Dynamics of atmospheres and oceans* **29** (2), 147–188.
- CURRY, J. H. & WINSAND, D. 1986 Low-order intermediate models: bifurcation, recurrence and solvability. *Journal of the atmospheric sciences* **43** (21), 2360–2373.
- CUSHMAN-ROISIN, B. I. T. 1982 Motion of a free particle on a beta-plane. *Geophysical & Astrophysical Fluid Dynamics* **22** (1-2), 85–102.
- DE MADRON, X. D. & WEATHERLY, G. 1994 Circulation, transport and bottom boundary layers of the deep currents in the brazil basin. *Journal of marine research* **52** (4), 583–638.
- DVORKIN, Y. & PALDOR, N. 1999 Analytical considerations of lagrangian cross-equatorial flow. *Journal of the atmospheric sciences* **56** (9), 1229–1237.
- EDWARDS, C. A. & PEDLOSKY, J. 1998 Dynamics of nonlinear cross-equatorial flow. part i: Potential vorticity transformation. *Journal of Physical Oceanography* **28** (12), 2382, iD: 437944330.
- GALPERIN, B., NAKANO, H., HUANG, H.-P. & SUKORIANSKY, S. 2004 The ubiquitous zonal jets in the atmospheres of giant planets and earth’s oceans. *Geophysical research letters* **31** (13), L13303.
- GENT, P. R. 1993 The energetically consistent shallow-water equations. *Journal of Atmospheric Sciences* **50**, 1323–1325.
- GENT, P. R. & MCWILLIAMS, J. C. 1982 Intermediate model solutions to the lorenz equations: Strange attractors and other phenomena. *Journal of Atmospheric Sciences* **39**, 3–13.

- GUSTAFSSON, B. & SUNDSTROM, A. 1978 Incompletely parabolic problems in fluid dynamics. *SIAM Journal on Applied Mathematics* **35** (2), 343–357.
- KAMENKOVICH, I. V. & GOODMAN, P. J. 2001 The effects of vertical mixing on the circulation of the aabw in the atlantic. *Geophysical Monograph Series* **126**, 217–226.
- KAWASE, M., ROTHSTEIN, L. M. & SPRINGER, S. R. 1992 Encounter of a deep western boundary current with the equator: A numerical spin-up experiment. *Journal of Geophysical Research* **97** (C4), 5447–5463.
- KILLWORTH, P. D. 1991 Cross-equatorial geostrophic adjustment. *Journal of Physical Oceanography* **21** (10), 1581–1601, iD: 4644771815.
- KIRKPATRICK, M. P. & ARMFIELD, S. W. 2009 Open boundary conditions in numerical simulations of unsteady incompressible flow. *ANZIAM Journal* **50**, C760–C773.
- KUZMIN, D., LOHNER, R. & TUREK, S. 2005 Flux-corrected transport principles, algorithms, and applications. ID: 66465694.
- LORENZ, E. N. 1980 Attractor sets and quasi-geostrophic equilibrium. *Journal of the Atmospheric Sciences* **37** (8), 1685–1699.
- MACCORMACK, R. & PAULLAY, A. 1972 Computational efficiency achieved by time splitting of finite difference operators. *AIAA Journal* pp. 72–154.
- MCCARTHY, G., FRAJKA-WILLIAMS, E., JOHNS, W., BARINGER, M., MEINEN, C., BRYDEN, H., RAYNER, D., DUCHEZ, A., ROBERTS, C. & CUNNINGHAM, S. 2012 Observed interannual variability of the atlantic meridional overturning circulation at 26.5 n. *Geophysical Research Letters* **39** (19).
- MCCARTNEY, M. S. 1993 Crossing of the equator by the deep western boundary current in the western atlantic ocean. *Journal of physical oceanography* **23** (9), 1953–1974.
- MCCARTNEY, M. S. & CURRY, R. A. 1993 Transequatorial flow of antarctic bottom water in the western atlantic ocean: Abyssal geostrophy at the equator. *Journal of physical oceanography* **23**, 1264–1264.
- MCDONALD, P. 1971 The computation of transonic flow through two-dimensional gas turbine cascades. ASME.
- MEINEN, C. S., JOHNS, W. E., GARZOLI, S. L., VAN SEBILLE, E., RAYNER, D., KANZOW, T. & BARINGER, M. O. 2012 Variability of the deep western boundary current at 26.5 n during 2004–2009. *Deep Sea Research Part II: Topical Studies in Oceanography* .
- NOF, D. & BORISOV, S. 1998 Inter-hemispheric oceanic exchange. *Quarterly journal of the Royal Meteorological Society*. **124** (552), 2829, iD: 93017784.
- OLBERS, D., WILLEBRAND, J. & EDEN, C. 2012 *Ocean Dynamics*. Springer.
- PALDOR, N. & KILLWORTH, P. D. 1988 Inertial trajectories on a rotating earth. *Journal of the atmospheric sciences* **45** (24), 4013–4019.

- PALDOR, N. & SIGALOV, A. 2006 Inertial particle approximation to solutions of the shallow water equations on the rotating spherical earth. *Tellus A* **58** (2), 280–292.
- PALDOR, N., SIGALOV, A. & NOF, D. 2003 The mechanics of eddy transport from one hemisphere to the other. *Quarterly Journal of the Royal Meteorological Society* **129** (591), 2011–2025.
- PATANKAR, S. V. 1980 *Numerical heat transfer and fluid flow*. Taylor & Francis Group.
- PEDLOSKY, J. 1982 Geophysical fluid dynamics. *New York and Berlin, Springer-Verlag, 1982.636 p. 1.*
- PEÑA-MOLINO, B., JOYCE, T. M. & TOOLE, J. M. 2012 Variability in the deep western boundary current: local versus remote forcing. *Journal of Geophysical Research: Oceans (1978–2012)* **117** (C12).
- PENNELL, S. A. & SEITTER, K. L. 1990 On inertial motion on a rotating sphere. *Journal of Atmospheric Sciences* **47**, 2032–2034.
- PINARDI, N. & WOODS, J. 2002 *Ocean forecasting: conceptual basis and applications*. Springer.
- RAHMAN, M., MIETTINEN, A. & SIIKONEN, T. 1996 Modified simple formulation on a collocated grid with an assessment of the simplified quick scheme. *Numerical Heat Transfer* **30** (3), 291–314.
- RHIE, C. & CHOW, W. 1983 Numerical study of the turbulent flow past an airfoil with trailing edge separation. *AIAA Journal* **21** (11), 1525–1532.
- RHINES, P. B. 1975 Waves and turbulence on a beta-plane. *J. Fluid Mech* **69** (3), 417–443.
- RICHARDS, K., MAXIMENKO, N., BRYAN, F. & SASAKI, H. 2006 Zonal jets in the pacific ocean. *Geophysical research letters* **33** (3).
- RIPA, P. 1997 Inertial oscillations and the  $\beta$ -plane approximation (s). *Journal of physical oceanography* **27** (5), 633–647.
- SAMELSON, R. M. 2011 *The theory of large-scale ocean circulation*. Cambridge University Press.
- SANDOVAL, F. J. & WEATHERLY, G. L. 2001 Evolution of the deep western boundary current of antarctic bottom water in the brazil basin. *Journal of physical oceanography* **31** (6), 1440–1460.
- SARAFANOV, A., SOKOV, A. & DEMIDOV, A. 2007 Water mass characteristics in the equatorial north atlantic: A section nominally along 6.5 n, july 2000. *Journal of Geophysical Research* **112** (C12), C12023.
- SCHMID, C., BOURLES, B. & GOURIOU, Y. 2005 Impact of the equatorial deep jets on estimates of zonal transports in the atlantic. *Deep Sea Research Part II: Topical Studies in Oceanography* **52** (3), 409–428.

- SIEDLER, G., CHURCH, J., GOULD, J. & GRIFFIES, S. 2001 *Ocean circulation and climate: observing and modelling the global ocean*, , vol. 77. Academic Press.
- STEPHENS, J. C. & MARSHALL, D. P. 2000 Dynamical pathways of antarctic bottom water in the atlantic. *Journal of physical oceanography* **30** (3), 622–640.
- STEVENS, D. P. 1990 On open boundary conditions for three dimensional primitive equation ocean circulation models. *Geophysical & Astrophysical Fluid Dynamics* **51** (1-4), 103–133.
- STEWART, A. & DELLAR, P. 2012 Cross-equatorial channel flow with zero potential vorticity under the complete coriolis force. *IMA Journal of Applied Mathematics* **77** (5), 626–651.
- STOMMEL, H. & ARONS, A. 1959 On the abyssal circulation of the world ocean i. stationary planetary flow patterns on a sphere. *Deep Sea Research (1953) Deep Sea Research (1953)* **6**, 140–154, iD: 4633440336.
- SWATERS, G. E. 2006 The meridional flow of source-driven abyssal currents in a stratified basin with topography. part i: Model development and dynamical properties. *Journal of Physical Oceanography* **36** (3), 335–355.
- SWATERS, G. E. 2013 Flow of grounded abyssal ocean currents along zonally-varying topography on a rotating sphere. *Geophysical & Astrophysical Fluid Dynamics* pp. 1–23.
- VALLIS, G. K. 2006 *Atmospheric and oceanic fluid dynamics: fundamentals and large-scale circulation*. Cambridge University Press.
- YE, J. & MCCORQUODALE, J. 1997 Depth-averaged hydrodynamic model in curvilinear collocated grid. *Journal of Hydraulic Engineering* **123** (5), 380–388.
- ZALESAK, S. 1979 Fully multidimensional flux-corrected transport algorithms for fluids. *Journal of Computational Physics Journal of Computational Physics* **31** (3), 335–362, iD: 4657235746.